UC Irvine
UC Irvine Electronic Theses and Dissertations

Title

Electrocatalytic and Chemical Investigations of CO2 and N2O Reduction Using Late Transition Metal Hydrides

Permalink

https://escholarship.org/uc/item/4115w2hn

Author

Wang, Xinran

Publication Date

2023

Peer reviewed|Thesis/dissertation

UNIVERSITY OF CALIFORNIA,

IRVINE

Electrocatalytic and Chemical Investigations of CO_2 and N_2O Reduction Using Late Transition
Metal Hydrides

DISSERTATION

submitted in partial satisfaction of the requirements
for the degree of

DOCTOR OF PHILOSOPHY

in Chemistry

by

Xinran S. Wang

Dissertation Committee:

Chancellor's Professor Jenny Y. Yang, Chair
Distinguished Professor A. S. Borovik
Distinguished Professor Emeritus William J. Evans

2023

DEDICATION

For Teddy,

who really helped

TABLE OF CONTENTS

List of Figures

List of Tables

List of Schemes

List of Charts

ACKNOWLEDGEMENTS

CURRICULUM VITAE

Xinran S. Wang

EDUCATION

University of California, Irvine – Irvine, CA   2017-2023
Ph.D. in Chemistry

Carleton College – Northfield, MN   2013-2017
B.A. in Chemistry; Concentration in Biochemistry

RESEARCH EXPERIENCE

Graduate Research Assistant | University of California, Irvine   2018-present
Advisor: Jenny Y. Yang

- Designed transition metal complexes to mediate electrocatalytic CO_2 and N_2O reduction
- Characterized complexes using spectroscopic and electrochemical techniques
- Developed analytical methods for quantitative N_2 detection
- Quantified gaseous (H_2, N_2, CO) and solvated (formate) products from electrolysis

Undergraduate Research Assistant | Carleton College   2016-2017
Advisor: Matthew T. Whited

- Synthesized nickel silylamide complexes to access nickel-imide species for formal nitrene transfer

Research Intern | National Center for Advancing Translational Sciences   2015
Advisor: Shyh-Ming Yang

- Synthesized and optimized small molecule inhibitors of aldehyde dehydrogenase 1A1

TEACHING EXPERIENCE

Head Teaching Assistant| University of California, Irvine   Mar. 2020-June 2021
Chem 51LB/Chem 51LC: Organic Chemistry Lab

Graduate Teaching Assistant | University of California, Irvine   2017-2020
Chem 1A: General Chemistry, Chem 1LC/1LD: General Chemistry Lab, Chem 107: Inorganic Chemistry

Teaching Assistant / Grader | Carleton College   2015-2017

PUBLICATIONS

1. **Wang, X. S.**; Yang, J. Y. Development of a Molecular Electrocatalyst for the Reduction of Nitrous Oxide to Nitrogen. *Manuscript in preparation.*
2. **Wang, X. S.**; Yang, J. Y. Translating Aqueous CO_2 Hydrogenation Activity to Electrocatalytic Reduction with a Homogeneous Cobalt Catalyst. *Chem Commun.* **2023**, *59*, 338-341.
3. Yang, J. Y.; Kerr, T.; **Wang, X. S.**; Barlow, J. M., *J. Am. Chem. Soc.*, **2020**, *142* (46), 19438–19445. Reducing CO_2 to HCO_2^- at Mild Potentials: Lessons from Formate Dehydrogenase.
4. Yang, S.-M.; Martinez, N. J.; Yasgar, A.; Danchik, C.; Johansson, C.; Wang, Y.; Baljinnyam, B.; Wang, A. Q.; Xu, X.; Shah, P.; Cheff, D.; **Wang, X. S.**; Roth, J.; Lal-Nag, M.; Dunford, J. E.; Oppermann, U.; Vasiliou, V.; Simeonov, A.; Jadhav, A.; Maloney, D. J., *J. Med. Chem.* **2018**, *61* (11), 4883–4903. Discovery of Orally Bioavailable, Quinoline-Based Aldehyde Dehydrogenase 1A1 (ALDH1A1) Inhibitors with Potent Cellular Activity.

PRESENTATIONS

1. Yang, J. Y., **Wang, X. S.** Bio-inspired electrocatalysts for CO_2 reduction to formate. *ACS Spring 2022 National Meeting*, San Diego, CA. *Oral presentation*
2. **Wang, X. S.**, Development of an aqueous electrocatalyst for CO_2 reduction to formate. *ACS Fall 2021 National Meeting*, Atlanta, GA. *Virtual presentation*
3. **Wang, X. S.**, Yang, J. Y. Development of an aqueous electrocatalyst for reversible CO_2 reduction to formate. *ACS Fall 2019 National Meeting*, San Diego, CA. *Oral presentation*
4. **Wang, X. S.** Development of an aqueous electrocatalyst for reversible CO_2 reduction to formate. *SoCal Bioinorganic 2019*, University of California, Los Angeles. *Poster presentation*
5. **Wang, X. S.**, Kerr, T. Tuning the hydricity of metal complexes for selective CO_2 reduction. *SoCal Bioinorganic 2018*, California Institute of Technology. *Poster presentation*

AWARDS | HONORS

Chemistry Dissertation Fellowship | University of California, Irvine	Nov. 2022
ADDSTEAM Scholar	May 2022
Solutions that Scale Fellowship | University of California, Irvine	June 2021
Department Service Award | University of California, Irvine	May 2020
Sigma Xi member	June 2017

CERTIFICATES

Mentoring Excellence Program
Management Beyond the Classroom
Industry Insights for STEM Scientists

ABSTRACT OF THE DISSERTATION

Electrocatalytic and Chemical Investigations of CO_2 and N_2O Reduction Using Late Transition

Metal Hydrides

by

Xinran S. Wang

Increasing atmospheric concentrations of greenhouse gases driven by anthropogenic emissions of CO_2 and N_2O are a critical concern for climate change and global warming. Electrocatalysts which can use renewable energy to directly abate these greenhouse gases via chemical reduction are desirable. This dissertation describes experimental research to develop a new aqueous CO_2 reduction electrocatalyst inspired by hydrogenation catalysts, as well as a new organic N_2O reduction electrocatalyst inspired by electrochemical CO_2 reduction. Lastly, a series of transition metal complexes were chosen and investigated based on their thermodynamic and redox properties to identify metals which activate N_2O at milder potentials.

Ch. 1 details the translation of $[Co(dmpe)_2(H)_2]^+$, an aqueous hydrogenation catalyst, into an aqueous electrocatalyst. The hydricity of this compound is pH-dependent in water due to OH^- binding upon hydride transfer, thus the free energies of CO_2 reduction and HER are both thermodynamically favourable at neutral pH. Both HCO_2^- and H_2 are observed under stoichiometric conditions and during controlled potential electrolysis.

Ch. 2 establishes $[Pt(dmpe)_2]^{2+}$ as an electrocatalyst for N_2O reduction. Controlled potential electrolysis experiments demonstrate good selectivity for N_2. Cyclic voltammetry and NMR experiments indicate that $[Pt(dmpe)_2H]^+$ and $[Pt(dmpe)_2OH]^+$ are key intermediates in the catalytic cycle, and that N_2O insertion into the Pt-H is rate limiting.

Ch. 3 describes the reactivity of several late transition metal hydrides with N_2O. These hydrides span a 15 kcal/mol range in hydride donor strength. While all are demonstrated to react with N_2O, there is no apparent correlation between N_2O activation and hydride donor strength or pK_a.

Introduction

0.1 Background and motivation

Atmospheric concentrations of greenhouse gases such as carbon dioxide (CO_2) and nitrous oxide (N_2O) have significantly increased in the last 50 years.[1,2] These increases in atmospheric concentration for both gases are responsible for driving anthropogenic climate change and are a result of increased emissions. Although the absolute concentration of N_2O is much lower than that of CO_2, N_2O has 300 times the global warming potential.[3,4] Anthropogenic CO_2 emissions arise primarily due to fossil fuel consumption in transportation and electricity production.[5] Anthropogenic N_2O emissions largely originate from agriculture (through a denitrification cycle after the use of nitrogen-based fertilizers) as well as fossil fuel combustion and industrial sources.[3,6,7] Global demands for energy and fertilizer use are projected to continue increasing for the next 30 years.[8,9] In order to meet these demands while simultaneously decreasing net emissions, it is therefore desirable to: (a) develop alternative fuel sources produced from CO_2 and renewable energy to replace fossil fuels, and (b) identify technologies and strategies that can directly mitigate N_2O emissions.[10,11] Precision fertilization will likely play a significant role in reducing nitrous oxide from agricultural sources, but direct abatement strategies at industrial emission sites such as nitric and adipic acid plants will also be needed to achieve climate goals in the next 100 years.[10]

0.2 Electrochemical CO_2 reduction and hydricity

One method to developing alternative fuel sources is the conversion of CO_2 to reduced C_1 products such as formic acid (HCO_2H) or formate (HCO_2^-) which can be used as fuels or chemical feedstocks.[12,13] Molecular hydrogenation catalysts which perform these reactions are well-studied but frequently operate at high temperatures and pressures of H_2 and CO_2.[14–16] Another conversion method, the electrochemical reduction of CO_2, can be conducted under

ambient conditions and 1 atm of CO_2.[17–20] Table 0.1 details the thermodynamic potentials for selected CO_2 reduction products.[21]

Table 0.1. Thermodynamic potentials of selected CO_2 reduction reactions.

CO₂ reduction reaction	E° vs. NHE (pH 7)
$CO_2 + 2H^+ + 2e^- \longrightarrow CO + H_2O$	-0.53 V
$CO_2 + H^+ + 2e^- \longrightarrow HCO_2^-$	-0.49 V

CO_2 reduction to formate (HCO_2^-) can also be described as a formal hydride transfer, where the hydride (H^-) combines both the proton and two electrons.[22,23]

$$HCO_2^- \longrightarrow CO_2 + H^- \qquad \Delta G^\circ_{H^-} = 44.0 \text{ kcal/mol (MeCN)} \qquad (\text{Eq 0.1})$$
$$\Delta G^\circ_{H^-} = 24.1 \text{ kcal/mol (H}_2\text{O)} \qquad (\text{Eq 0.2})$$

The free energy of this reaction can be described in terms of hydricity ($\Delta G^\circ_{H^-}$), a thermodynamic parameter which describes the free energy of a given compound to release a hydride (H^-).[24] The hydricity of HCO_2^- has been experimentally determined to be 24.1 kcal/mol in water (H_2O) and 44.0 kcal/mol in acetonitrile (MeCN).[23,25,26]

Transition metal hydrides ($[M-H]^n$) are key intermediates proposed in catalytic CO_2 reduction to formate.[27] Their hydride donor ability can be described using hydricity. $[M-H]^n$ compounds can be generated electrochemically via two, one-electron reductions of the parent species M^{n+1} to form M^{n-1} followed by protonation. Consequently, one method to determine the hydricity of a $[M-H]^n$ is through the potential-pK_a method:[23]

$[M]^{n-1} \rightleftharpoons [M]^n + e^-$	$\Delta G^\circ = 23.06 * E^\circ$	Eq 0.3
$[M]^n \rightleftharpoons [M]^{n+1} + e^-$	$\Delta G^\circ = 23.06 * E^\circ$	Eq. 0.4
$[M-H]^n \rightleftharpoons [M]^{n-1} + H^+$	$\Delta G^\circ = 1.364 * pK_a$	Eq. 0.5
$H^+ + 2e^- \rightleftharpoons H^-$	$\Delta G^\circ = 79.6$ kcal/mol (MeCN) $\Delta G^\circ = 34.2$ kcal/mol (H₂O)	Eq 0.6
$[M-H]^n \rightleftharpoons [M]^{n+1} + H^-$	$\Delta G^\circ = \Sigma(\Delta G^\circ)$	Eq 0.7

When the reduction of the parent M^{n+1} species occurs in a single two-electron process, Eq. 0.4 and 0.5 are combined to form Eq. 0.8:

$[M]^{n-1} \rightleftharpoons [M]^{n+1} + 2\ e^-$	$\Delta G° = 46.12 * E°$	Eq 0.8
$[M\text{-}H]^n \rightleftharpoons [M]^{n-1} + H^+$	$\Delta G° = 1.364 * pK_a$	Eq. 0.5
$H^+ + 2\ e^- \rightleftharpoons H^-$	$\Delta G° = 79.6$ kcal/mol (MeCN) $\Delta G° = 34.2$ kcal/mol (H_2O)	Eq 0.6
$[M\text{-}H]^n \rightleftharpoons [M]^{n+1} + H^-$	$\Delta G°_{H-} = \Sigma(\Delta G°)$	Eq 0.9
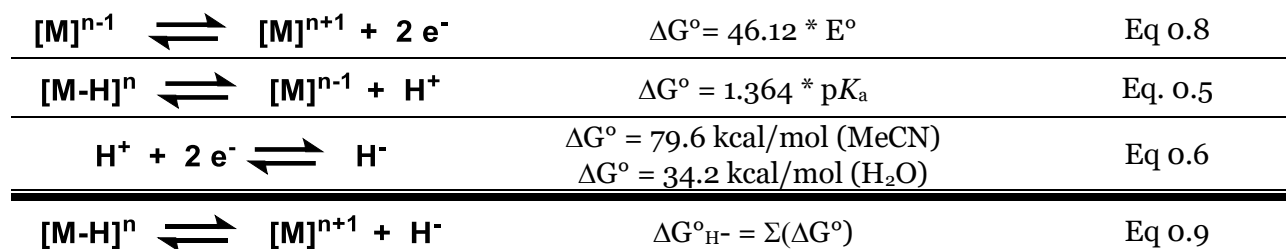
Hydride transfer from a $[M\text{-}H]^n$ to CO_2 to produce formate is exergonic when the hydricity of the metal hydride *is lower* than that of formate in a particular solvent (44.0 kcal/mol in MeCN, 24.1 kcal/mol in H_2O).

$$[MH]^n + CO_2 \rightleftharpoons [M]^{n+1} + HCO_2^- \qquad \Delta G° = \Delta G°_{H-}(MH^n) - \Delta G°_{H-}(HCO_2^-) \qquad \text{Eq 0.10}$$

Using this parameter, reactive transition metal hydrides for CO_2 reduction can be identified for each solvent.

0.3 Electrocatalysts and hydrogenation catalysts for CO_2 reduction

The Yang group has previously demonstrated selective electrocatalytic CO_2 reduction to formate in MeCN without H_2 production using two well defined Pt-H species: $[Pt(dmpe)_2H]^+$ (dmpe = 1,2-*bis*(dimethylphosphino)ethane) and $[Pt(depe)_2H]^+$ (depe = 1,2-*bis*(diethylphosphino)ethane).[28,29] $[Pt(dmpe)_2H]^+$ has a hydricity of 41.4 kcal/mol in MeCN, less than that of HCO_2^- while $[Pt(depe)_2H]^+$ has a hydricity of 44.0 kcal/mol in MeCN.[30] $[Pt(depe)_2H]^+$ also demonstrated *reversible* electrocatalysis for CO_2 reduction to HCO_2^-, made possible in part due to ergoneutral hydride transfer to CO_2.[29,31]

Another way to identify electrocatalyst candidates for CO_2 reduction is to "electrify" known hydrogenation catalysts (**Chart 0.1**). Hazari and Palmore were able to demonstrate this with $Ir(PNP)H_3$, an aqueous hydrogenation catalyst, by turning it into an organic electrocatalyst

3

for formate production with 12% H_2O in MeCN.[32,33] Similarly, Saouma and coworkers

demonstrated both hydrogenation catalysis and electrocatalysis using $Co(^{Me}P_3)Cl$ and

$Co(^{Bz2N}P_3)Cl$ complexes using 3% H_2O in MeCN.[34] Kang and coworkers have also established

$[Fe(P(PPh_2)_3)]^{2+}$ as a competent electrocatalyst after Beller and coworkers first identified it as a

hydrogenation catalyst.[35,36] An analysis of the literature shows that no aqueous hydrogenation

catalysts have been successfully translated into aqueous electrocatalysts for CO_2 reduction to

formate.
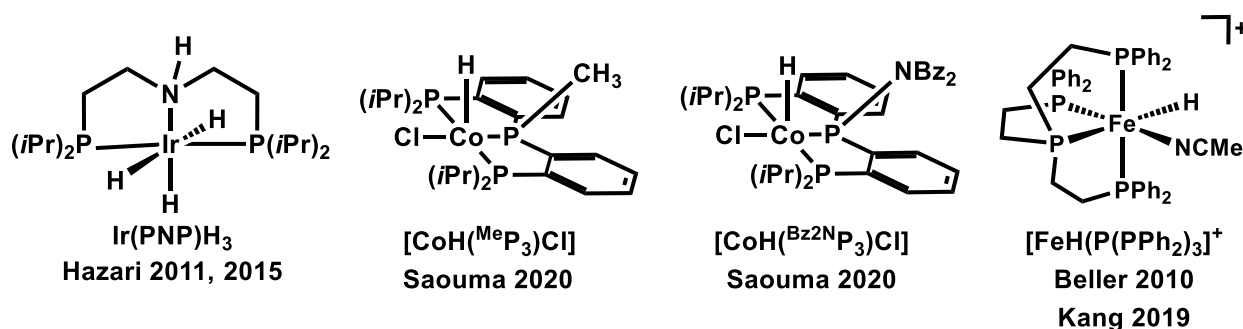
Chart 0.1. Examples of CO_2 hydrogenation catalysts which have also been identified as electrocatalysts for CO_2 reduction.

0.4 Methods for N_2O abatement

N_2O is another greenhouse gas that is isoelectronic to CO_2 and a number of transition metal

complexes have been identified as catalysts for the hydrogenation of N_2O to N_2 and H_2O.[37] These

include the Ru and Ir pincer complexes developed by Milstein and Suárez respectively,[38,39] as

well as a Pt-Rh compound developed by Grützmacher and coworkers (**Chart 0.2**).[40] With the

exception of the Ir pincer system, these N_2O hydrogenation catalysts have similar limitations to

CO_2 hydrogenation catalysts, necessitating heat and > 1 atm of N_2O and H_2 gas. Furthermore,

strategies to abate industrial nitrous oxide emissions currently use heterogeneous catalysts to

promote the decomposition of N_2O at temperatures > 500 C.[7,41,42]
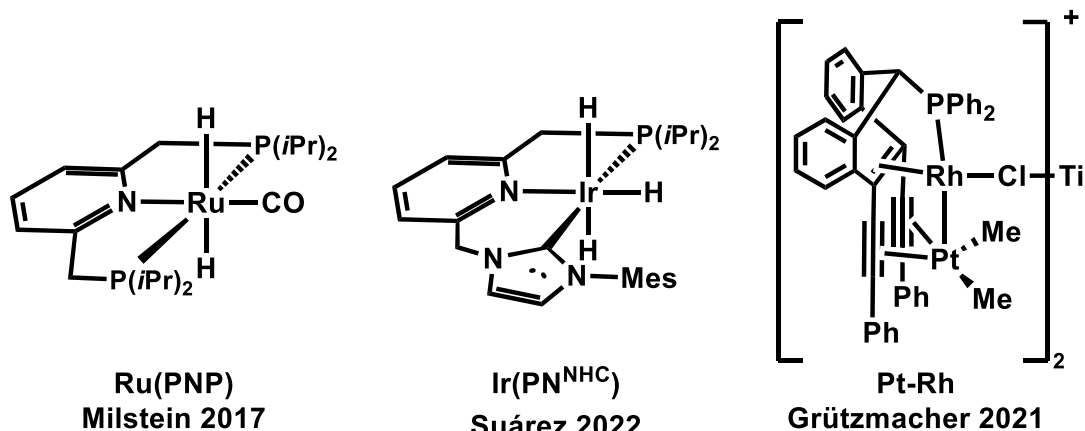
Chart 0.2. Examples of N_2O hydrogenation catalysts.

Just as CO_2 reduction can proceed via hydrogenation or electrocatalysis, so can N_2O reduction. N_2O can be reduced via a two electron, two proton reaction to form N_2 and water.[37,43] Unlike CO_2 reduction, this process is exergonic and N_2O is generally considered a potent oxidant.[44,45]

$$N_2O \ + \ 2H^+ \ + \ 2e^- \ \longrightarrow \ N_2 \ + \ H_2O \quad E° = 1.76 \text{ V vs. NHE}$$ (Eq 0.11)
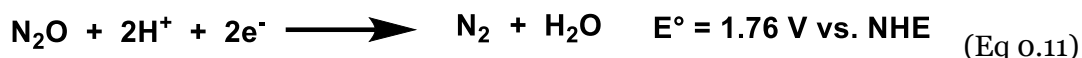
While much research has been conducted on homogeneous electrocatalytic CO_2 reduction, there have been comparatively few examples of homogeneous electrocatalytic reduction of N_2O. Since the substrate is isoelectronic to CO_2, it is unsurprising that the few homogeneous transition metal electrocatalysts (**Chart 0.3**) that have been identified are also known CO_2-to-CO reduction catalysts. In 1981, L'Her and coworkers demonstrated that Co(porphyrin) complexes were capable of electrocatalytic reduction of N_2O.[46] More recently, Costentin demonstrated high selectivity and electrocatalysis using $Re(bpy)(CO)_3Cl$ and $Mn(bpy)(CO)_3Br$ systems in 2021.[47] Taniguchi and coworkers identified Ni macrocyclic tetraamine complexes like $Ni(cyclam)^{2+}$ as competent electrocatalysts when using a mercury pool electrode in 1990;[48] however, the Hg may play the same critical role in these catalysts in modulating selectivity and activity as it does in CO_2 reduction.[49−52]

CoTPP
L'Her 1981

Ni(cyclam)$^{2+}$
Tanaguchi 1990

Re(bpy)(CO)$_3$Cl
Costentin 2021

Mn(bpy)(CO)$_3$Br
Costentin 2021
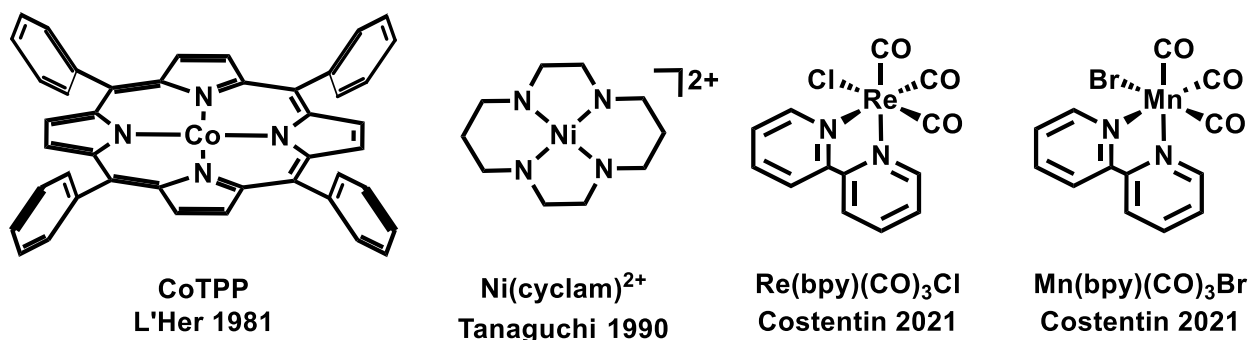
Chart 0.3. Examples of electrocatalytic N_2O reduction catalysts.

Since N_2O reduction to N_2 is significantly more exergonic than CO_2 reduction, electrocatalysts for N_2O reduction may not need to be as reducing as those used for CO_2 reduction. As previously mentioned, hydricity, which describes hydride donor ability has a direct correlation with reduction potential. Consequently, less hydridic compounds (or weaker hydride donors) are usually also less reducing. Using hydricity as a screening parameter, it is possible to identify $[M-H]^n$ complexes with hydricity values *above* 44.0 kcal/mol to find species which react with N_2O but are not sufficiently hydridic to reduce CO_2.

0.5 Research goals

The research presented in this dissertation describes advances made to develop new electrocatalysts for CO_2 reduction in aqueous solvents and N_2O reduction in organic solvents. An aqueous cobalt hydrogenation catalyst, $[Co(dmpe)_2(H)_2]^+$, was "electrified" and developed into an aqueous electrocatalyst. Hydricity was used to understand and interpret the product selectivity observed by this system under catalytic and stoichiometric conditions since both HCO_2^- and H_2 are observed. The lack of selectivity illustrates a challenge in translating CO_2 reduction with hydrogenation catalysis to electrocatalysis since H_2 is a reagent during in the former, and an undesired side product in the latter.

Investigations were conducted to expand the library of electrocatalysts for N_2O reduction and elucidate whether CO_2 reduction catalysts which operate through a $[M-H]^n$ intermediate can

reduce N_2O. The hydricity of $[Pt(dmpe)_2H]^+$ was previously used to identify a CO_2 to formate electrocatalyst, $[Pt(dmpe)_2]^{2+}$. Electrocatalytic N_2O reduction was demonstrated with this system. Notably, the proposed mechanism is different from previously identified N_2O reduction electrocatalysts since it proceeds through a $[M-H]^+$ and $[M-OH]^+$ intermediate. Hydricity was also used to identify less reducing compounds which could still be active for N_2O reduction. While a number of these complexes reacted with N_2O, there was no apparent trend between reactivity and reducing ability. It was possible, however, able to identify metal hydrides less reducing than $[Pt(dmpe)_2H]^+$ which react with N_2O and are promising candidates for further study as N_2O reduction electrocatalysts.

0.6 References

(1)   US Department of Commerce, N. *Global Monitoring Laboratory - Carbon Cycle Greenhouse Gases*. https://gml.noaa.gov/ccgg/trends/ (accessed 2023-02-23).

(2)   *AGAGE Data & Figures | Advanced Global Atmospheric Gases Experiment*. https://agage.mit.edu/data/agage-data (accessed 2023-02-23).

(3)   Tian, H.; Xu, R.; Canadell, J. G.; Thompson, R. L.; Winiwarter, W.; Suntharalingam, P.; Davidson, E. A.; Ciais, P.; Jackson, R. B.; Janssens-Maenhout, G.; Prather, M. J.; Regnier, P.; Pan, N.; Pan, S.; Peters, G. P.; Shi, H.; Tubiello, F. N.; Zaehle, S.; Zhou, F.; Arneth, A.; Battaglia, G.; Berthet, S.; Bopp, L.; Bouwman, A. F.; Buitenhuis, E. T.; Chang, J.; Chipperfield, M. P.; Dangal, S. R. S.; Dlugokencky, E.; Elkins, J. W.; Eyre, B. D.; Fu, B.; Hall, B.; Ito, A.; Joos, F.; Krummel, P. B.; Landolfi, A.; Laruelle, G. G.; Lauerwald, R.; Li, W.; Lienert, S.; Maavara, T.; MacLeod, M.; Millet, D. B.; Olin, S.; Patra, P. K.; Prinn, R. G.; Raymond, P. A.; Ruiz, D. J.; van der Werf, G. R.; Vuichard, N.; Wang, J.; Weiss, R. F.; Wells, K. C.; Wilson, C.; Yang, J.; Yao, Y. A Comprehensive Quantification of Global Nitrous Oxide Sources and Sinks. *Nature* **2020**, *586* (7828), 248–256. https://doi.org/10.1038/s41586-020-2780-0.

(4)   US EPA, O. *Overview of Greenhouse Gases*. https://www.epa.gov/ghgemissions/overview-greenhouse-gases (accessed 2023-02-23).

(5)   Yoro, K. O.; Daramola, M. O. Chapter 1 - CO2 Emission Sources, Greenhouse Gases, and the Global Warming Effect. In *Advances in Carbon Capture*; Rahimpour, M. R., Farsi, M., Makarem, M. A., Eds.; Woodhead Publishing, 2020; pp 3–28. https://doi.org/10.1016/B978-0-12-819657-1.00001-3.

(6)   Lehnert, N.; Dong, H. T.; Harland, J. B.; Hunt, A. P.; White, C. J. Reversing Nitrogen Fixation. *Nat. Rev. Chem.* **2018**, *2* (10), 278–289. https://doi.org/10.1038/s41570-018-0041-7.

(7)   Konsolakis, M. Recent Advances on Nitrous Oxide (N2O) Decomposition over Non-Noble-Metal Oxide Catalysts: Catalytic Performance, Mechanistic Considerations, and Surface Chemistry Aspects. *ACS Catal.* **2015**, *5* (11), 6397–6421. https://doi.org/10.1021/acscatal.5b01605.

(8)   Reay, D. S.; Davidson, E. A.; Smith, K. A.; Smith, P.; Melillo, J. M.; Dentener, F.; Crutzen, P. J. Global Agriculture and Nitrous Oxide Emissions. *Nat. Clim. Change* **2012**, *2* (6), 410–416. https://doi.org/10.1038/nclimate1458.

(9)   Scheffran, J.; Felkers, M.; Froese, R. Economic Growth and the Global Energy Demand. In *Green Energy to Sustainability*; John Wiley & Sons, Ltd, 2020; pp 1–44. https://doi.org/10.1002/9781119152057.ch1.

(10) Centi, G.; Perathoner, S. Reduction of Non-CO2 Greenhouse Gas Emissions by Catalytic Processes. In *Handbook of Climate Change Mitigation and Adaptation*; Lackner, M., Sajjadi, B., Chen, W.-Y., Eds.; Springer: New York, NY, 2020; pp 1–44. https://doi.org/10.1007/978-1-4614-6431-0_49-3.

(11) Gielen, D.; Boshell, F.; Saygin, D.; Bazilian, M. D.; Wagner, N.; Gorini, R. The Role of Renewable Energy in the Global Energy Transformation. *Energy Strategy Rev.* **2019**, *24*, 38–50. https://doi.org/10.1016/j.esr.2019.01.006.

(12)   Robert, M. Running the Clock: CO $_2$ Catalysis in the Age of Anthropocene. *ACS Energy Lett.* **2016**, *1* (1), 281–282. https://doi.org/10.1021/acsenergylett.6b00159.

(13)   Benson, E. E.; Kubiak, C. P.; Sathrum, A. J.; Smieja, J. M. Electrocatalytic and Homogeneous Approaches to Conversion of CO2 to Liquid Fuels. *Chem. Soc. Rev.* **2008**, *38* (1), 89–99. https://doi.org/10.1039/B804323J.

(14)   Jessop, P. G.; Joó, F.; Tai, C.-C. Recent Advances in the Homogeneous Hydrogenation of Carbon Dioxide. *Coord. Chem. Rev.* **2004**, *248* (21), 2425–2442. https://doi.org/10.1016/j.ccr.2004.05.019.

(15)   Bai, S.-T.; Smet, G. D.; Liao, Y.; Sun, R.; Zhou, C.; Beller, M.; Maes, B. U. W.; Sels, B. F. Homogeneous and Heterogeneous Catalysts for Hydrogenation of CO2 to Methanol under Mild Conditions. *Chem. Soc. Rev.* **2021**, *50* (7), 4259–4298. https://doi.org/10.1039/D0CS01331E.

(16)   Federsel, C.; Jackstell, R.; Beller, M. State-of-the-Art Catalysts for Hydrogenation of Carbon Dioxide. *Angew. Chem. Int. Ed.* **2010**, *49* (36), 6254–6257. https://doi.org/10.1002/anie.201000533.

(17)   Kang, P.; Cheng, C.; Chen, Z.; Schauer, C. K.; Meyer, T. J.; Brookhart, M. Selective Electrocatalytic Reduction of CO2 to Formate by Water-Stable Iridium Dihydride Pincer Complexes. *J. Am. Chem. Soc.* **2012**, *134* (12), 5500–5503. https://doi.org/10.1021/ja300543s.

(18)   Kang, P.; Meyer, T. J.; Brookhart, M. Selective Electrocatalytic Reduction of Carbon Dioxide to Formate by a Water-Soluble Iridium Pincer Catalyst. *Chem. Sci.* **2013**, *4* (9), 3497–3502. https://doi.org/10.1039/C3SC51339D.

(19)   Taheri, A.; Thompson, E. J.; Fettinger, J. C.; Berben, L. A. An Iron Electrocatalyst for Selective Reduction of CO $_2$ to Formate in Water: Including Thermochemical Insights. *ACS Catal.* **2015**, *5* (12), 7140–7151. https://doi.org/10.1021/acscatal.5b01708.

(20) Lu, X.; Leung, D. Y. C.; Wang, H.; Leung, M. K. H.; Xuan, J. Electrochemical Reduction of Carbon Dioxide to Formic Acid. *ChemElectroChem* **2014**, *1* (5), 836–849. https://doi.org/10.1002/celc.201300206.

(21) Sutin, N.; Creutz, C.; Fujita, E. Photo-Induced Generation of Dihydrogen and Reduction of Carbon Dioxide Using Transition Metal Complexes. *Comments Inorg. Chem.* **1997**, *19* (2), 67–92. https://doi.org/10.1080/02603599708032729.

(22) Brereton, K. R.; Smith, N. E.; Hazari, N.; Miller, A. J. M. Thermodynamic and Kinetic Hydricity of Transition Metal Hydrides. *Chem. Soc. Rev.* **2020**, *49* (22), 7929–7948. https://doi.org/10.1039/D0CS00405G.

(23) Wiedner, E. S.; Chambers, M. B.; Pitman, C. L.; Bullock, R. M.; Miller, A. J. M.; Appel, A. M. Thermodynamic Hydricity of Transition Metal Hydrides. *Chem. Rev.* **2016**, *116* (15), 8655–8692. https://doi.org/10.1021/acs.chemrev.6b00168.

(24) Curtis, C. J.; Miedaner, A.; Ellis, W. W.; DuBois, D. L. Measurement of the Hydride Donor Abilities of [HM(Diphosphine)2]+ Complexes (M = Ni, Pt) by Heterolytic Activation of Hydrogen. *J. Am. Chem. Soc.* **2002**, *124* (9), 1918–1925. https://doi.org/10.1021/ja0116829.

(25) Brereton, K. R.; Jadrich, C. N.; Stratakes, B. M.; Miller, A. J. M. Thermodynamic Hydricity across Solvents: Subtle Electronic Effects and Striking Ligation Effects in Iridium Hydrides. *Organometallics* **2019**, *38* (16), 3104–3110. https://doi.org/10.1021/acs.organomet.9b00278.

(26) Robinson, S. J. C.; Zall, C. M.; Miller, D. L.; Linehan, J. C.; Appel, A. M. Solvent Influence on the Thermodynamics for Hydride Transfer from Bis(Diphosphine) Complexes of Nickel. *Dalton Trans.* **2016**, *45* (24), 10017–10023. https://doi.org/10.1039/C6DT00309E.

(27) Barlow, J. M.; Yang, J. Y. Thermodynamic Considerations for Optimizing Selective CO2 Reduction by Molecular Catalysts. *ACS Cent. Sci.* **2019**, *5* (4), 580–588. https://doi.org/10.1021/acscentsci.9b00095.

(28) Ceballos, B. M.; Yang, J. Y. Directing the Reactivity of Metal Hydrides for Selective CO2 Reduction. *Proc. Natl. Acad. Sci.* **2018**, *115* (50), 12686–12691. https://doi.org/10.1073/pnas.1811396115.

(29) Cunningham, D. W.; Barlow, J. M.; Velazquez, R. S.; Yang, J. Y. Reversible and Selective CO2 to HCO2− Electrocatalysis near the Thermodynamic Potential. *Angew. Chem. Int. Ed.* **2020**, *59* (11), 4443–4447. https://doi.org/10.1002/anie.201913198.

(30) Berning, D. E.; Noll, B. C.; DuBois, D. L. Relative Hydride, Proton, and Hydrogen Atom Transfer Abilities of [HM(Diphosphine)2]PF6 Complexes (M = Pt, Ni). *J. Am. Chem. Soc.* **1999**, *121* (49), 11432–11447. https://doi.org/10.1021/ja991888y.

(31) Cunningham, D. W.; Yang, J. Y. Kinetic and Mechanistic Analysis of a Synthetic Reversible CO2/HCO2− Electrocatalyst. *Chem. Commun.* **2020**, *56* (85), 12965–12968. https://doi.org/10.1039/D0CC05556E.

(32) Ahn, S. T.; Bielinski, E. A.; Lane, E. M.; Chen, Y.; Bernskoetter, W. H.; Hazari, N.; Palmore, G. T. R. Enhanced CO$_2$ Electroreduction Efficiency through Secondary Coordination Effects on a Pincer Iridium Catalyst. *Chem. Commun.* **2015**, *51* (27), 5947–5950. https://doi.org/10.1039/C5CC00458F.

(33) Schmeier, T. J.; Dobereiner, G. E.; Crabtree, R. H.; Hazari, N. Secondary Coordination Sphere Interactions Facilitate the Insertion Step in an Iridium(III) CO2 Reduction Catalyst. *J. Am. Chem. Soc.* **2011**, *133* (24), 9274–9277. https://doi.org/10.1021/ja2035514.

(34) Wang, F.; Cannon, A. T.; Bhattacharya, M.; Baumgarten, R.; VanderLinden, R. T.; Saouma, C. T. Hydrogenation and Electrocatalytic Reduction of Carbon Dioxide to Formate with a Single Co Catalyst. *Chem. Commun.* **2020**, *56* (81), 12142–12145. https://doi.org/10.1039/D0CC04310A.

(35) Bi, J.; Hou, P.; Liu, F.-W.; Kang, P. Electrocatalytic Reduction of CO2 to Methanol by Iron Tetradentate Phosphine Complex Through Amidation Strategy. *ChemSusChem* **2019**, *12* (10), 2195–2201. https://doi.org/10.1002/cssc.201802929.

(36) Federsel, C.; Boddien, A.; Jackstell, R.; Jennerjahn, R.; Dyson, P. J.; Scopelliti, R.; Laurenczy, G.; Beller, M. A Well-Defined Iron Catalyst for the Reduction of Bicarbonates and Carbon Dioxide to Formates, Alkyl Formates, and Formamides. *Angew. Chem. Int. Ed.* **2010**, *49* (50), 9777–9780. https://doi.org/10.1002/anie.201004263.

(37) Rathnayaka, S. C.; Mankad, N. P. Coordination Chemistry of the CuZ Site in Nitrous Oxide Reductase and Its Synthetic Mimics. *Coord. Chem. Rev.* **2021**, *429*, 213718. https://doi.org/10.1016/j.ccr.2020.213718.

(38) Zeng, R.; Feller, M.; Ben-David, Y.; Milstein, D. Hydrogenation and Hydrosilylation of Nitrous Oxide Homogeneously Catalyzed by a Metal Complex. *J. Am. Chem. Soc.* **2017**, *139* (16), 5720–5723. https://doi.org/10.1021/jacs.7b02124.

(39) Ortega-Lepe, I.; Sánchez, P.; Santos, L. L.; Lara, P.; Rendón, N.; López-Serrano, J.; Salazar-Pereda, V.; Álvarez, E.; Paneque, M.; Suárez, A. Catalytic Nitrous Oxide Reduction with H2 Mediated by Pincer Ir Complexes. *Inorg. Chem.* **2022**, *61* (46), 18590–18600. https://doi.org/10.1021/acs.inorgchem.2c02963.

(40) Jurt, P.; Abels, A. S.; Gamboa-Carballo, J. J.; Fernández, I.; Le Corre, G.; Aebli, M.; Baker, M. G.; Eiler, F.; Müller, F.; Wörle, M.; Verel, R.; Gauthier, S.; Trincado, M.; Gianetti, T. L.; Grützmacher, H. Reduction of Nitrogen Oxides by Hydrogen with Rhodium(I)–Platinum(II) Olefin Complexes as Catalysts. *Angew. Chem. Int. Ed.* **2021**, *60* (48), 25372–25380. https://doi.org/10.1002/anie.202109642.

(41) Pérez-Ramı́rez, J.; Kapteijn, F.; Schöffel, K.; Moulijn, J. A. Formation and Control of N2O in Nitric Acid Production: Where Do We Stand Today? *Appl. Catal. B Environ.* **2003**, *44* (2), 117–151. https://doi.org/10.1016/S0926-3373(03)00026-2.

(42) Shimizu, A.; Tanaka, K.; Fujimori, M. Abatement Technologies for N2O Emissions in the Adipic Acid Industry. *Chemosphere - Glob. Change Sci.* **2000**, *2*, 425–434. https://doi.org/10.1016/S1465-9972(00)00024-6.

(43) Bar-Nahum, I.; Gupta, A. K.; Huber, S. M.; Ertem, M. Z.; Cramer, C. J.; Tolman, W. B. Reduction of Nitrous Oxide to Dinitrogen by a Mixed Valent Tricopper-Disulfido Cluster. *J. Am. Chem. Soc.* **2009**, *131* (8), 2812–2814. https://doi.org/10.1021/ja808917k.

(44) Severin, K. Synthetic Chemistry with Nitrous Oxide. *Chem. Soc. Rev.* **2015**, *44* (17), 6375–6386. https://doi.org/10.1039/C5CS00339C.

(45) Severin, K. Homogeneous Catalysis with Nitrous Oxide. *Trends Chem.* **2023**, *0* (0). https://doi.org/10.1016/j.trechm.2022.12.008.

(46) Collman, J. P.; Marrocco, M.; Elliott, C. M.; L'Her, M. Electrocatalysis of Nitrous Oxide Reduction: Comparison of Several Porphyrins and Binary "Face-to-Face" Porphyrins. *J. Electroanal. Chem. Interfacial Electrochem.* **1981**, *124* (1), 113–131. https://doi.org/10.1016/S0022-0728(81)80289-6.

(47) Deeba, R.; Molton, F.; Chardon-Noblat, S.; Costentin, C. Effective Homogeneous Catalysis of Electrochemical Reduction of Nitrous Oxide to Dinitrogen at Rhenium Carbonyl Catalysts. *ACS Catal.* **2021**, *11* (10), 6099–6103. https://doi.org/10.1021/acscatal.1c01197.

(48) Taniguchi, I.; Shimpuku, T.; Yamashita, K.; Ohtaki, H. Electrocatalytic Reduction of Nitrous Oxide to Dinitrogen at a Mercury Electrode Using Niii Complexes of Macrocyclic Polyamines. *J. Chem. Soc. Chem. Commun.* **1990**, No. 13, 915–917. https://doi.org/10.1039/C39900000915.

(49) Beley, Marc.; Collin, J. Paul.; Ruppert, Romain.; Sauvage, J. Pierre. Electrocatalytic Reduction of Carbon Dioxide by Nickel Cyclam2+ in Water: Study of the Factors Affecting the Efficiency and the Selectivity of the Process. *J. Am. Chem. Soc.* **1986**, *108* (24), 7461–7467. https://doi.org/10.1021/ja00284a003.

(50) Collin, J. P.; Jouaiti, A.; Sauvage, J. P. Electrocatalytic Properties of (Tetraazacyclotetradecane)Nickel(2+) and Ni2(Biscyclam)4+ with Respect to Carbon Dioxide and Water Reduction. *Inorg. Chem.* **1988**, *27* (11), 1986–1990. https://doi.org/10.1021/ic00284a030.

(51) Song, J.; Klein, E. L.; Neese, F.; Ye, S. The Mechanism of Homogeneous CO2 Reduction by Ni(Cyclam): Product Selectivity, Concerted Proton–Electron Transfer and C–O Bond Cleavage. *Inorg. Chem.* **2014**, *53* (14), 7500–7507. https://doi.org/10.1021/ic500829p.

(52) Fujihira, M.; Hirata, Y.; Suga, K. Electrocatalytic Reduction of CO2 by Nickel(II) Cyclam: Study of the Reduction Mechanism on Mercury by Cyclic Voltammetry, Polarography and Electrocapillarity. *J. Electroanal. Chem. Interfacial Electrochem.* **1990**, *292* (1), 199–215. https://doi.org/10.1016/0022-0728(90)87336-I.

Chapter 1: Translating Aqueous CO₂ Hydrogenation Activity to Electrocatalytic Reduction with a Homogeneous Cobalt Catalyst

1.1 Introduction

The reduction of CO_2, either through hydrogenation or electrochemical pathways, is an attractive route to non-fossil carbon products,.[1–3] Hydrogenation catalysts typically generate a metal hydride intermediate from hydrogen and a base (**Scheme 1.1**, red). The parallel electrochemical 'hydrogenation' route uses two electrons from the electrode and a proton from solution to generate equivalent metal hydrides (**Scheme 1.1**, blue). An advantage of electrochemical reduction is that it directly uses electricity for CO_2 reduction instead of using H_2 as an intermediary reductant.
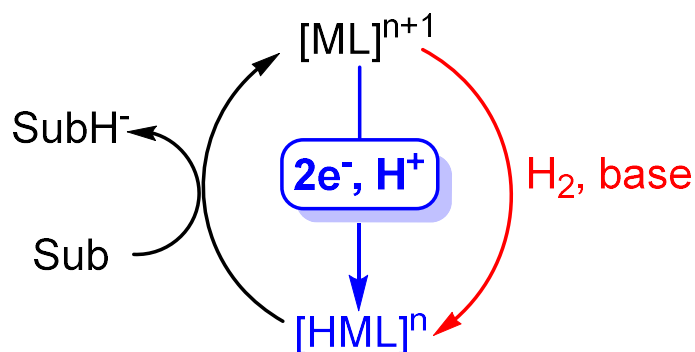
Scheme 1.1. Metal hydride generation through hydrogenation (**red**) vs electrochemical methods (**blue**).

Extensive work has been performed on the development of both molecular CO_2 hydrogenation catalysts and electrocatalysts. However, there are few examples of translating reactivity between these two reduction mechanisms.[4,5] To further research in this area, the aqueous CO_2 hydrogenation catalyst $[Co(dmpe)_2(H)]^{2+}$ (**2**) (dmpe = 1,2-*bis*(dimethylphosphino)ethane) was investigated for electrocatalytic reduction. **2** exhibits one of highest activities for a first-row transition metal catalyst in water.[6–8] The proposed hydrogenation mechanism is depicted in red in **Scheme 1.2**. The proposed electrocatalytic mechanism is depicted in blue in **Scheme 1.2**.
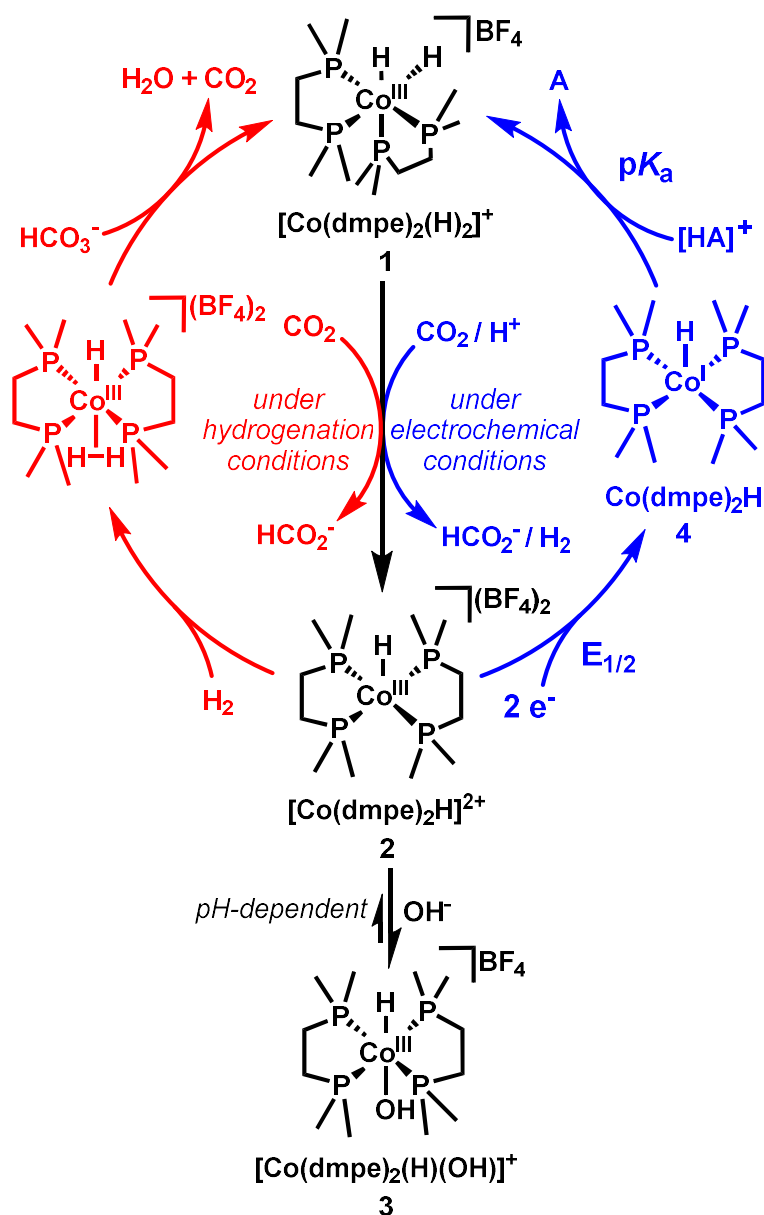
Scheme 1.2. Proposed electrocatalytic cycle and hydrogenation catalysis cycle for CO_2 reduction using $[Co(dmpe)_2(H)_2][BF_4]_2$ (**1**).

1.2 Results

1.2.1 Synthesis and characterization of $[Co(dmpe)_2(H)_2][BF_4]$ (1)

The synthesis and characterization of the dihydride $[Co(dmpe)_2(H)_2][BF_4]$ (**1**), $[Co(dmpe)_2H][BF_4]_2$ (**2**), $[Co(dmpe)_2(H)(OH)][BF_4]$ (**3**), and $Co(dmpe)_2H$ (**4**) were previously reported.[6,9] Attempts to synthesize $[Co(dmpe)_2(H)_2][BF_4]$ (**1**) by the published method, reaction

of $[Co(dmpe)_2][BF_4]_2$ (**2**) with KC_8 in acetonitrile under 1 atm H_2, resulted in the formation of an

unidentified side product which could not be separated from **1**. Instead, $[Co(dmpe)_2(H)_2][BF_4]$

(**1**) was synthesized using $Co(C_5(CH_3)_5)_2$ as the reductant and then exposed the solution to 1 atm

of H_2. $[Co(dmpe)_2(H)_2][BF_4]$ (**1**) was further characterized by low temperature $^{31}P\{^1H\}$, ^{31}P, and

^1H NMR spectroscopy (**Figures 1.1-1.4**) and UV-Vis characterization of $[Co(dmpe)_2(H)_2]^+$ (**1**)

and $[Co(dmpe)_2(OH)H][BF_4]$ (**3**) (**Figures 1.5-1.6**).

As previously reported, the $^{31}P\{^1H\}$ spectrum for $[Co(dmpe)_2(H)_2][BF_4]$ has two characteristic

broad peaks at room temperature likely due to the fluxionality of the dmpe ligands.[10] The

broadness may also be attributed to *cis-trans* isomerization or quadrupolar coupling to the ^{59}Co

nucleus.[11,12] Low temperature ^{31}P and $^{31}P\{^1H\}$ spectra were obtained in an attempt to further

characterize $[Co(dmpe)_2(H)_2][BF_4]$ and measure the ^{31}P-^1H coupling with the hydride. When

cooled to 183K, the peaks sharpen, suggesting that the ligands are less fluxional than at room

temperature (**Figure 1.1**). However, even at 183K, both the $^{31}P\{^1H\}$ and ^{31}P spectra look similar

– no ^{31}P-^1H coupling is observed in the phosphorus spectrum even in the absence of ^1H

decoupling (**Figure 1.2**).

At 183K, the hydride peak of $[Co(dmpe)_2(H)_2][BF_4]_2$ resolves into a multiplet in the ^1H

NMR at -14.4 ppm (**Figure 1.3**). At 183K, $^1H\{^{31}P\}$ experiments show that the multiplet for the

hydride peak at -14.4 ppm collapses into a singlet when the decoupling is irradiated at 58.5 ppm

in the ^{31}P spectrum (**Figure 1.4**), suggesting that the splitting normally observed in the ^1H

spectrum does arise from ^{31}P-^1H coupling. The magnitude of this coupling is likely too small to

observe in the ^{31}P spectrum since the broad ^{31}P feature is 2 ppm wide while the widest expected

doublet (J = 93 Hz) would result in a peak separation of 0.38ppm.
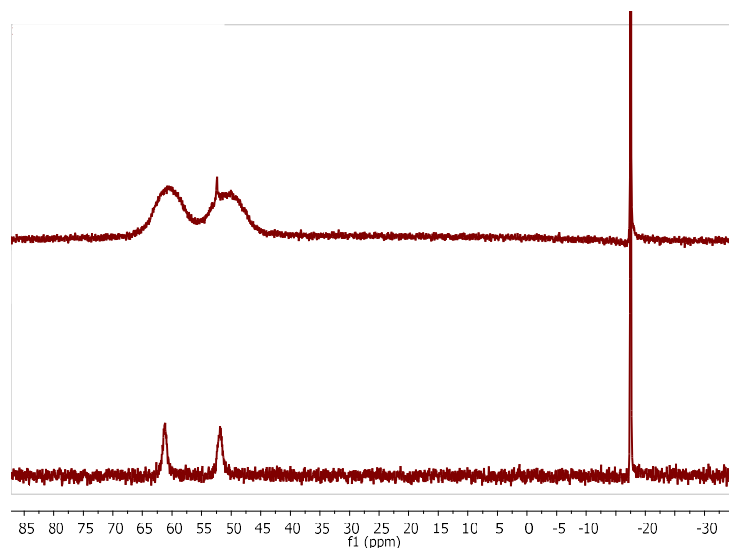
Figure 1.1. *Top:* $^{31}P\{^1H\}$ spectra of $[Co(dmpe)_2(H)_2][BF_4]$ (**1**) in THF at 298K, referenced to an external standard of triphenylphosphate. *Bottom:* $^{31}P\{^1H\}$ spectra of $[Co(dmpe)_2(H)_2][BF_4]$ (**1**) in THF at 183K, referenced to an external standard of triphenylphosphate.
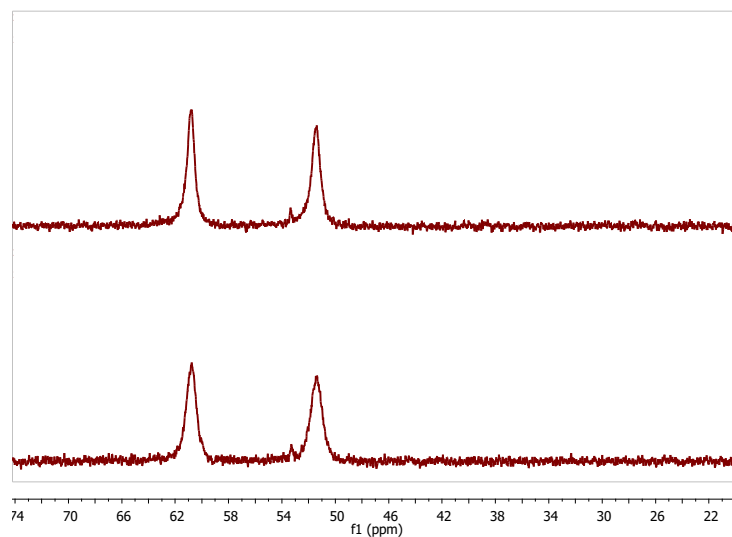
Figure 1.2. *Top*: $^{31}P\{^1H\}$ spectrum of $[Co(dmpe)_2(H)_2][BF_4]$ (**1**) at 183 K with a small impurity at 52.4 ppm in THF, referenced to an external standard of triphenylphosphate. *Bottom*: ^{31}P spectrum of $[Co(dmpe)_2(H)_2][BF_4]$ (**1**) at 183 K, referenced to an external standard of triphenylphosphate.
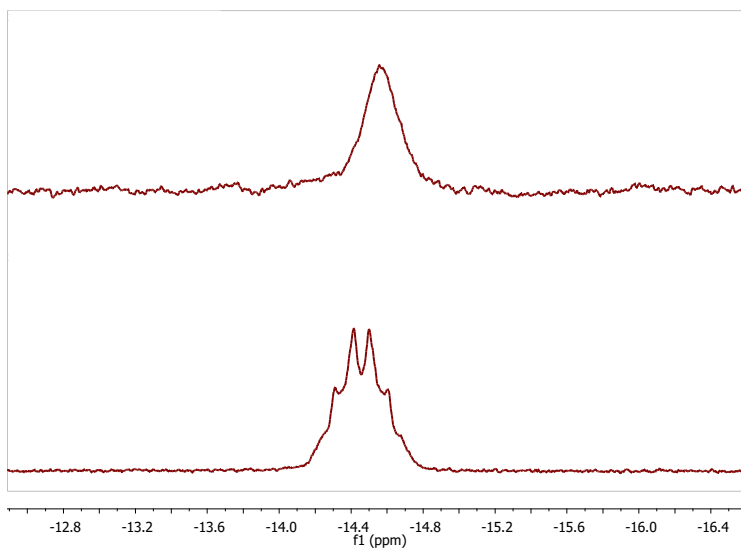
Figure 1.3. *Top*: Hydride region of ¹H spectrum of [Co(dmpe)₂(H)₂][BF₄] (**1**) at 298K. *Bottom*: Hydride region of ¹H spectrum of [Co(dmpe)₂(H)₂][BF₄] (**1**) at 183 K.
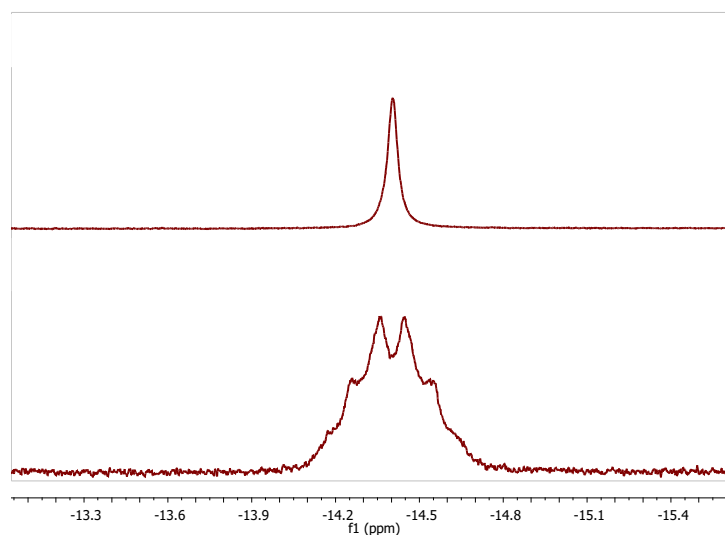
Figure 1.4. *Top*: Hydride region of ¹H spectrum of [Co(dmpe)₂(H)₂][BF₄] (**1**) at 183 K with ³¹P decoupling at 58 ppm. *Bottom*: Hydride region of ¹H spectrum of [Co(dmpe)₂(H)₂][BF₄] (**1**) at 183 K with no decoupling.
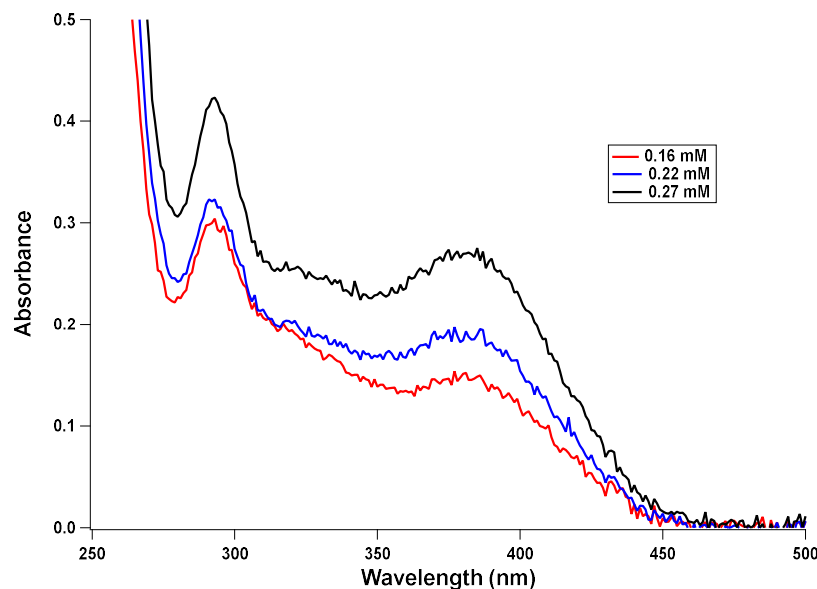
Figure 1.5. UV-Vis spectra of increasing amounts of $[Co(dmpe)_2(H)_2][BF_4]$ (**1**) in 0.20 M phosphate buffer used to calculate ε from the Beer-Lambert law ($A = \varepsilon bc$ where b = 1 cm and c = concentration in M). $[Co(dmpe)_2(H)_2][BF_4]$ (**1**) has two features in the UV-Vis spectrum: a broad peak at 385 nm with $\varepsilon = 1.1 \times 10^4$ $M^{-1}cm^{-1}$ as well as a sharper peak at 293 nm with $\varepsilon = 1.1 \times 10^4$ $M^{-1}cm^{-1}$. Spectra were recorded using a 1 cm quartz cuvette with an Agilent Cary 60 UV-Vis spectrophotometer fitted with an Agilent fiber optic coupler connected to an Ocean Optics CUV 1 cm cuvette holder in a glovebox under an atmosphere of N_2.
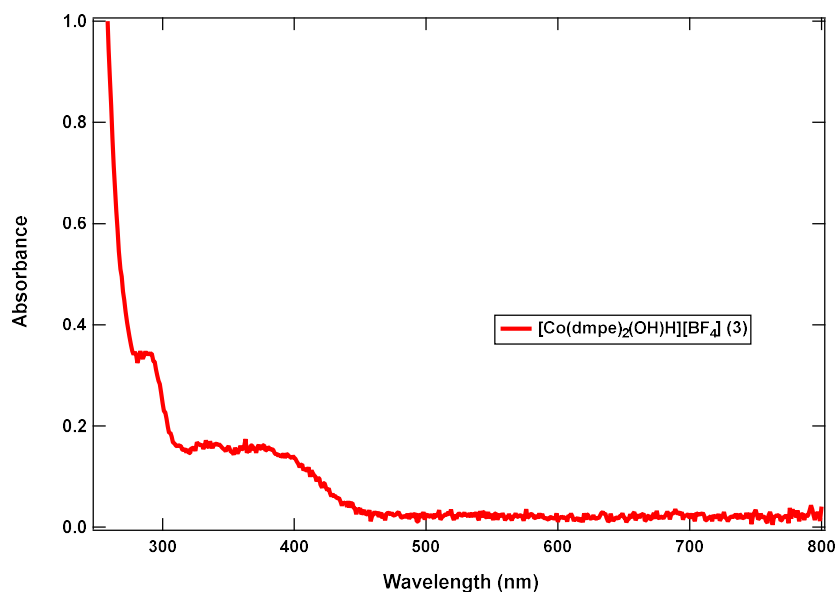
Figure 1.6. UV-Vis spectrum of a 0.20 mM solution of $[Co(dmpe)_2(OH)H][BF_4]$ (**3**) in 0.2 M phosphate buffer. $[Co(dmpe)_2(OH)H][BF_4]$ (**3**) has two features in the UV-Vis spectrum: a very broad peak at 376 nm, and a sharper peak at 291 nm. The spectrum was recorded using a 1 cm quartz cuvette with an Agilent Cary 60 UV-Vis spectrophotometer fitted with an Agilent fiber optic coupler connected to an Ocean Optics CUV 1 cm cuvette holder in a glovebox under an atmosphere of N_2.

21

1.2.2 pK_a determination of [Co(dmpe)$_2$(H)$_2$][BF$_4$] (1)

The pK_a of **1** was measured to determine the pH conditions necessary to generate the active catalyst from the reduced complex Co(dmpe)$_2$H (**4**) (**Scheme 1.2**). When [Co(dmpe)$_2$(H)$_2$]$^+$ (**1**) is dissolved in pH 13.3, 13.2, and 13.1 phosphate buffer, it is partially deprotonated to form Co(dmpe)$_2$H (**4**) (**Figure 1.7**). Based on the equilibrium product distribution between **1** and **4** measured at these different pH values, the pK_a of [Co(dmpe)$_2$(H)$_2$]$^+$ (**1**) is 12.9(5), providing the upper bound for the pH required to generate the hydride *in situ*.
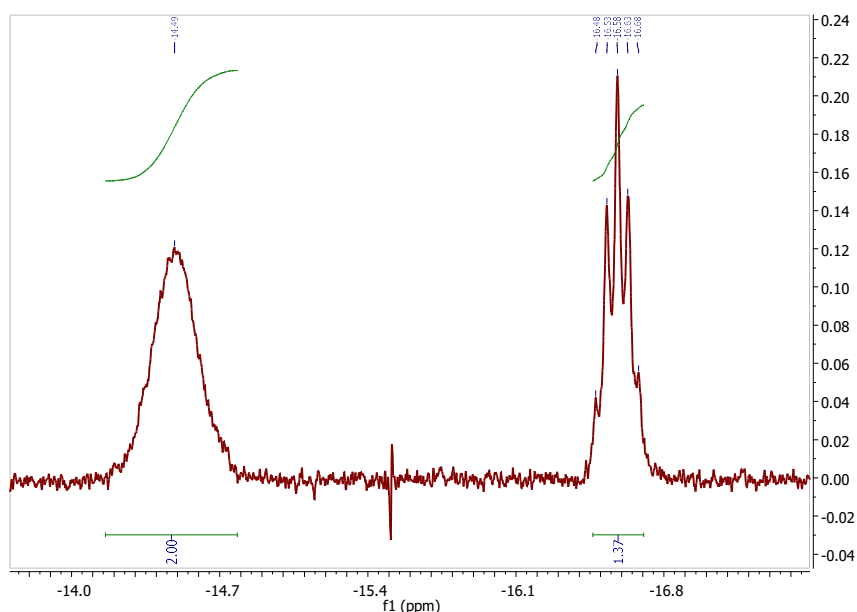
Figure 1.7. ^{1}H spectrum acquired in d_8-THF showing the hydride region and product distribution between [Co(dmpe)$_2$(H)$_2$]$^+$ and Co(dmpe)$_2$H after [Co(dmpe)$_2$(H)$_2$]$^+$ was placed in pH 13.3 phosphate buffer (0.4 M) for 96h. Due to the insolubility of Co(dmpe)$_2$H in H$_2$O, NMR spectra were acquired in THF.

1.2.3 Electrochemical behavior

Electrochemical characterization was conducted on solutions of [Co(dmpe)$_2$(OH)H][BF$_4$] (**3**) below pH 12 to ensure that Co(dmpe)$_2$H (**4**) would fully protonate to form [Co(dmpe)$_2$(H)$_2$]$^+$ (**1**) upon reduction. In water, [Co(dmpe)$_2$(OH)H][BF$_4$] (**3**) has a pH-dependent equilibrium with [Co(dmpe)$_2$H][BF$_4$]$_2$ (**2**) (**Scheme 1.2**) due to hydroxide coordination.[6] However, at the pH

22

conditions studied by cyclic voltammetry (7.9 and 9.9), only **3** is observed in solution by $^{31}P\{^{1}H\}$ NMR.

The reduction of $Co(dmpe)_2(OH)H]^+$ (**3**) at pH 9.9 in bicarbonate buffer under N_2 features two reduction events (**Figure 1.8**). An irreversible reduction at -0.96 V vs. SCE is attributed to the $Co^{3+/2+}$ reduction and a second event at -1.58 V is attributed to the $Co^{2+/+}$ reduction (**Figure 1.8, red trace**). In bicarbonate buffer under N_2 (pH 9.9), the larger current associated with the $Co^{2+/+}$ reduction compared to the $Co^{3+/2+}$ reduction is attributed to catalytic H_2 production, which was verified by controlled potential electrolysis (*vide infra*). The current increase is adjacent to background H_2 production at the electrode. Under CO_2-saturated conditions, the bicarbonate solution acidifies to pH 7.9. The $Co^{3+/2+}$ reduction shifts anodically (-0.92 V vs. SCE) but remains irreversible (**Figure 1.8**). The onset potential for the $Co^{2+/+}$ reduction also shifts anodically by about 65 mV, and a modest increase in current is observed at -1.58 V vs. SCE (**Figure 1.8**). These data are summarized in **Table 1.1**.

Table 1.1. Electrochemical data for [Co(dmpe)₂(OH)H]⁺ (3) in bicarbonate buffered solutions.ᵃ

	Under N_2 (pH 9.9)		Under CO_2 (pH 7.9)	
	E_{pc} (V vs. SCE)	E_{pa} (V vs. SCE)	E_{pc} (V vs. SCE)	E_{pa} (V vs. SCE)
Co³⁺/²⁺	-0.96	---	-0.92	---
Co²⁺/⁺	-1.58	-1.48	-1.58	---

ᵃCyclic voltammograms were performed at 250 mV/s using 0.4 M bicarbonate buffer under N_2 (pH 9.9), or saturated CO_2 in 0.4 M bicarbonate buffer (pH 7.9) with the buffer acting as electrolyte. The reference electrode was a saturated calomel electrode (SCE); the working and counter electrodes were glassy carbon disk and rod respectively.

The peak current increases linearly with the square root of scan rate for both reductions, indicating that the analyte is homogeneous and freely diffusing (**Figure 1.9**). The first reduction at -0.96 V is irreversible for scan rates between 50 mV/s to 1000 mV/s (**Figure 1.10**).
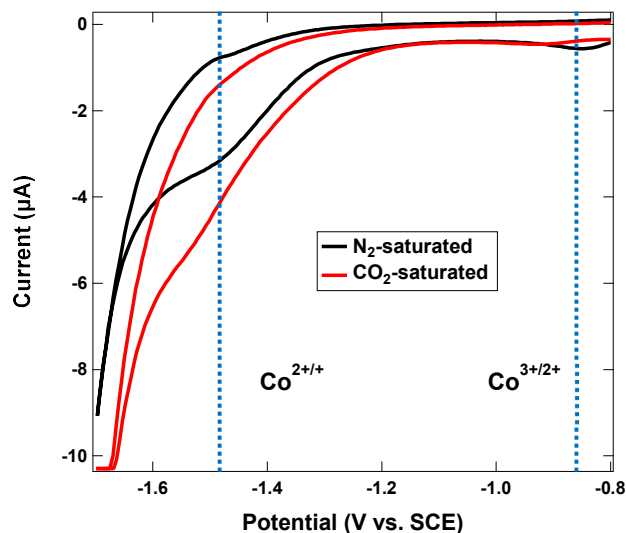
Figure 1.8. Cyclic voltammograms of 1 mM [Co(dmpe)₂(OH)H]⁺ in 0.4 M bicarbonate buffer (pH 9.9, red trace) at 250 mV/s and after CO_2 addition (pH 7.9, black trace) using a glassy carbon disk working electrode. The reductions attributed to $Co^{3+/2+}$ and $Co^{2+/+}$ are labelled with blue dotted lines.
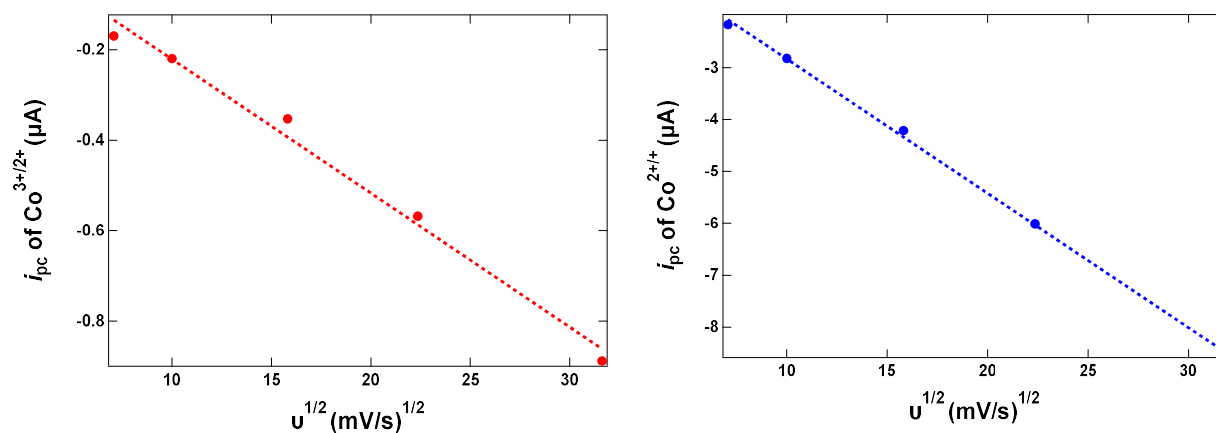
Figure 1.9. *Left*: Variable scan rate plot of i_{pc} of the $Co^{3+/2+}$ feature of [Co(dmpe)₂(OH)H]⁺ from 50 mV/s to 1000 mV/s. R² = 0.989. *Right*: Variable scan rate plot of i_{pc} of the $Co^{2+/+}$ feature of [Co(dmpe)₂(OH)H]⁺ from 50 mV/s to 1000 mV/s. R² = 0.999 Plots show a linear relationship with the square root of scan rate, indicating that the species is freely diffusing in solution.

24
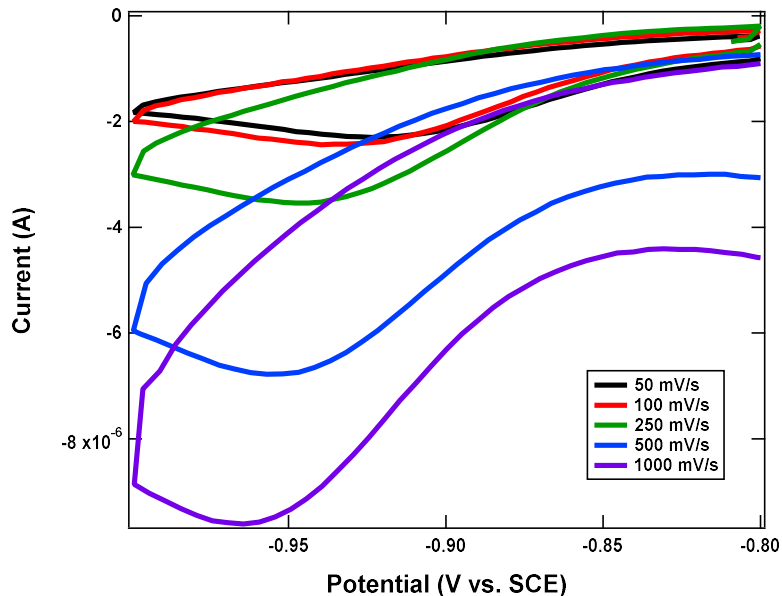
Figure 1.10. Cyclic voltammograms of the $Co^{3+/2+}$ couple of $[Co(dmpe)_2(OH)H]^+$ in bicarbonate buffer under N_2 (pH 9.9) do not show reversibility at faster scan rates.

Under a N_2 atmosphere at pH 9.9, no oxidation peak is observed for the $Co^{2+/+}$ reduction event at slow scan rates (**Figure 1.11, top**). A return oxidation peak is observed at scan rates >100 mV/s. (**Figure 1.11, bottom**). In a CO_2-saturated solution at pH 7.9, the oxidation peak at −1.48 V is not observed at faster scan rates, even at scan rates up to 1000 mV/s (**Figure 1.12**).
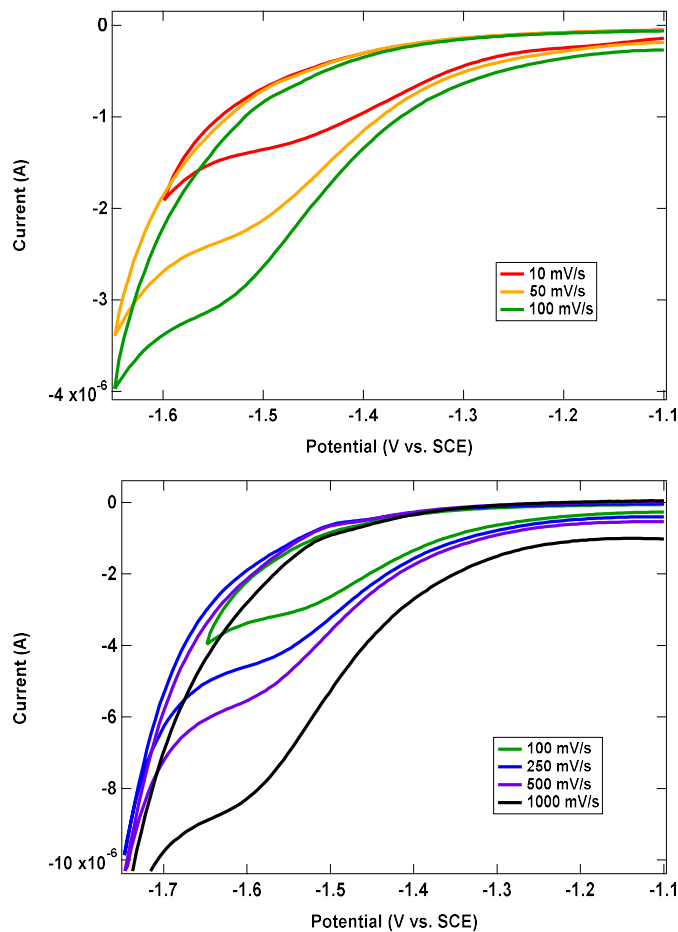
Figure 1.11. For the $Co^{2+/+}$ couple of $[Co(dmpe)_2(OH)H]^+$ in bicarbonate buffer (pH 9.9), an oxidation event at -1.48 V is not observed at slow scan rates below 100 mV/s (*top*) but is observed when scanning at 100 mV/s and above (*bottom*).
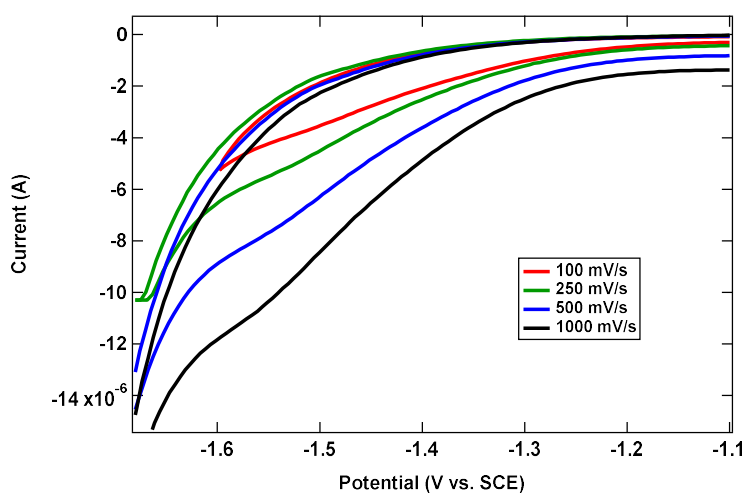
Figure 1.12. No oxidation peak at -1.48 V is observed for $[Co(dmpe)_2(OH)H]^+$ after CO_2 addition (pH 7.9), even at fast scan rates.

Another reduction event is only observed in bicarbonate buffer at pH 9.9, or in phosphate buffer after CO_2 is added to the solution, upon which the pH lowers to 7.9 and bicarbonate is produced *in situ*. This quasi-reversible reduction event occurs at −0.62 V vs. SCE. This feature is not observed in phosphate buffer at pH 7.9 with no added CO_2 (**Figure 1.13**), suggesting that this feature may be due to bicarbonate interaction with the cobalt species, but no catalysis is observed at this event.
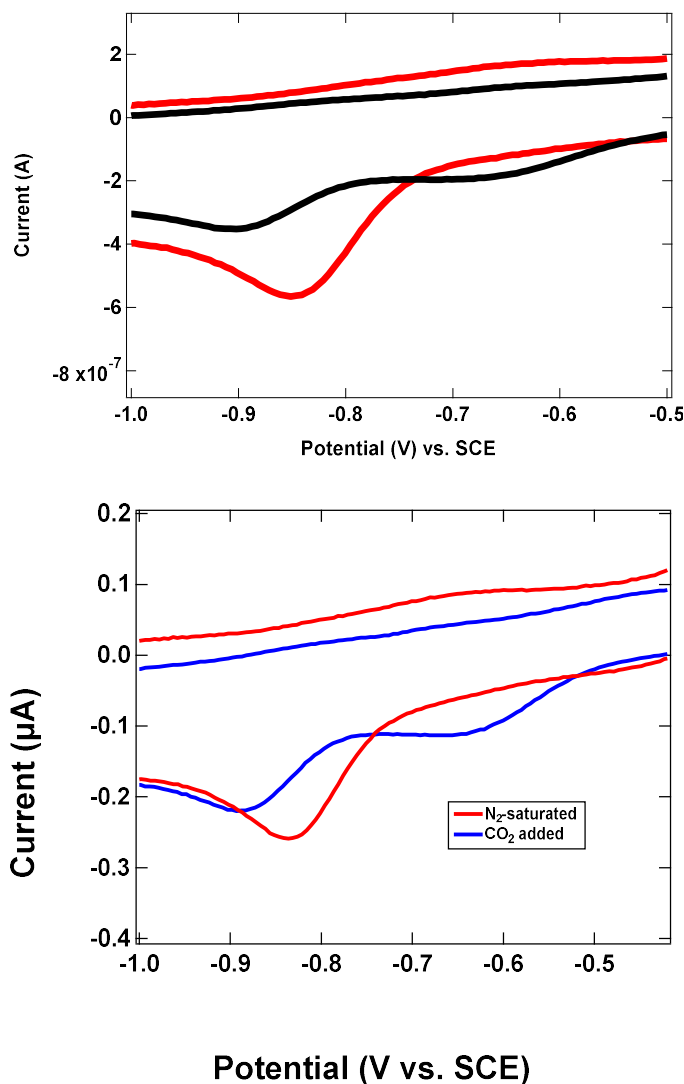
Figure 1.13. *Top*: Cyclic voltammograms of [Co(dmpe)2(OH)H]+ in 0.4 M phosphate buffer at pH 7.9 (red) and 0.4 M bicarbonate buffer at pH 9.9 (black) showing an additional redox event at −0.62 V vs. SCE in bicarbonate buffer which is not observed in phosphate buffer. *Bottom*: Cyclic voltammograms of [Co(dmpe)2(OH)H]+ in 0.4 M phosphate buffer at pH 7.9 under N2 (red) and CO2 (blue) showing an additional redox event at −0.62 V vs. SCE after CO2 addition which is not observed under N2. Experiments were conducted using a glassy carbon working electrode and scanned at 250 mV/s.

1.2.4 Controlled potential electrolysis

Controlled potential electrolysis (CPE) experiments were performed with **3** at −1.50 V vs.

SCE using a 0.2 M sodium carbonate solution saturated with CO_2 to the appropriate pH value.

Results from these experiments are summarized in **Table 1.2**. Formate was quantified by [1]H

NMR and H_2 by gas chromatography. Under electrolytic conditions, the Faradaic yield for

formate is optimized at pH 7.8. At other pH conditions, the Faradaic efficiency for H_2 is higher

than that of formate. Electrolysis was also performed on blank samples containing only

carbonate buffer acidified to the appropriate pH using CO_2 at −1.50 V vs. SCE. H_2 was observed

under these conditions, but no formate was observed in solution for electrolyses without **3**

present.

Table 1.2. Summary of CPE data with [Co(dmpe)$_2$(OH)H]$^+$ (3).[a]

	Charge passed (C)	Faradaic yield (% H$_2$)	Faradaic yield (% HCO$_2^-$)
pH 7.2	6.7 ± 0.5	52 ± 6	40 ± 7
pH 7.8	5.3 ± 0.8	47 ± 5	54 ± 4
pH 8.1	5.8 ± 0.5	57 ± 3	37 ± 2
pH 8.7	5.2 ± 0.7	62 ± 2	22 ± 5

[a]Experiments were conducted with 2 mM of analyte (0.01 mmol) using a glassy carbon rod working electrode, a carbon fabric counter electrode, and a SCE reference electrode in 0.2 M CO_2-saturated carbonate buffer. The solutions were electrolyzed at -1.50 V vs. SCE for 5 h over a mercury pool in the working electrode compartment.

1.2.5 Calculation and discussion of overpotential during catalysis

The overpotential for this catalytic system was calculated as the difference between the applied

potential during electrolysis and the thermodynamic potential of the reduction of CO_2 to

formate.

$$CO_2(g) + 2\,e^- + H^+ \rightleftharpoons HCO_2^-(aq) \quad E^{o'} = -0.43\,\text{V vs. NHE @ pH 7} \qquad \text{(Eq 1.1)}$$

$$CO_2(g) + 2\,e^- + H^+ \rightleftharpoons HCO_2^-(aq) \quad E^{o'} = -0.46\,\text{V vs. NHE @ pH 8} \qquad \text{(Eq 1.2)}$$
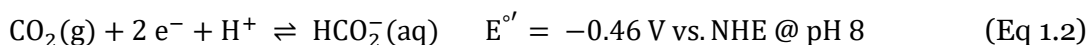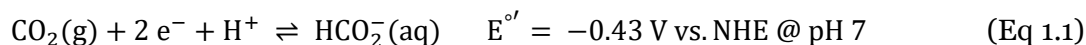
Since the reaction of interest is a 2 e$^-$/1 H$^+$ process, the thermodynamic potential shifts by 30 mV/pH unit at these conditions.

For [Co(dmpe)$_2$(OH)H]$^+$, the applied potential of -1.50 V vs. SCE corresponds to -1.26 V vs. NHE. At pH 8 which is approximately where formate selectivity is highest, the difference between the applied potential and the thermodynamic potential is 800 mV. In comparison, two selective catalysts for CO$_2$ reduction to HCO$_2^-$, [Ir(POCOP^{tBu})(H)]$^+$ and [Fe$_4$N(CO)$_{12}$]$^-$ (**Chart 1.1**), have overpotentials of 950 mV at pH 7 and 500 mV pH 8 respectively.
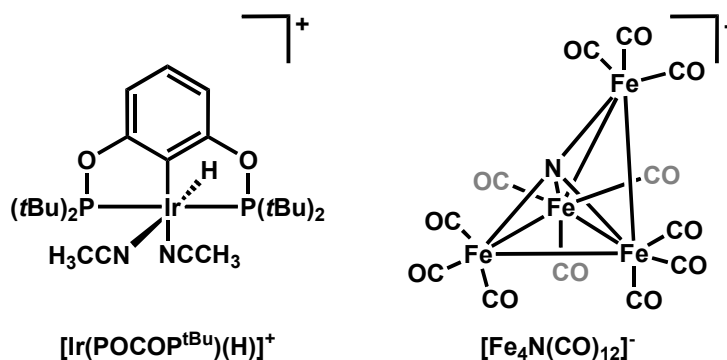
Chart 1.1. Examples of selective electrocatalysts for the reduction of CO$_2$ to HCO$_2^-$.

For [Fe$_4$N(CO)$_{12}$]$^-$, the applied potential of -1.20 V vs. SCE corresponds to -0.96 V vs. NHE. At pH 7, the difference between the applied and thermodynamic potential is 530 mV. At pH 8, the difference is 500 mV.[13] For Ir(POCOP^{tBu}), the applied potential for the highest formate selectivity was -1.41 V vs. NHE, which corresponds to an overpotential of 950 mV between the applied and thermodynamic potentials at pH 7. Electrolysis at other pH conditions was not reported.[14]

The energetic requirements for electrocatalytic reduction may exceed what is expected based on hydrogenation activity. For example, Waymouth and coworkers have translated the activity of reversible ruthenium hydrogenation catalysts to electrocatalytic alcohol oxidation, but observe a high overpotential. The overpotential is postulated to arise from the use of a very

strong base.[14] Based on prior work in acetonitrile, catalysis was expected to occur at low

overpotentials because hydride transfer to CO_2 is nearly ergooneutral.[15] However, the pH values

required to generate **1** limits the operational range of the catalyst.

1.2.6 Stoichiometric hydride transfer from [Co(dmpe)$_2$(H)$_2$][BF$_4$] (1)

To understand why pH-dependent product selectivity was observed, additional experimental

and thermochemical analyses were performed.

Stoichiometric hydride transfer studies were conducted with $[Co(dmpe)_2(H)_2]^+$ (**1**) to

compare the competitive reactivity with CO_2 or H^+ under 1 atmosphere of CO_2 under various pH

conditions. Formate was quantified by ^{1}H NMR and H_2 by gas chromatography. The yields from

these experiments using $[Co(dmpe)_2(H)_2]^+$ indicate that H_2 is the favored species under most

conditions (**Table 1.3**). Formate reaches near-parity at pH 7.8.

Table 1.3. Average yields from 3 trials of stoichiometric hydride transfer from

[Co(dmpe)$_2$(H)$_2$]$^+$ (0.01 mmol) to either H$^+$ or CO$_2$.[a]

	% yield H$_2$	% yield HCO$_2^-$
pH 7.2	60 ± 9	33 ± 5
pH 7.8	47 ± 4	43 ± 7
pH 8.1	56 ± 6	47 ± 3
pH 8.7	66 ± 7	28 ± 4

[a]Reactions were conducted in 0.2 M carbonate solutions with CO_2 added to reach the
appropriate pH.

1.2.7 Controlled potential electrolysis using a mercury pool electrode

The stoichiometric reactivity suggests that protonation of the cobalt hydride to form H_2 is a

significant source of consumption of $[Co(dmpe)_2(H)_2]^+$ between pH 7 and pH 9. Consequently, it

is suggested that the H_2 evolution observed during electrolysis likely arises from the catalyst

itself, and not the electrode, which is further corroborated by bulk electrolysis experiments

using a mercury pool working electrode. Mercury was chosen because the solvent window in

water is shifted more negative for Hg than for glassy carbon, which means that H_2 production is less favorable for Hg compared to glassy carbon.[16] However, selectivity for formate did not improve with this electrode and a small amount of H_2 was still produced, indicating that the H_2 observed during electrolysis with $[Co(dmpe)_2(OH)(H)]^+$ in solution comes from the catalyst, not the glassy carbon electrode (**Table 1.4**).

Table 1.4. Summary of CPE data using a mercury pool working electrode.[a]

	Charge passed (C)	**H_2 (mmol)**	**HCO_2^- (mmol)**	**Faradaic yield (% H_2)**	**Faradaic yield (% HCO_2^-)**
pH 7.9	0.82	0.0026	0.0015	62	36
pH 8.1	0.74	0.0029	Not detected	70	N/A

[a]Experiments were conducted with 2 mM of analyte (0.015 mmol) using a mercury pool working electrode, a carbon fabric counter electrode, and a SCE reference electrode in 0.2 M CO_2-saturated carbonate buffer. The mercury pool working electrode was created by submerging a 1 mm glassy carbon disk electrode into a 1 mL pool of mercury at the bottom of a customized H-cell. The solutions were electrolyzed at -1.50 V vs. SCE for 6 h over a mercury pool. H_2 was quantified by GC, while formate was quantified by ^1H NMR using an internal reference.

1.3 Discussion

The mixed product selectivity can be rationalized with the thermochemistry of hydride transfer to CO_2 and hydride transfer to H^+. This hydrogen evolution reaction (HER) typically proceeds through the protonation of metal hydride intermediates.[17] In order to rationalize the mixed product selectivity, the free energies for the reaction of H^+ and CO_2 with $[Co(dmpe)_2(H)_2]^+$ (**1**) (blue center line, **Scheme 1.2**) were analyzed. The free energy for all reactions involving protonation of a metal hydride to form H_2 relies on the hydricity the former, proton activity (pH or pK_a) of the solution, and heterolytic cleavage energy of H_2 according to eq 1.3.[18]

$$\Delta G^o_{HER} = \Delta G^o_{H^-} + 1.364 * pK_a - \Delta G^o_{H_2} \qquad \text{(Eq 1.3)}$$

The free energy for the CO_2 reduction reaction (CO2RR) via hydride transfer to form formate only relies on the relative hydricities of the metal hydride and formate (eq 1.4).[18]

$$\Delta G^o_{CO_2 RR} = \Delta G^o_{H^-(MH)} - \Delta G^o_{H^-(HCO_2^-)} \qquad \text{(Eq 1.4)}$$

In many cases, particularly in the well-studied group 10 class of bis(diphosphine) metal hydrides, the absence of a ligand coordination step concomitant with hydride transfer results in a hydricity value of a given metal hydride that is invariant with pH.[19,20] As a result, there are conditions in which the reactivity of a metal hydride can reliably be predicted to be exergonic with CO_2 and endergonic with H^+, leading to product selectivity for the former.

In contrast, the reactivity of complexes that undergo ligand association after hydride transfer are do not remain invariant, especially under aqueous conditions.[21] As previously described by Wiedner and coworkers, the hydricity value of $[Co(dmpe)_2(H)_2]^+$ (**1**) is pH-dependent in water. The formation of the hydroxide bound species, $[Co(dmpe)_2(OH)H]^+$ (**3**) (eq 1.5) increases the *effective* hydricity of **1**, as the free energy includes formation of the Co-OH bond.[22,23] Increasing amounts of OH^- in solution at higher pH values therefore *increases* the hydricity of $[Co(dmpe)_2(H)_2]^+$ according to eq 3, where $\Delta G^o_{H^-}$ is 14.0 kcal/mol as determined by a thermodynamic cycle (dashed blue line, Figure 2).[6]

$$[Co(dmpe)_2(H)_2]^+ \; + \; OH^- \; \rightleftharpoons \; [Co(dmpe)_2(OH)H]^+ \; + \; H^-$$

$$\Delta G^o_{H^-(eff)} = \Delta G^o_{H^-} - 1.364 * pOH \qquad \text{(Eq. 1.5)}$$

Because the effective $\Delta G^o_{H^-}$ of $[Co(dmpe)_2(H)_2]^+$ (**1**) is pH dependent (pOH = 14-pH), the free energy of H^- transfer to CO_2 is also pH dependent, while the free energy of HER remains the same value at all pH values. As a result, the free energy of hydrogen evolution ΔG^o_{HER} is −1.1 kcal/mol at all pH values (black line, **Figure 1.14**).
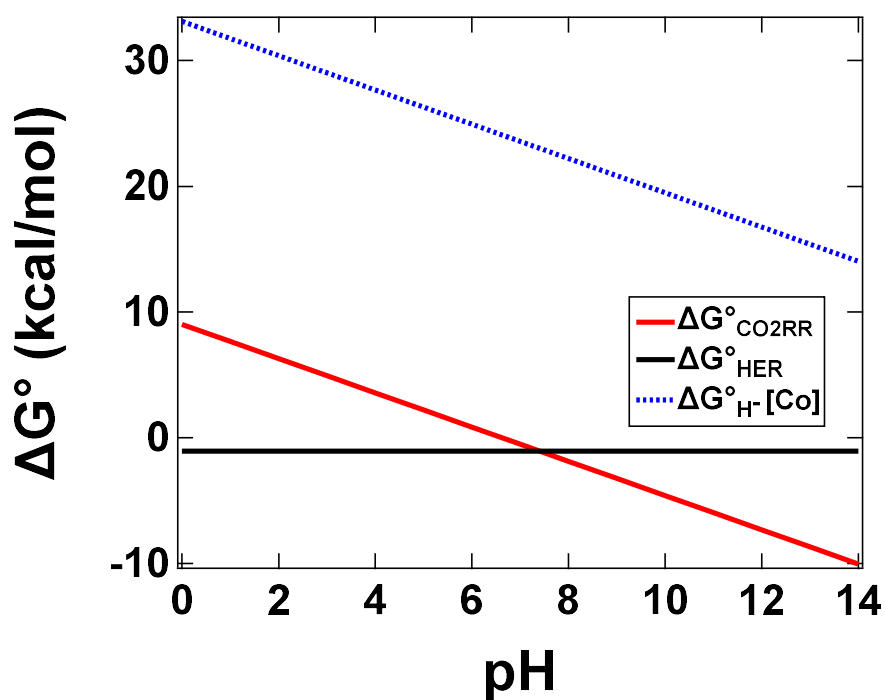
Figure 1.14. Thermodynamic relationships for CO_2 reduction, H_2 evolution, and $\Delta G°_{H^-(eff)}$ for $[Co(dmpe)_2(H)_2]^{2+}$ (**1**). $\Delta G°_{CO2RR}$ and $\Delta G°_{HER}$ are calculated based on Eqs. 1.3 and 1.4 using $\Delta G°_{H^-(eff)}$ of $[Co(dmpe)_2(H)_2]^{2+}$ (**1**).

While the free energy of the reaction of $[Co(dmpe)_2(H)_2]^+$ with CO_2 is more exergonic than H^+ above pH 7.4, stoichiometric and faradaic yields indicate that H_2 production is still the predominant reaction above pH 8. Data from cyclic voltammograms are also in agreement with this; despite acidifying the solution by adding CO_2 as a substrate, there is only a modest increase (< 40%) in the amount of current passed at −1.58V vs. SCE (**Figure 1.8**).

Although the free energy for hydride transfer from $[Co(dmpe)_2(H)_2]^+$ to CO_2 becomes more favorable at higher pH, the selectivity for formate vs H_2 is reduced. This discrepancy may arise from the different concentrations of bicarbonate and dissolved CO_2 at higher pH values. Prior work with aqueous CO_2 hydrogenation catalysts have demonstrated significantly higher turnover frequencies using 34 atm of a gaseous 1:1 H_2/CO_2 mixture than with bicarbonate alone in solution, suggesting CO_2 is more easily reduced than bicarbonate.[24,25] However, the effective concentration of CO_2 is only about 1/10th that of HCO_3^- at pH 7.8 and the concentration of CO_2 further decreases

relative to HCO_3^- as the pH increases.[26,27] Thus, it is suggested that the lower concentration of CO_2 at higher pH values are an important determinant in aqueous selectivity.

A complicating factor in electrochemical reduction that does not exist in hydrogenation is the direct reduction of protons to hydrogen.[28] Despite the challenges in favoring CO_2 reduction versus H_2 evolution in aqueous solvents, selective homogenous CO_2 reduction catalysts have been reported. In an Ir(POCOP) system developed by Brookhart and coworkers, the current passed at E_{pc} (-1.3 V vs. SCE) under 1 atm CO_2 was 2.2 times greater than the current passed under 1 atm Ar at the same scan rate.[29] The Ir system, unlike the Co system described here, demonstrated selective CO_2 reduction to formate with optimal selectivity at -1.65 V vs. SCE at pH 6.95. Computational work done by Goddard and coworkers indicates that the observed selectivity likely originates from kinetically disfavoring H_2 formation, possibly from the presence of *tert*-butyl groups inhibiting the approach of a water cluster.[30] An iron carbonyl cluster, [HFe-4N(CO)$_{12}$]$^-$ used by Berben and coworkers also demonstrates selective CO_2 reduction to formate. Like the Ir(POCOP) system, the free energy of H^+ and CO_2 reduction by the cluster is favorable. However, an Eyring analysis of the rate-determining hydride transfer step to CO_2 showed that the transition barrier was stabilized by almost 14 kcal/mol in H_2O compared to a 95:5 $MeCN/H_2O$ solution, which indicates that selectivity in this system also arises from kinetic considerations.[31] Thus, success in selective aqueous CO_2 reduction electrocatalysts have relied on favoring the kinetic reactivity of CO_2. Catalyst designs that can kinetically inhibit the hydrogen evolution reaction may be particularly valuable for aqueous catalysts.[32]

1.4 Conclusion

A hydrogenation catalyst for CO_2 reduction to formate was investigated as a potential electrocatalyst. Additional spectroscopic characterization of the hydride transfer species [Co(dmpe)$_2$(H)$_2$][BF$_4$] (**1**) was conducted. Conditions suitable for electrochemical regeneration of the active hydride species were determined. Data from controlled potential electrolysis and stoichiometric experiments indicate that the catalyst is most selective for formate at pH 7.8 but

still produces significant quantities of H_2. Thermodynamic considerations suggest that the lack of selectivity for formate likely results from hydroxide coordination upon hydride transfer, which renders HER favourable by 1.1 kcal/mol at all pH conditions.

1.5 Experimental Details

General Methods: All synthesis and manipulations were carried out under an inert atmosphere of dinitrogen in a Vacuum Atmospheres OMNI-Lab glovebox or using standard Schlenk techniques. Organic solvents used during synthesis and/or manipulations were degassed by sparging with argon and dried by passing through columns of neutral alumina or molecular sieves and stored over activated 3 Å molecular sieves. Water was obtained from a Barnstead Nanopure filtration system and was degassed under active vacuum. All deuterated solvents were purchased from Cambridge Isotope Laboratories, Inc. Deuterated solvents used for nuclear magnetic resonance (NMR) spectroscopic characterization were degassed via three freeze-pump-thaw (FPT) cycles and stored over activated 3 Å molecular sieves prior to use. All solvents and reagents were purchased from commercial vendors and used without further purification unless otherwise noted. Electrochemical studies under pure CO_2 atmospheres were performed using ultra high purity (99.999%) CO_2 that was passed through a VICI carbon dioxide purification column to eliminate residual H_2O, O_2, CO, halocarbons, and sulfur compounds. Buffer pH levels were adjusted using concentrated solutions of Na_2CO_3, H_3PO_4, or by additional CO_2 bubbling and measured using a Thermo Scientific Orion Star A216 pH meter.

Physical Methods: ^1H and $^{31}P\{^1H\}$ nuclear magnetic resonance (NMR) spectra were collected at 298K, unless otherwise noted, on a Bruker AVANCE 600 MHz spectrometer equipped with a BBFO cryoprobe. Low temperature ^1H and $^{31}P\{^1H\}$ NMR spectra were collected on a Bruker DRX 500 MHz spectrometer equipped with a BBO probe. Chemical shifts are reported in δ units notation in parts per million (ppm). ^1H spectra are referenced to the residual solvent resonances of the deuterated solvent. $^{31}P\{^1H\}$ spectra were referenced to H_3PO_4 at 0 ppm within XwinNMR

or Bruker's Topspin software, using the known frequency ratios (Ξ) of the ^{31}P standard to the lock signal of the deuterated solvent or referenced to an external standard of triphenylphosphate in a capillary. Manual shimming, Fourier transformation, and automatic spectrum phasing were performed using Xwin-NMR software when using the 500 MHz spectrometer. Spectra were analyzed and figures were generated using MestReNova 6.0.2 software. Peak integrations were calculated within MestReNova. Quantitative ^{1}H NMR experiments for formate detection were performed with a delay time of 60s and acquisition time of 5s. Room temperature electronic absorption spectra were recorded using a 1 cm quartz cuvette with an Agilent Cary 60 UV-Vis spectrophotometer fitted with an Agilent fiber optic coupler connected to an Ocean Optics CUV 1 cm cuvette holder in a glovebox under an inert atmosphere of N_2.

Electrochemistry: All measurements were performed on a Pine Wavedriver 10 bipotentiostat. Cyclic voltammetry was performed with a 1 mm diameter glassy carbon disc working electrode, a glassy carbon rod counter electrode, and a saturated calomel electrode (SCE) reference electrode. Internal resistance was measured for each solution using a current interrupt method, and resistance manually compensated for between 80-90% of the measured value for each voltammogram performed. All experiments were performed in degassed aqueous solutions with 1 mM analyte and 0.4 M phosphate, bicarbonate, or carbonate buffer with the buffer acting as supporting electrolyte. Samples for electrochemical studies performed under CO_2 atmosphere were prepared by sparging the analyte solution with solvent saturated carbon dioxide gas prior to measurement and the headspace above the solution was blanketed with CO_2 during each measurement.

Electrolysis: Controlled potential electrolysis experiments were performed in a custom H-cell with the working and counter compartments (16.1 and 8.0 mL respectively) separated by a medium porosity glass frit. The working and counter compartments were sealed with GL25 and GL18 open top caps with silicone/PTFE septa from Ace Glass. The working compartment

contained: 2.0 mM catalyst, 0.2 M carbonate buffer, a glassy carbon rod working electrode, the SCE reference electrode, and a mercury pool at the bottom of the compartment. The counter compartment contained an aqueous solution of 0.2 M carbonate buffer and a 1" x 2.25" piece of carbon fabric as the counter electrode. After the electrolysis period, the volume in the working compartment was measured. The formate concentration was determined by ^{1}H NMR after addition of an internal standard (sodium propane sulfonate) to a known volume of electrolysis solution. The headspace of the working compartment was sampled with a Restek A-2 Luer lock gas-tight syringe. Headspace hydrogen was quantified by gas chromatography on an Agilent 7890B instrument with a HP-PLOT Molesieve column (19095P-MS6, 30m x 0.530 mm, 25 mm) and TCD detector.

Synthesis of $[Co(dmpe)_2(H)_2][BF_4]$ (1): Precursor $[Co(dmpe)_2(MeCN)_2][BF_4]_2$ was synthesized per the literature procedure and recrystallized by vapor diffusion of diethyl (Et_2O) into an acetonitrile solution (MeCN).[9] The coordinated solvent was removed from the recrystallized material *in vacuo* to obtain $[Co(dmpe)_2][BF_4]_2$ as a green solid. $[Co(dmpe)_2][BF_4]_2$ (171 mg, 0.320 mmol) was dissolved in 20 mL of cold MeCN at −40°C in a 250 mL Schlenk flask, forming a dark red-brown solution of $[Co(dmpe)_2(CH_3CN)_2][BF_4]_2$ *in situ*. To this stirring solution, a yellow solution of 1.1 eq of $Co(C_5(CH_3)_5)_2$ (118 mg, 0.358 mmol) dissolved in 20 mL of cold THF at −40°C was added dropwise. The mixture was warmed to room temperature and the brownish-red solution turned yellow after addition of H_2. The solvent was removed, and the solids were extracted with THF followed by filtration through Celite. The crude product precipitated as a white powder after concentration of the THF filtrate (~3 mL) and addition of excess pentane. The powder was isolated by filtration through Celite before being redissolved in a minimal amount of THF. Off-white crystals were grown by successive recrystallizations from vapor diffusion of diethyl ether into THF (62 mg, 43% yield, first crop). ^{31}P{^{1}H} and ^{1}H NMR spectra match those previously published.

1.6 References

(1)   Cheon, J.; Yang, J. Y.; Koper, M.; Ishitani, O. From Pollutant to Chemical Feedstock: Valorizing Carbon Dioxide through Photo- and Electrochemical Processes. *Acc. Chem. Res.* **2022**, *55* (7), 931–932. https://doi.org/10.1021/acs.accounts.2c00129.

(2)   Francke, R.; Schille, B.; Roemelt, M. Homogeneously Catalyzed Electroreduction of Carbon Dioxide—Methods, Mechanisms, and Catalysts. *Chem. Rev.* **2018**, *118* (9), 4631–4701. https://doi.org/10.1021/acs.chemrev.7b00459.

(3)   Bai, S.-T.; Smet, G. D.; Liao, Y.; Sun, R.; Zhou, C.; Beller, M.; Maes, B. U. W.; Sels, B. F. Homogeneous and Heterogeneous Catalysts for Hydrogenation of CO2 to Methanol under Mild Conditions. *Chem. Soc. Rev.* **2021**, *50* (7), 4259–4298. https://doi.org/10.1039/D0CS01331E.

(4)   Bi, J.; Hou, P.; Liu, F.-W.; Kang, P. Electrocatalytic Reduction of CO2 to Methanol by Iron Tetradentate Phosphine Complex Through Amidation Strategy. *ChemSusChem* **2019**, *12* (10), 2195–2201. https://doi.org/10.1002/cssc.201802929.

(5)   Wang, F.; Cannon, A. T.; Bhattacharya, M.; Baumgarten, R.; VanderLinden, R. T.; Saouma, C. T. Hydrogenation and Electrocatalytic Reduction of Carbon Dioxide to Formate with a Single Co Catalyst. *Chem. Commun.* **2020**, *56* (81), 12142–12145. https://doi.org/10.1039/D0CC04310A.

(6)   Burgess, S. A.; Appel, A. M.; Linehan, J. C.; Wiedner, E. S. Changing the Mechanism for CO2 Hydrogenation Using Solvent-Dependent Thermodynamics. *Angew. Chem. Int. Ed.* **2017**, *56* (47), 15002–15005. https://doi.org/10.1002/anie.201709319.

(7)   Jeletic, M. S.; Mock, M. T.; Appel, A. M.; Linehan, J. C. A Cobalt-Based Catalyst for the Hydrogenation of CO2 under Ambient Conditions. *J. Am. Chem. Soc.* **2013**, *135* (31), 11533–11536. https://doi.org/10.1021/ja406601v.

(8)   Jeletic, M. S.; Helm, M. L.; Hulley, E. B.; Mock, M. T.; Appel, A. M.; Linehan, J. C. A Cobalt

Hydride Catalyst for the Hydrogenation of CO2: Pathways for Catalysis and Deactivation.

ACS Catal. **2014**, *4* (10), 3755–3762. https://doi.org/10.1021/cs5009927.

(9)   Mock, M. T.; Potter, R. G.; O'Hagan, M. J.; Camaioni, D. M.; Dougherty, W. G.; Kassel, W.

S.; DuBois, D. L. Synthesis and Hydride Transfer Reactions of Cobalt and Nickel Hydride

Complexes to BX3 Compounds. *Inorg. Chem.* **2011**, *50* (23), 11914–11928.

https://doi.org/10.1021/ic200857x.

(10)   García Basallote, M.; L. Hughes, D.; Jiménez-Tenorio, M.; Jeffery Leigh, G.;

Puerta Vizcaíno, M. C.; Valerga Jiménez, P. Chemistry of Cobalt Complexes with 1,2-Bis-

(Diethylphosphino)Ethane: Hydrides, Carbon Disulfide Complexes, and C–H Cleavage in

Activated Alk-1-Ynes. Crystal Structure of [CoH(C[Triple Bond, Length Half m-Dash]CCO

2 Et)(Et 2 PCH 2 CH 2 PEt 2) 2][BPh 4]. *J. Chem. Soc. Dalton Trans.* **1993**, *0* (12), 1841–

1847. https://doi.org/10.1039/DT9930001841.

(11)   Jewiss, H. C.; Levason, W.; Webster, M. Coordination Chemistry of Higher Oxidation

States. 20. Synthesis and Cobalt-59 NMR Studies of Tris(Diphosphine)Cobalt(3+),

Tris(Diarsine)Cobalt(3+) and Related Complexes. Crystal Structure of Tris[o-

Phenylenebis(Dimethylarsine)]Cobalt(III) Tetrafluoroborate-2-Water. *Inorg. Chem.* **1986**,

25 (12), 1997–2001. https://doi.org/10.1021/ic00232a019.

(12)   Jessop, P. G.; Joó, F.; Tai, C.-C. Recent Advances in the Homogeneous Hydrogenation of

Carbon Dioxide. *Coord. Chem. Rev.* **2004**, *248* (21), 2425–2442.

https://doi.org/10.1016/j.ccr.2004.05.019.

(13)   Taheri, A.; Thompson, E. J.; Fettinger, J. C.; Berben, L. A. An Iron Electrocatalyst for

Selective Reduction of CO_2 to Formate in Water: Including Thermochemical Insights. *ACS

Catal.* **2015**, *5* (12), 7140–7151. https://doi.org/10.1021/acscatal.5b01708.

(14) Kang, P.; J. Meyer, T.; Brookhart, M. Selective Electrocatalytic Reduction of Carbon Dioxide to Formate by a Water-Soluble Iridium Pincer Catalyst. *Chem. Sci.* **2013**, *4* (9), 3497–3502. https://doi.org/10.1039/C3SC51339D.

(15) Waldie, K. M.; Flajslik, K. R.; McLoughlin, E.; Chidsey, C. E. D.; Waymouth, R. M. Electrocatalytic Alcohol Oxidation with Ruthenium Transfer Hydrogenation Catalysts. *J. Am. Chem. Soc.* **2017**, *139* (2), 738–748. https://doi.org/10.1021/jacs.6b09705.

(16) Cunningham, D. W.; Barlow, J. M.; Velazquez, R. S.; Yang, J. Y. Reversible and Selective CO_2 to HCO_2- Electrocatalysis near the Thermodynamic Potential. *Angew. Chem. Int. Ed.* **2020**, *59* (11), 4443–4447. https://doi.org/10.1002/anie.201913198.

(17) Bard, A., J.; Faulkner, L. R. *Electrochemical Methods: Fundamentals and Applications*, 2nd ed.; John Wiley & Sons, Inc., 2001.

(18) Ceballos, B. M.; Yang, J. Y. Directing the Reactivity of Metal Hydrides for Selective CO_2 Reduction. *Proc. Natl. Acad. Sci.* **2018**, *115* (50), 12686–12691. https://doi.org/10.1073/pnas.1811396115.

(19) Wiedner, E. S.; Chambers, M. B.; Pitman, C. L.; Bullock, R. M.; Miller, A. J. M.; Appel, A. M. Thermodynamic Hydricity of Transition Metal Hydrides. *Chem. Rev.* **2016**, *116* (15), 8655–8692. https://doi.org/10.1021/acs.chemrev.6b00168.

(20) Tsay, C.; Livesay, B. N.; Ruelas, S.; Yang, J. Y. Solvation Effects on Transition Metal Hydricity. *J. Am. Chem. Soc.* **2015**, *137* (44), 14114–14121. https://doi.org/10.1021/jacs.5b07777.

(21) Ceballos, B. M.; Tsay, C.; Yang, J. Y. CO_2 Reduction or HCO_2- Oxidation? Solvent-Dependent Thermochemistry of a Nickel Hydride Complex. *Chem. Commun.* **2017**, *53* (53), 7405–7408. https://doi.org/10.1039/C7CC02511D.

(22) Pitman, C. L.; Brereton, K. R.; Miller, A. J. M. Aqueous Hydricity of Late Metal Catalysts as a Continuum Tuned by Ligands and the Medium. *J. Am. Chem. Soc.* **2016**, *138* (7), 2252–2260. https://doi.org/10.1021/jacs.5b12363.

(23) Mathis, C. L.; Geary, J.; Ardon, Y.; Reese, M. S.; Philliber, M. A.; VanderLinden, R. T.; Saouma, C. T. Thermodynamic Analysis of Metal–Ligand Cooperativity of PNP Ru Complexes: Implications for CO2 Hydrogenation to Methanol and Catalyst Inhibition. *J. Am. Chem. Soc.* **2019**. https://doi.org/10.1021/jacs.9b06760.

(24) Brereton, K. R.; Jadrich, C. N.; Stratakes, B. M.; Miller, A. J. M. Thermodynamic Hydricity across Solvents: Subtle Electronic Effects and Striking Ligation Effects in Iridium Hydrides. *Organometallics* **2019**, *38* (16), 3104–3110. https://doi.org/10.1021/acs.organomet.9b00278.

(25) Federsel, C.; Jackstell, R.; Boddien, A.; Laurenczy, G.; Beller, M. Ruthenium-Catalyzed Hydrogenation of Bicarbonate in Water. *ChemSusChem* **2010**, *3* (9), 1048–1050. https://doi.org/10.1002/cssc.201000151.

(26) Burgess, S. A.; Kendall, A. J.; Tyler, D. R.; Linehan, J. C.; Appel, A. M. Hydrogenation of CO_2 in Water Using a Bis(Diphosphine) Ni–H Complex. *ACS Catal.* **2017**, *7* (4), 3089–3096. https://doi.org/10.1021/acscatal.7b00350.

(27) J. Connelly, S.; S. Wiedner, E.; M. Appel, A. Predicting the Reactivity of Hydride Donors in Water: Thermodynamic Constants for Hydrogen. *Dalton Trans.* **2015**, *44* (13), 5933–5938. https://doi.org/10.1039/C4DT03841J.

(28) Wiedner, E. S.; Linehan, J. C. Making a Splash in Homogeneous CO2 Hydrogenation: Elucidating the Impact of Solvent on Catalytic Mechanisms. *Chem. – Eur. J.* **2018**, *24* (64), 16964–16971. https://doi.org/10.1002/chem.201801759.

(29) Barlow, J. M.; Yang, J. Y. Thermodynamic Considerations for Optimizing Selective CO2 Reduction by Molecular Catalysts. *ACS Cent. Sci.* **2019**, *5* (4), 580–588. https://doi.org/10.1021/acscentsci.9b00095.

(30) Johnson, S. I.; Nielsen, R. J.; Goddard, W. A. Selectivity for HCO_2^- over H_2 in the Electrochemical Catalytic Reduction of CO_2 by $(POCOP)IrH_2$. *ACS Catal.* **2016**, *6* (10), 6362–6371. https://doi.org/10.1021/acscatal.6b01755.

(31) Taheri, A.; Carr, C. R.; Berben, L. A. Electrochemical Methods for Assessing Kinetic Factors in the Reduction of CO_2 to Formate: Implications for Improving Electrocatalyst Design. *ACS Catal.* **2018**, *8* (7), 5787–5793. https://doi.org/10.1021/acscatal.8b01799.

(32) Barlow, J. M.; Ziller, J. W.; Yang, J. Y. Inhibiting the Hydrogen Evolution Reaction (HER) with Proximal Cations: A Strategy for Promoting Selective Electrocatalytic Reduction. *ACS Catal.* **2021**, *11* (13), 8155–8164. https://doi.org/10.1021/acscatal.1c01527.

Chapter 2: Electrocatalytic Reduction of N_2O and Mechanistic Insights Using a Platinum CO_2 Reduction Electrocatalyst

2.1 Introduction

Atmospheric concentrations of nitrous oxide (N_2O) have continually increased since the beginning of the 19th century and much of this increase can be attributed to agricultural and industrial processes.[1,2] While the absolute concentrations of N_2O are low compared to other greenhouse gases, it is nearly 300 times more potent than carbon dioxide (CO_2) and is currently the largest contributor to ozone destruction.[3] Nitrous oxide is isoelectronic to CO_2 and is a thermodynamically a potent oxidant, but kinetically inert.[4,5] Although N_2O is a poor ligand to transition metals,[6] some transition metal hydrogenation catalysts for N_2O reduction have been reported.[7-9] Work by Kaplan and Bergman also demonstrated the stoichiometric reactivity of ruthenium dihydrides and N_2O to generate N_2 and ruthenium hydroxide complexes.[10,11] While there have been many advances in homogeneous electrocatalytic CO_2 reduction over the last 30 years, there has been comparatively little work done on homogeneous electrocatalytic N_2O reduction. Previous work on homogeneous electrocatalytic reduction of N_2O to N_2 has focused on electrocatalysts that reduce CO_2 to CO.[12-14] In contrast, $[Pt(dmpe)_2]^{2+}$ (dmpe = 1,2-*bis*(dimethylphosphino)ethane) has been previously reported by our group as a selective electrocatalyst for CO_2 reduction to formate which proceeds through a platinum hydride $[Pt(dmpe)_2H]^+$ using phenol as the acid source.[15,16] For this study, $[Pt(dmpe)_2]^{2+}$ was investigated for electrocatalytic N_2O reduction to elucidate whether other CO_2 reduction catalysts that operate through hydride transfer may be viable candidates for N_2O reduction. Our proposed electrocatalytic cycle (**Scheme 2.1**) includes electrolytic generation of the $[Pt(dmpe)_2H]^+$, followed by reactivity with N_2O to produce N_2 and hydroxide (OH^-).

Scheme 2.1. Proposed electrocatalytic cycle for N_2O reduction using $[Pt(dmpe)_2]^{2+}$.
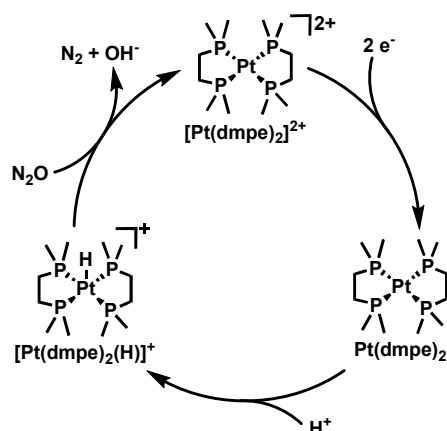
2.2 Results

2.2.1 Electrochemical studies using cyclic voltammetry

Cyclic voltammograms of $[Pt(dmpe)_2]^{2+}$ in MeCN feature a quasi-reversible two-electron reduction event at $-$ 1.73 V vs. $Fe(C_5H_5)_2^{+/0}$.[16] Under 1 atm of N_2O with no added phenol, the $Pt^{2+/0}$ feature becomes irreversible, but the return oxidation is observed at scan rates > 500 mV/s (**Figure 2.1**), suggesting that $[Pt(dmpe)_2]^0$ reacts with N_2O at a modest rate in the absence of acid. In the presence of N_2O and phenol, a loss of reversibility is observed at scan rates up to 10 V/s. The protonation rate of the Pt(0) by phenol to form the hydride was previously measured by Ceballos *et al.* to be >10^5 s^{-1}.[16]
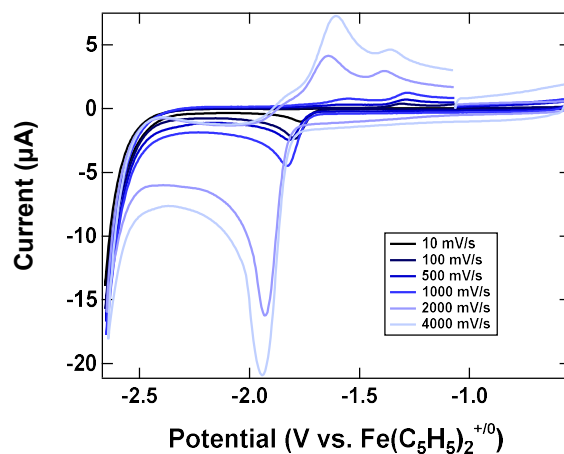
Figure 2.1. Cyclic voltammograms of 1 mM $[Pt(dmpe)_2][PF_6]_2$ in 0.2 M TBAPF$_6$ MeCN under 1 atm of N_2O at different scan rates.

Additionally, in the presence of N₂O and phenol, the oxidation event at -0.37 V vs. $Fe(C_5H_5)_2^{+/0}$ attributed to the oxidation of $[Pt(dmpe)_2H]^+$ is apparent at 25 mV/s and does not significantly increase between CVs acquired at 1 V/s and 10 V/s (**Figure 2.2**). The appearance of the oxidation feature of the platinum hydride suggests that protonation of $[Pt(dmpe)_2]^0$ to form the hydride is likely fast, in agreement with the previously measured rate. In contrast, subsequent reactivity between $[Pt(dmpe)_2H]^+$ and N₂O is slow since the hydride is still observed at slow scan rates.
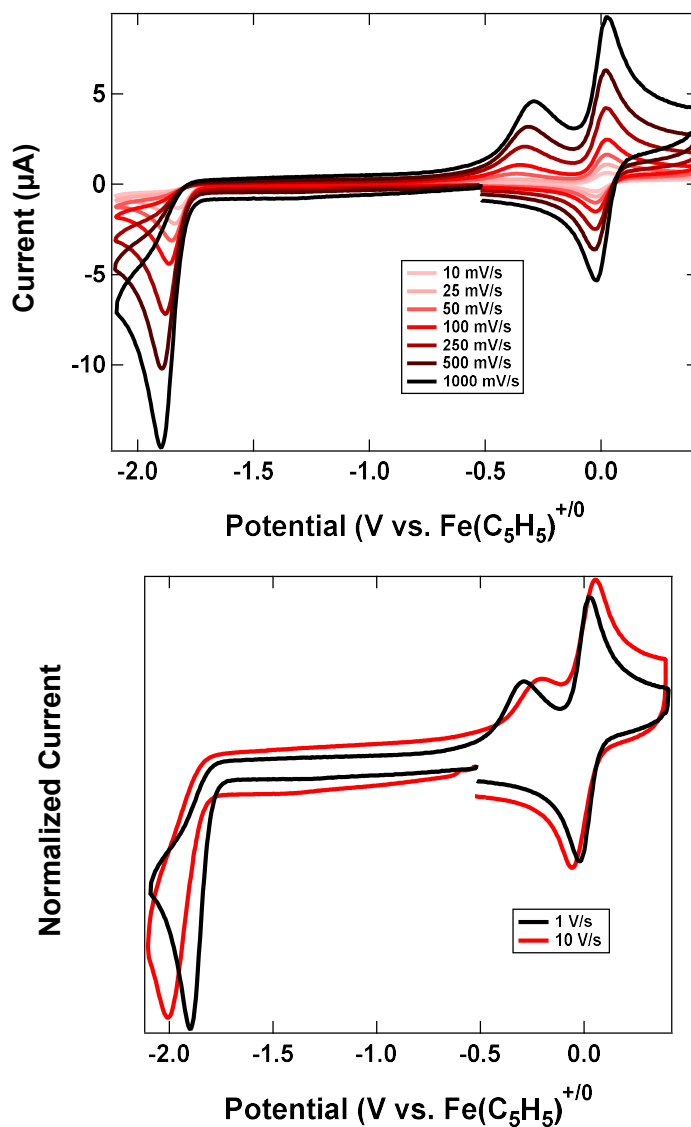
Figure 2.2. Cyclic voltammograms of 1 mM $[Pt(dmpe)_2][PF_6]_2$ with 1 equivalent of phenol in 0.2 M TBAPF₆ MeCN under 1 atm of N₂O. *Top*: CVs at different scan rates. *Bottom*: CVs at 1 V/s and 10 V/s showing normalized current.

A modest current enhancement consistent with electrocatalysis is observed for the irreversible $Pt^{2+/0}$ reduction event under N_2O with increasing titrations of phenol at very slow scan rates, but no significant current enhancement is observed after the first 10 equivalents of acid were added.
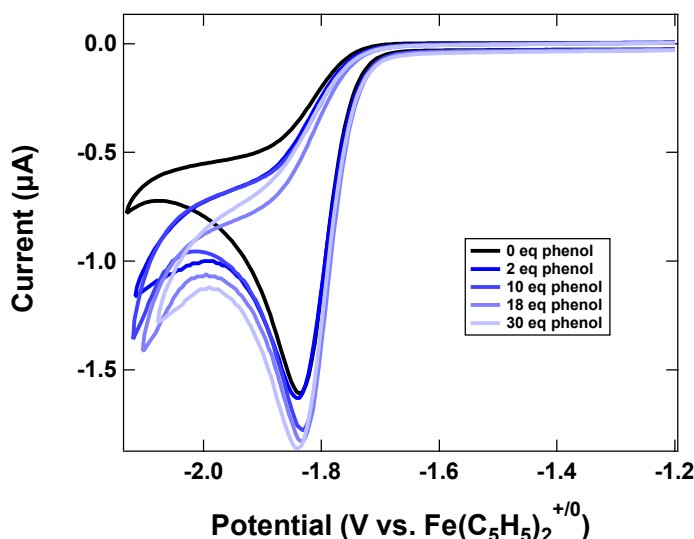
Figure 2.3. Cyclic voltammograms of 1 mM $[Pt(dmpe)_2][PF_6]_2$ with increasing amounts of phenol in 0.2 M TBAPF$_6$ MeCN under 1 atm of N_2O at 10 mV/s.

2.2.2 Controlled potential electrolysis

Table 2.1. **Summary of CPE data for N_2O reduction using $[Pt(dmpe)_2]^{2+}$.**[a]

	Charge (C)	Faradaic efficiency (% N_2)	mmol (N_2)	Faradaic efficiency (% H_2)	mmol (H_2)
$[Pt(dmpe)_2]^{2+}$	5.0 ± 1.5	60 ± 10	0.015 ± 0.003	9 ± 4	0.0022 ± 0.0008
No cat.	1.2	34	0.002	10	0.0006

[a]Experiments were conducted with 2 mM of analyte (0.01 mmol) using a carbon fabric working electrode, a carbon fabric counter electrode, and a Ag$^{+/0}$ pseudo-reference electrode separated from the bulk solution with a Vycor tip. Solutions were electrolyzed at −1.92 V vs. Fe(C$_5$H$_5$)$_2^{+/0}$ for 1h over a mercury pool in the working electrode compartment.

Three controlled potential electrolysis experiments for N_2O reduction were performed using $[Pt(dmpe)_2]^{2+}$ and excess phenol in MeCN at -1.92 V vs. $Fe(C_5H_5)_2^{+/0}$. The accumulated charge versus time with and without catalyst are shown in **Figure 2.4**. Data from these experiments are summarized in **Table 2.1**.
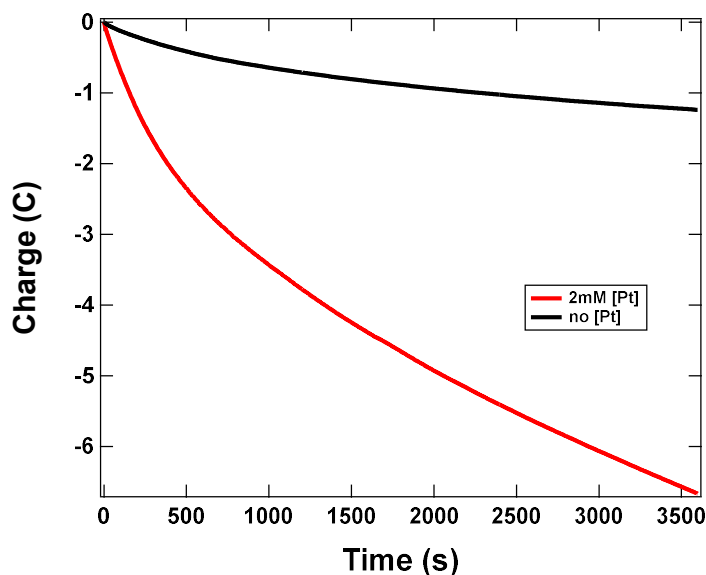
Figure 2.4. Traces of charge over time for controlled potential electrolysis with 2 mM $[Pt(dmpe)_2]^{2+}$ (**red**) and without $[Pt(dmpe)_2]^{2+}$ (**black**).

The 60% faradaic efficiency for N_2 was significantly higher than the 9% observed for H_2. An average of 5.0(±1.5) C was passed, corresponding to 2.6(±0.7) eq of electrons relative to $[Pt(dmpe)_2]^{2+}$. In the presence of $[Pt(dmpe)_2]^{2+}$ (0.01 mmol) as a catalyst, 1.5(±0.3) eq of N_2 corresponding to 0.015(±0.003) mmol were produced. A blank electrolysis with no catalyst present produced <15% of the N_2 and ~ 30% of the H_2 observed with catalyst present. $^{31}P(^1H)$ NMR spectra of the solutions before and after electrolysis show $[Pt(dmpe)_2][PF_6]_2$ with no evidence of catalyst or ligand decomposition. No precipitate was observed in the post-electrolysis solution.
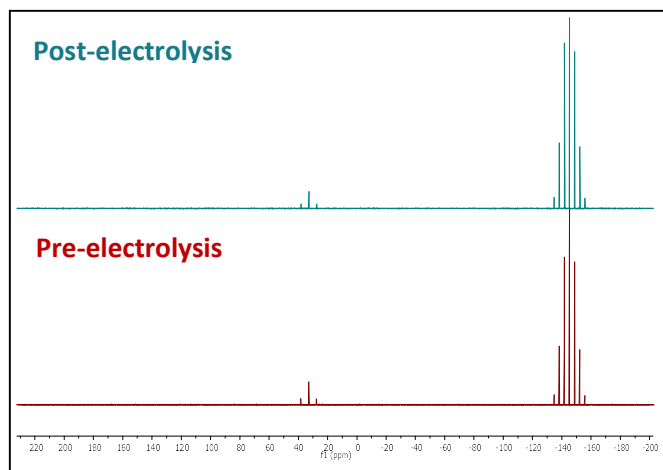
Figure 2.5. $^{31}P\{^1H\}$ NMR spectra of pre-electrolysis (*bottom*) and post-electrolysis solutions (*top*) showing [Pt(dmpe)$_2$]$^{2+}$ and PF$_6^-$ with no other species formed. Spectra were acquired using MeCN.

2.2.3 Stoichiometric reactivity

In order to identify the relevant species which reacts with N$_2$O, all three platinum species which may be catalytically relevant were individually exposed to N$_2$O and monitored by NMR.

[Pt(dmpe)$_2$][PF$_6$]$_2$ does not react with N$_2$O on the NMR timescale. A sample of [Pt(dmpe)$_2$][PF$_6$]$_2$ in CD$_3$CN was exposed to 1 atm of N$_2$O in a J-young. No change in the $^{31}P\{^1H\}$ NMR spectra was observed after 3 days (**Figure 2.6**).

+ N₂O 3 days

+ N₂O 20 minutes

[Pt(dmpe)₂][PF₆]₂

220 200 180 160 140 120 100 80 60 40 20 0 -20 -40 -60 -80 -100 -120 -140 -160 -180
f1 (ppm)
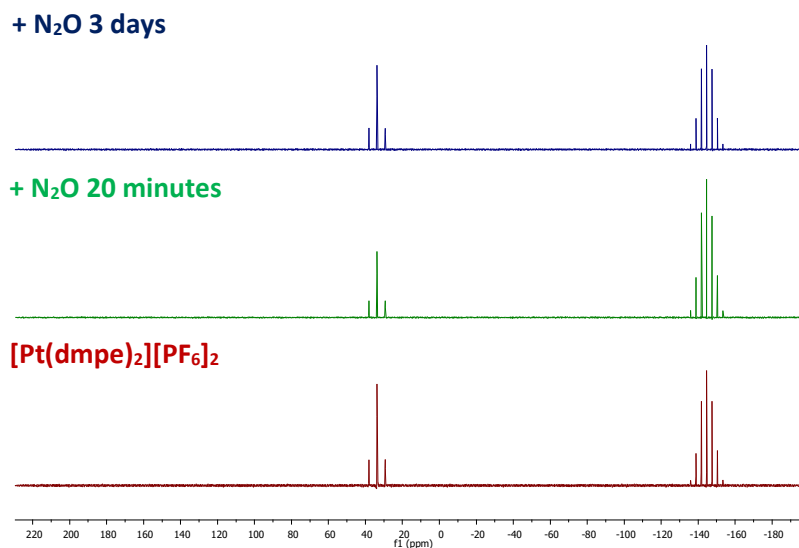
Figure 2.6. $^{31}P\{^1H\}$ NMR spectra of [Pt(dmpe)$_2$][PF$_6$]$_2$ (**bottom**), after N$_2$O addition (**middle**), and after 3 days of exposure to N$_2$O (**top**) in CD$_3$CN.

       In contrast, exposing samples of [Pt(dmpe)$_2$] or [Pt(dmpe)$_2$H]$^+$ to 1 atm of N$_2$O under the

same conditions resulted in rapid consumption of the starting material within 30 minutes.

[Pt(dmpe)$_2$] is a clear colorless solution in d_8-toluene but the solution rapidly becomes a light

brown which diffuses through the solution after exposure to N$_2$O. The $^{31}P\{^1H\}$ NMR spectrum

features a major species at δ = 30.0 ppm which does not exhibit ^{195}Pt-^{31}P coupling, suggesting

that the species arises from ligand decomposition that is no longer bound to the metal (**Figure**

2.7, middle). Adding phenol to the mixture shifts the signal to δ = 43.9 ppm which also shows

no ^{195}Pt-^{31}P coupling (**Figure 2.7**, top). No starting material is observed. Attempts to isolate and

further characterize these complexes by X-ray crystallography were unsuccessful.
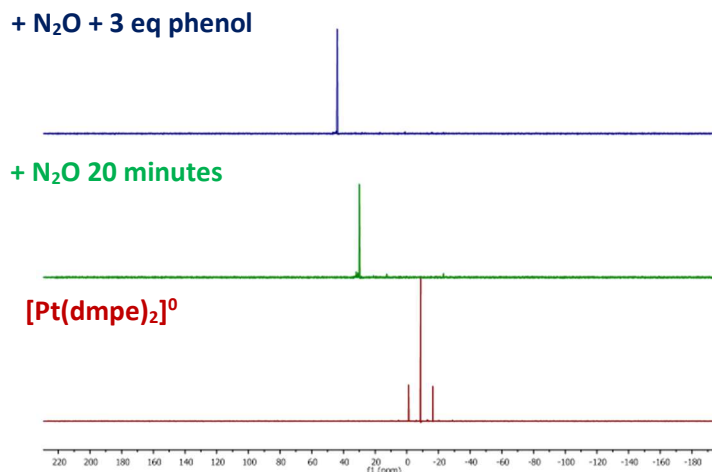
Figure 2.7. ^{31}P{^{1}H} NMR spectra of [Pt(dmpe)$_2$]^0 (**bottom**), after N$_2$O addition (**middle**), and after N$_2$O addition followed by phenol addition (**top**) in d_8-toluene.

[Pt(dmpe)$_2$H]$^+$ is a clear yellow-brown solution in CD$_3$CN and the solution becomes bright yellow when the sample is exposed to 1 atm N$_2$O. White precipitate is observed. The ^{31}P{^{1}H} NMR spectrum shows a number of features with a prominent species centered at δ = 34.8 ppm (s, $^1J_{Pt-P}$ = 2180 Hz) which is proposed to be [Pt(dmpe)$_2$OH]$^+$. The reaction does not proceed cleanly since multiple species are observed by ^{31}P{^{1}H} NMR spectroscopy; however, complete consumption of the [Pt(dmpe)$_2$H]$^+$ is observed. The ^{31}P{^{1}H} NMR spectrum of this new species formed from N$_2$O exposure differs from that of [Pt(dmpe)$_2$][PF$_6$]$_2$ slightly; the signal is shifted upfield by 0.2 ppm and the $^1J_{Pt-P}$ constant is different by 10 Hz (**Figure 2.8**).
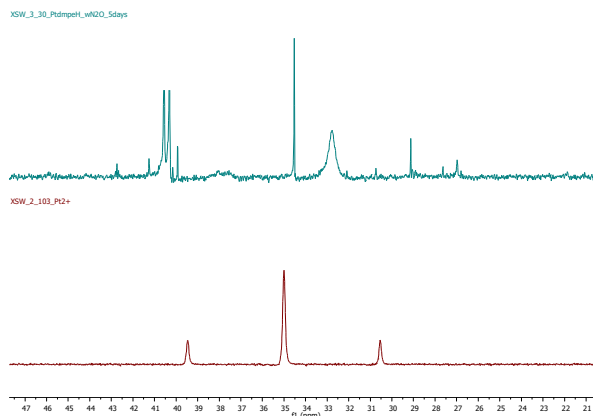
Figure 2.8. ^{31}P{^{1}H} NMR spectra of [Pt(dmpe)$_2$][PF$_6$]$_2$ (*bottom*) and the reaction mixture produced from adding N$_2$O to [Pt(dmpe)$_2$H][PF$_6$] in CD$_3$CN.

51

2.2.4 Identification of intermediate formed from reaction of $[Pt(dmpe)_2H]^+$ with N2O

The species formed after exposure of $[Pt(dmpe)_2H]^+$ to 1 atm of N_2O is postulated to be

$[Pt(dmpe)_2OH]^+$. The $^{31}P\{^1H\}$ NMR spectrum is dominated by a species with δ = 34.8 ppm (s,

$^1J_{Pt-P}$ = 2180 Hz) while there is a feature observed in the ^1H spectrum at δ = -5.64 ppm with

apparent ^{31}P-^1H coupling (J = 74 Hz) (**Figure 2.9**). A smaller feature is also observed at δ = -

3.74 ppm but this species is much smaller than the one at δ = -5.64 ppm. No platinum hydride

starting material is observed. By mass spectrometry, a species with 512.1 m/z is observed which

corresponds to the molecular weight of $[Pt(dmpe)_2H]^+$ + ^{16}O. The IR spectrum of the drop cast

reaction mixture of $[Pt(dmpe)_2H]^+$ with N_2O displays weak, broad features at 3461 cm^{-1}, 3275

cm^{-1}, and 3187 cm^{-1} in the expected region for O-H vibrations (**Figure 2.10**). Attempts to isolate

and characterize the major product from the reaction have been unsuccessful.
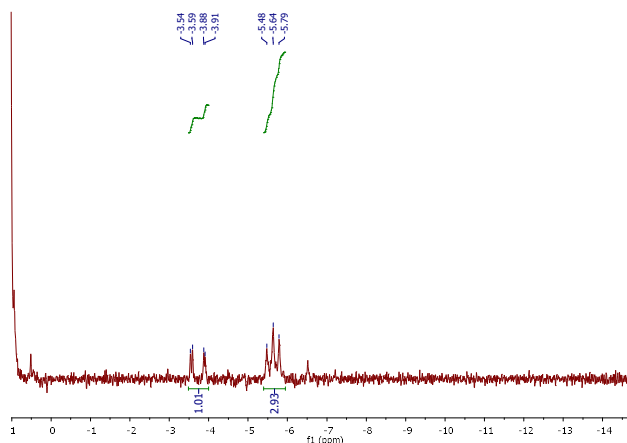
Figure 2.9. ^1H NMR spectrum of the reaction mixture of $[Pt(dmpe)_2H]^+$ and N_2O showing the broad feature at δ = -5.64 ppm, a smaller feature at δ = -3.74 ppm and no remaining $[Pt(dmpe)_2H]^+$ at δ = -11.55 ppm.

When a sample of $[Pt(dmpe)_2D]^+$ is exposed to 1 atm of N_2O overnight, a species with

513.1 m/z is detected by mass spectrometry, which corresponds to the molecular weight of

$[Pt(dmpe)_2D]^+$ + ^{16}O. The IR spectrum of the reaction mixture of $[Pt(dmpe)_2D]^+$ with N_2O

contains a broad feature at 3254 cm^{-1} in the O-H region (**Figure 2.10**). The O-D vibration is

expected to occur between 2700-2300 cm^{-1} but no new feature is observed here, possibly due to insufficient material deposited during the drop casting process.
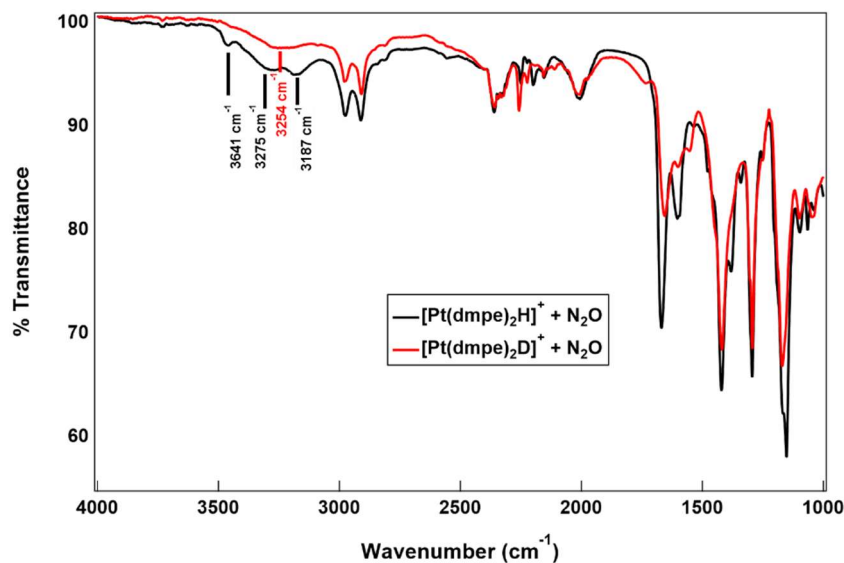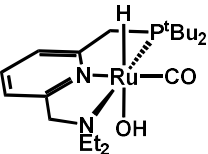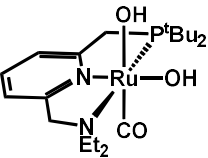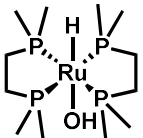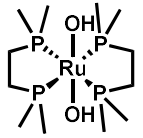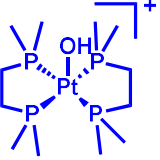
Figure 2.10. FT-IR spectra of the reaction mixtures of [Pt(dmpe)$_2$H]$^+$ + N$_2$O (**black**) and [Pt(dmpe)$_2$D]$^+$ + N$_2$O (**red**). Samples were drop cast from MeCN for [Pt(dmpe)$_2$H]$^+$ or CD3CN for [Pt(dmpe)$_2$D]$^+$.

The IR and NMR spectroscopy data as well as mass spectrometry suggest that [Pt(dmpe)$_2$OH]$^+$ is formed from the reaction of [Pt(dmpe)$_2$H]$^+$ with N$_2$O. As mentioned in the introduction to this chapter, O-atom insertion into M-H bonds using N$_2$O is precedented with Ru(dmpe)$_2$(H)$_2$ to form Ru(dmpe)$_2$(OH)H when only 1 equivalent of N$_2$O is added or Ru(dmpe)$_2$(OH)$_2$ under 1 atm of N$_2$O.[10] This metal hydride reactivity with N$_2$O has also been reported using Ru(PNN)(CO)(OH)H pincer complexes to form Ru(PNN)(CO)(OH)$_2$.[17] The ^{1}H signal for the hydroxide ligands in these Ru(PNN) pincer systems has been reported as broad features at -1.41 ppm (Ru-OH d_8-toluene), -7.4 (Ru-(OH)$_2$, CD$_2$Cl$_2$) while broad hydroxyl resonances are observed at -7.00 ppm (Ru-(OH)$_2$, C$_6$D$_6$) and -5.41 ppm (Ru-OH) for Ru(dmpe)$_2$X$_2$ compounds.[10,17,18] These values are in agreement with the resonance observed at -5.64 ppm that is tentatively assigned to the O*H* moiety of [Pt(dmpe)$_2$OH]$^+$ and are summarized in **Table 2.2**.

Table 2.2 Summary of ¹H NMR and IR spectroscopy data for known and proposed M-OH compounds.

	¹H NMR for O*H* (ppm)	IR $\tilde{v}_{OH}$ (cm⁻¹)
Ru(PNN)(OH)H	δ = -1.41 (br, O*H*) d_8-toluene	3413 (br) thin film, NaCl
Ru(PNN)(OH)₂	δ = -7.4 (br, 2 O*H*) CD₂Cl₂	--
trans-Ru(dmpe)₂(OH)H	δ = -5.41 (br, O*H*) C₆D₆	3613 (w) C₆D₆
trans-Ru(dmpe)₂(OH)₂	δ = -7.00 (br, 2 O*H*) C₆D₆	3400-3100 (br) Nujol
proposed [Pt(dmpe)₂OH]⁺	δ = -5.64 (br, O*H*) CD₃CN	3641 (w, br) or 3300-3100 (w, br)

2.2.5 Kinetic analysis

Since cyclic voltammograms and NMR spectra both show that the reduced species, [Pt(dmpe)₂]⁰, reacts with N₂O in the absence of acid, rate constants for both reactions were determined to elucidate whether protonation or N₂O reactivity was dominant during catalysis.

As described previously, cyclic voltammograms of [Pt(dmpe)₂]²⁺ exhibit a quasi-reversible feature at -1.73 V vs. Fe(C₅H₅)₂⁺/⁰ which corresponds to the Pt²⁺/⁰ couple; the reduction is irreversible at slow scan rates once N₂O is added to the solution. The return oxidation is observed at faster scan rates (>500 mV/s) suggesting that the subsequent chemical

step after reduction is relatively slow. The k_{obs} for this reaction was determined to be 1.7($\pm$0.7) s^{-1} by fitting the data to a working curve of i_{pa}/i_{pc} vs. log(kt) where k is the rate constant and t is the time in seconds for scanning from $E_{1/2}$ to the turning potential (**Figure 2.11**).[19,20]
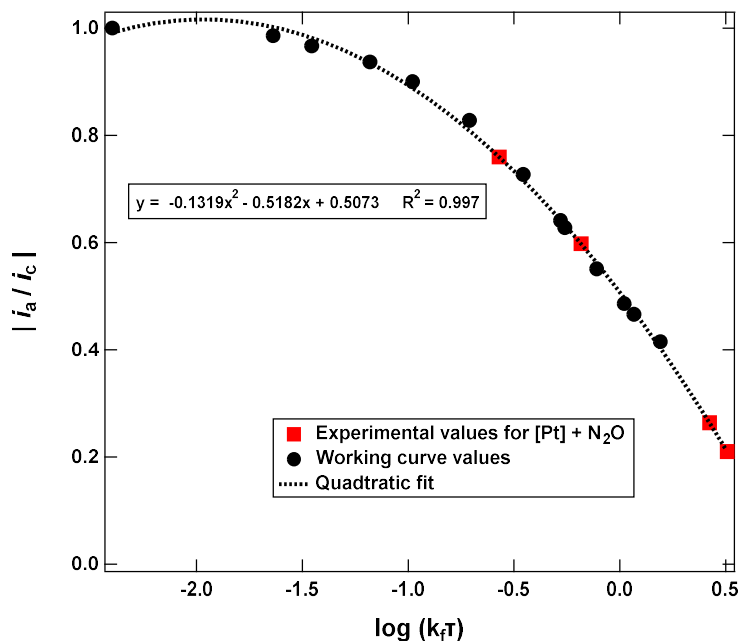
Figure 2.11. Working curve used to calculate k_{obs} for [Pt(dmpe)$_2$]^0 reacting with N$_2$O. Values in black are from ref. 19. Experimental values are in red.

In comparison, the k_{obs} for the protonation of [Pt(dmpe)$_2$] with phenol to form [Pt(dmpe)$_2$H]$^+$ was previously determined to be >10^5 s^{-1} since the Pt$^{2+/0}$ redox event remains irreversible even at scan rates of 125 V/s.[16] The immense difference between these two k_{obs} values indicates that under electrochemical conditions, protonation of [Pt(dmpe)$_2$] to form the hydride will be significantly faster than coordination or reactivity of [Pt(dmpe)$_2$] with N$_2$O directly. As a result, it is likely that catalysis proceeds through protonation of [Pt(dmpe)$_2$] to form [Pt(dmpe)$_2$H]$^+$ which subsequently reacts with N$_2$O rather than N$_2$O interaction with the Pt^0 species and subsequent protonation.

Current enhancement is observed for the irreversible Pt$^{2+/0}$ reduction event under N$_2$O with increasing titrations of phenol but no significant current enhancement is observed after the

first 10 equivalents of acid added (**Figure 2.3**). An S-shaped catalytic current in the pure kinetic region is not observed, preventing accurate determination of a value for k_{cat} for N_2O reduction. Based on the minimal increase in current observed for N_2O reduction, the k_{cat} for this reaction is likely lower than the k_{cat} determined for $[Pt(dmpe)_2H]^+$ with CO_2 (0.5 s^{-1}).[16]

As previously described, independently synthesized $[Pt(dmpe)_2H]^+$ is completely consumed within 30 minutes under 1 atm of N_2O, but the reaction does not proceed cleanly and precipitate is observed. Although the reaction is not clean, the estimated k_{obs} of initial N_2O reactivity to be 1.3($\pm$0.4) x 10^{-4} s^{-1} assuming a pseudo-first order reaction based on the disappearance of $[Pt(dmpe)_2H]^+$. This value was obtained by plotting the concentration of $[Pt(dmpe)_2H]^+$ over the initial time points (< 11 minutes) (**Figure 2.12**). The slopes of these data represent the rate equation:

$$-\frac{d[PtH^+]}{dt} = -(\text{slope}) = k[PtH^+][N_2O] \qquad \text{(eq. 2.1)}$$

Under experimental conditions, the concentration of N_2O is presumed to be much higher than the concentration of $[Pt(dmpe)_2H]^+$. While a precise value for the solubility of N_2O in acetonitrile has not been measured, the solubility is generally comparable to that of CO_2 in many organic solvents. The solubility of CO_2 in MeCN is 280 mM.[21,22] N_2O solubility has been measured to be as high as 620 mM in THF.[9] The rate expression thus simplifies to:

$$-\frac{d[PtH^+]}{dt} = -(\text{slope}) = k_{obs}[PtH^+] \qquad \text{(eq. 2.2)}$$

The initial rate constant, k_{obs}, can be calculated using the slope of the linear fit and the known concentration of $[Pt(dmpe)_2H]^+$ used.

$$k_{obs} = \frac{-(\text{slope})}{[PtH^+]} \qquad \text{(eq. 2.3)}$$
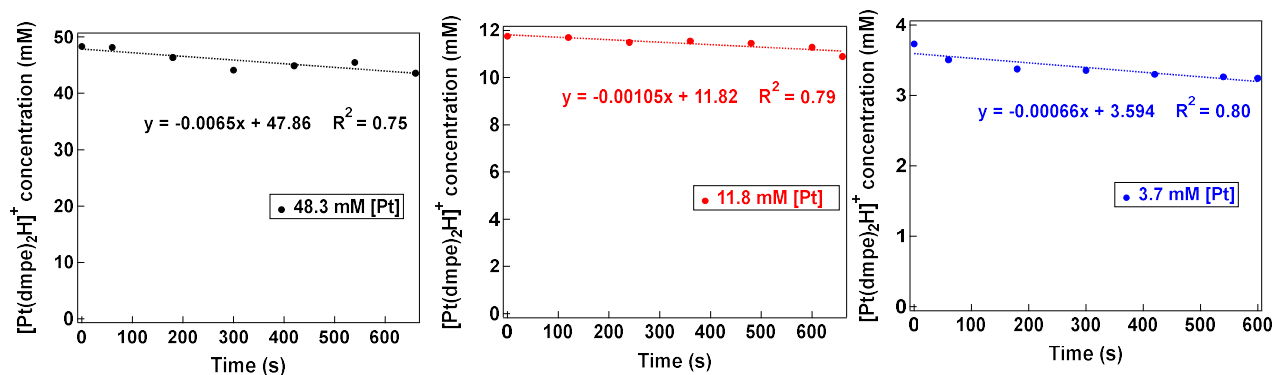
Figure 2.12. Reactions of $[Pt(dmpe)_2H]^+$ with N_2O with different starting amounts of $[Pt(dmpe)_2H]^+$. The dotted lines represent the best linear fit for time points < 11 minutes.

Based on the consumption of the hydride species observed by ^1H NMR and assuming a pseudo-first order reaction due to the high solubility of N_2O, the k_{obs} of N_2O reactivity is estimated to be $1.3(\pm 0.4) \times 10^{-4}$ s^{-1} which is comparable to the k_{obs} determined for $[Pt(depe)_2H]^+$ (depe = 1,2-*bis*(diethylphosphino)ethane) with CO_2 (2.8×10^{-4} s^{-1}). This is in agreement with the very modest current enhancement upon acid titration and absence of an S-shaped catalytic current even at low scan rates, indicating that the k_{cat} for N_2O reduction using $[Pt(dmpe)_2H]^+$ is likely much lower than the k_{cat} determined for $[Pt(dmpe)_2H]^+$ with CO_2 (0.5 s^{-1}). Notably, the decomposition observed during stoichiometric reactivity using $[Pt(dmpe)_2H]^+$ and N_2O is not observed during electrocatalysis, suggesting that this chemical step described by this rate may not be catalytically relevant.

2.3 Discussion

$[Pt(dmpe)_2]^{2+}$ is a competent electrocatalyst for N_2O reduction to N_2, and based on the stoichiometric reactivity and kinetic analysis, a catalytic cycle (**Scheme 2.2**) is proposed that notably features a $[Pt(dmpe)_2H]^+$ intermediate. An off-cycle pathway (dotted line, **Scheme 2.2**) with N_2O reacting directly with $[Pt(dmpe)_2]^0$ is not relevant under catalytic conditions since protonation to form the metal hydride is significantly faster. The kinetic values for electron

transfer and protonation were previously determined from investigations using $[Pt(dmpe)_2]^{2+}$ for CO_2 reduction.[16]

When $[Pt(dmpe)_2]^{2+}$ catalyzes CO_2 reduction using phenol, CO_2 insertion into the Pt-H bond is proposed to be the rate-determining step with a $k_{obs} < 0.5$ s^{-1}.[16] It is postulated that likewise, N_2O insertion into the Pt-H bond may be rate-determining in catalysis since an initial k_{obs} of 1.3($\pm$0.4) x 10^{-4} s^{-1} is estimated for this reaction. It is noted, however, that in both CO_2 and N_2O reduction the post-electrolysis solution contains only $[Pt(dmpe)_2][PF_6]_2$ in the $^{31}P\{^1H\}$ NMR spectrum because it is the resting of the catalytic cycle.

Scheme 2.2. Proposed electrocatalytic cycle for N_2O reduction using $[Pt(dmpe)_2]^{2+}$ with rates for each step shown in red.
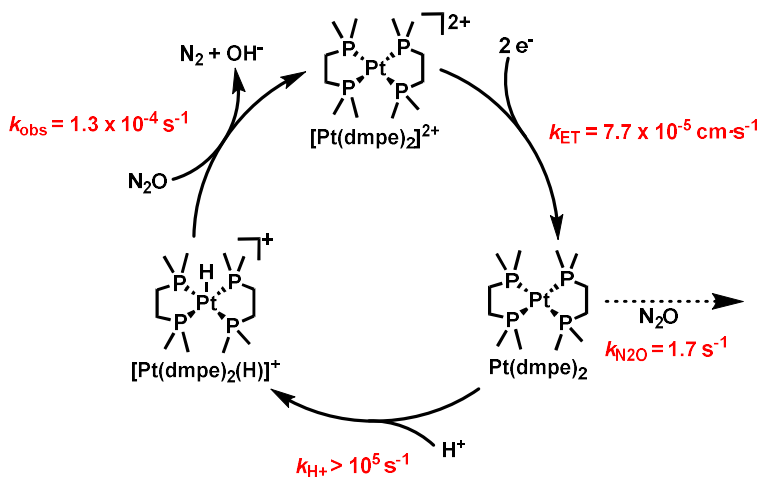
In contrast to other electrocatalysts for N_2O reduction,[12–14] the mechanism proposed proceeds through a M-H. It is further suggested that $[Pt(dmpe)_2OH]^+$ is a catalytically relevant intermediate formed from the reaction of N_2O with the metal hydride. N_2O is known to perform O-atom insertion into M-H bonds, as Kaplan and Bergman demonstrated with $Ru(dmpe)_2(H)_2$ to form $Ru(dmpe)_2(OH)_2$.[10,11,24] Formation of metal hydroxo compounds is notably also the proposed mechanism for catalytic N_2O hydrogenation using Ru and Ir pincer complexes which react via a M-H intermediate, as well as the bimetallic system developed by Jurt *et al.*[7–9,25] In contrast, the $Re(bpy)(CO)_3Cl$ and $Mn(bpy)(CO)_3Br$ systems which Chardon-Noblet, Costentin,

and coworkers have investigated for electrocatalytic N_2O reduction are postulated to undergo direct reactivity between the reduced metal species and N_2O, followed by protonation.[12] Similarly, Co porphyrins systems which are competent electrocatalysts for N_2O reduction to N_2 are also thought to react with N_2O first rather than protonate.[14] While there has not been a mechanism proposed for catalytic N_2O reduction with Ni polycyclic amines, the proposed mechanism for CO_2 reduction using those catalysts to form CO also proceeds through interaction of CO_2 with the reduced metal species rather than protonation of the reduced metal to form a metal hydride.[26–28]

2.4 Conclusion

$[Pt(dmpe)_2]^{2+}$ is a known electrocatalyst for the reduction of CO_2 to formate. These studies have now also demonstrated that it is a competent electrocatalyst for N_2O reduction to N_2 and have quantified kinetic parameters associated with proposed steps in the catalytic cycle. Catalysis notably proceeds through a M-H intermediate, which has not previously been reported for other electrocatalysts for N_2O reduction. It is suggested that the species formed from reacting the Pt-H with N_2O is a platinum hydroxide species. The reaction between the Pt-H and N_2O is slow, and is likely the rate-determining step in catalysis. Further investigations are proposed to develop new N_2O reduction electrocatalysts which are not CO_2 reduction catalysts by identifying whether other metal hydrides which do not react with CO_2 can react with N_2O.

2.5 Experimental Details

General methods: All syntheses were carried out under an inert atmosphere of dinitrogen in a Vacuum Atmospheres OMNI-Lab glovebox or using standard Schlenk techniques. All electrochemical studies were carried out in an inert atmosphere of argon in a Vacuum Atmospheres OMNI-Lab glovebox. Organic solvents used during synthesis and/or manipulations were degassed by sparging with argon and dried by passing through columns of neutral alumina or molecular sieves and stored over activated 3 Å molecular sieves. Water was

obtained from a Barnstead Nanopure filtration system and was degassed under active vacuum. All deuterated solvents were purchased from Cambridge Isotope Laboratories, Inc. Deuterated solvents used for NMR (nuclear magnetic resonance) spectroscopic characterization were degassed via three freeze-pump-thaw (FPT) cycles and stored over activated 3 Å molecular sieves prior to use. All solvents and reagents were purchased from commercial vendors and used without further purification unless otherwise noted. Tetrabuylammonium hexafluorophosphate (TBAPF$_6$) used for electrochemical studies was recrystallized three times from hot ethanol. Electrochemical studies under pure N$_2$O atmospheres were performed using N$_2$O (> 99%) from Airgas.

Physical methods: ^{1}H and ^{31}P{^{1}H} nuclear magnetic resonance (NMR) spectra were collected at 298 K on a Bruker AVANCE 600 MHz spectrometer equipped with a BBFO cryoprobe or a Bruker DRX 500 MHz spectrometer equipped with a BBO probe. ^{2}H NMR spectra were collected on a Bruker AVANCE 600 MHz spectrometer equipped with a TCI probe. Chemical shifts are reported in δ units notation in parts per million (ppm). ^{1}H spectra are referenced to the residual solvent resonances of the deuterated solvent. ^{31}P{^{1}H} spectra were referenced to H$_3$PO$_4$ at 0 ppm within XwinNMR or Bruker's Topspin software, using the known frequency ratios (Ξ) of the ^{31}P standard to the lock signal of the deuterated solvent or referenced to the PF$_6$ anion. Manual shimming, Fourier transformation, and automatic spectrum phasing were performed using Xwin-NMR software when using the 500 MHz spectrometer. Spectra were analyzed and figures were generated using MestReNova 6.0.2 software. Peak integrations were calculated within MestReNova. Infrared (IR) absorption measurements were acquired as thin films on a Thermo Scientific Nicolet iS5 spectrophotometer fitted with an iD5 ATR attachment. Electrospray ionization (ESI) mass spectrometry was performed using a Waters ESI LC-TOF Micromass LCT 3 premier mass spectrometer on positive mode.

Electrochemistry: All measurements were performed on a Pine Wavedriver 10 bipotentiostat. Cyclic voltammetry was performed with a 1 mm diameter glassy carbon disc working electrode, a glassy carbon rod counter electrode, and a $Ag^{+/o}$ pseudo-reference electrode with $Fe(C_5H_5)_2$ added to the solution. Internal resistance was measured for each solution, and resistance manually compensated for between 80-90% of the measured value for each voltammogram performed. Samples for electrochemical studies performed under N_2O atmosphere were prepared by sparging the analyte solution with solvent-saturated N_2O gas prior to measurement and the headspace above the solution was blanketed with N_2O during each measurement. Controlled potential electrolysis experiments were performed in a custom H-cell with the working and counter compartments separated by a fine glass frit. The working and counter compartments were sealed with GL25 and GL18 open top caps with silicone/PTFE septa from Ace Glass. The working compartment contained: 2.0 mM catalyst, 36 mM phenol, 0.2 M $TBAPF_6$ in acetonitrile, a carbon fabric working electrode measuring 2.25"x 0.75", a $Ag^{+/o}$ pseudo-reference electrode separated from the bulk solution with a Vycor tip filled with 0.2 M $TBAPF_6$, and a mercury pool at the bottom of the compartment. The counter compartment contained 0.2 M $TBAPF_6$ in acetonitrile, 0.1 M $Fe(C_5H_5)_2$ as a sacrificial reductant, and a 1" x 2.25" piece of carbon fabric as the counter electrode. After the electrolysis period, the volume in the working compartment was measured. The headspace of the working compartment was sampled with a Restek A-2 Luer lock gas-tight syringe. Headspace nitrogen was quantified by gas chromatography using argon as the carrier gas on an Agilent 7890B instrument with a instrument with a HP-PLOT Molesieve column (19095P-MS6, 30m x 0.530 mm, 25 mm) and thermal conductivity detector (TCD).

Kinetic studies by ^{1}H NMR

$[Pt(dmpe)_2H][PF_6]$ was synthesized via hydride transfer from $NaBH_4$ in a N_2 glovebox and isolated using the method published by Miller, Labinger, and Bercaw.[29] The sample was dissolved in 0.4 mL

of CD_3CN and filtered through a glass microfiber pipette into a J. Young tube. An 0.1 mL aliquot of trimethoxybenzene (25 mM in CD_3CN) was added as an internal standard. The resulting solutions for kinetic analysis were 3.7, 11.8, and 48.3 mM [Pt]. The J. Young was freeze-pump-thawed three times using liquid N_2 to remove gaseous N_2 from the headspace and solution. A starting ^1H and $^{31}P\{^1H\}$ NMR spectrum was acquired. N_2O was then charged into the J. Young using a balloon, starting the timer at 0s. The J. Young sample was exposed to N_2O for 60s and then brought immediately to the spectrometer. ^1H spectra were acquired with 8 scans and a d1 = 1s. Concentrations of $[Pt(dmpe)_2H]^+$ were calculated using the methyl protons of the ligand (24H, 1.61 ppm) and the methoxy protons of the trimethoxybenzene standard (9H, 3.74 ppm). $^{31}P\{^1H\}$ spectra were acquired periodically to confirm the consumption of $[Pt(dmpe)_2H]^+$.

2.6 References

(1) Tian, H.; Xu, R.; Canadell, J. G.; Thompson, R. L.; Winiwarter, W.; Suntharalingam, P.; Davidson, E. A.; Ciais, P.; Jackson, R. B.; Janssens-Maenhout, G.; Prather, M. J.; Regnier, P.; Pan, N.; Pan, S.; Peters, G. P.; Shi, H.; Tubiello, F. N.; Zaehle, S.; Zhou, F.; Arneth, A.; Battaglia, G.; Berthet, S.; Bopp, L.; Bouwman, A. F.; Buitenhuis, E. T.; Chang, J.; Chipperfield, M. P.; Dangal, S. R. S.; Dlugokencky, E.; Elkins, J. W.; Eyre, B. D.; Fu, B.; Hall, B.; Ito, A.; Joos, F.; Krummel, P. B.; Landolfi, A.; Laruelle, G. G.; Lauerwald, R.; Li, W.; Lienert, S.; Maavara, T.; MacLeod, M.; Millet, D. B.; Olin, S.; Patra, P. K.; Prinn, R. G.; Raymond, P. A.; Ruiz, D. J.; van der Werf, G. R.; Vuichard, N.; Wang, J.; Weiss, R. F.; Wells, K. C.; Wilson, C.; Yang, J.; Yao, Y. A Comprehensive Quantification of Global Nitrous Oxide Sources and Sinks. *Nature* **2020**, *586* (7828), 248–256. https://doi.org/10.1038/s41586-020-2780-0.

(2) Severin, K. Synthetic Chemistry with Nitrous Oxide. *Chem. Soc. Rev.* **2015**, *44* (17), 6375–6386. https://doi.org/10.1039/C5CS00339C.

(3) Rathnayaka, S. C.; Mankad, N. P. Coordination Chemistry of the CuZ Site in Nitrous Oxide Reductase and Its Synthetic Mimics. *Coord. Chem. Rev.* **2021**, *429*, 213718. https://doi.org/10.1016/j.ccr.2020.213718.

(4) Trogler, W. C. Physical Properties and Mechanisms of Formation of Nitrous Oxide. *Coord. Chem. Rev.* **1999**, *187* (1), 303–327. https://doi.org/10.1016/S0010-8545(98)00254-9.

(5) Leont'ev, A. V.; Fomicheva, O. A.; Proskurnina, M. V.; Zefirov, N. S. Modern Chemistry of Nitrous Oxide. *Russ. Chem. Rev.* **2001**, *70* (2), 91–104. https://doi.org/10.1070/RC2001v070n02ABEH000631.

(6) Tolman, W. B. Binding and Activation of N2O at Transition-Metal Centers: Recent Mechanistic Insights. *Angew. Chem. Int. Ed.* **2010**, *49* (6), 1018–1024. https://doi.org/10.1002/anie.200905364.

(7) Ortega-Lepe, I.; Sánchez, P.; Santos, L. L.; Lara, P.; Rendón, N.; López-Serrano, J.; Salazar-Pereda, V.; Álvarez, E.; Paneque, M.; Suárez, A. Catalytic Nitrous Oxide Reduction with H2 Mediated by Pincer Ir Complexes. *Inorg. Chem.* **2022**, *61* (46), 18590–18600. https://doi.org/10.1021/acs.inorgchem.2c02963.

(8) Jurt, P.; Abels, A. S.; Gamboa-Carballo, J. J.; Fernández, I.; Le Corre, G.; Aebli, M.; Baker, M. G.; Eiler, F.; Müller, F.; Wörle, M.; Verel, R.; Gauthier, S.; Trincado, M.; Gianetti, T. L.; Grützmacher, H. Reduction of Nitrogen Oxides by Hydrogen with Rhodium(I)−Platinum(II) Olefin Complexes as Catalysts. *Angew. Chem. Int. Ed.* **2021**, *60* (48), 25372–25380. https://doi.org/10.1002/anie.202109642.

(9) Zeng, R.; Feller, M.; Ben-David, Y.; Milstein, D. Hydrogenation and Hydrosilylation of Nitrous Oxide Homogeneously Catalyzed by a Metal Complex. *J. Am. Chem. Soc.* **2017**, *139* (16), 5720–5723. https://doi.org/10.1021/jacs.7b02124.

(10) Kaplan, A. W.; Bergman, R. G. Nitrous Oxide Mediated Oxygen Atom Insertion into a Ruthenium−Hydride Bond. Synthesis and Reactivity of the Monomeric Hydroxoruthenium

Complex (DMPE) ₂ Ru(H)(OH). *Organometallics* **1997**, *16* (6), 1106–1108.

https://doi.org/10.1021/om960991i.

(11) Kaplan, A. W.; Bergman, R. G. Nitrous Oxide Mediated Synthesis of Monomeric

Hydroxoruthenium Complexes. Reactivity of (DMPE) ₂ Ru(H)(OH) and the Synthesis of a

Silica-Bound Ruthenium Complex. *Organometallics* **1998**, *17* (23), 5072–5085.

https://doi.org/10.1021/om980295d.

(12) Deeba, R.; Molton, F.; Chardon-Noblat, S.; Costentin, C. Effective Homogeneous Catalysis of

Electrochemical Reduction of Nitrous Oxide to Dinitrogen at Rhenium Carbonyl Catalysts.

ACS Catal. **2021**, *11* (10), 6099–6103. https://doi.org/10.1021/acscatal.1c01197.

(13) Taniguchi, I.; Shimpuku, T.; Yamashita, K.; Ohtaki, H. Electrocatalytic Reduction of Nitrous

Oxide to Dinitrogen at a Mercury Electrode Using Niii Complexes of Macrocyclic

Polyamines. *J. Chem. Soc. Chem. Commun.* **1990**, No. 13, 915–917.

https://doi.org/10.1039/C39900000915.

(14) Collman, J. P.; Marrocco, M.; Elliott, C. M.; L'Her, M. Electrocatalysis of Nitrous Oxide

Reduction: Comparison of Several Porphyrins and Binary "Face-to-Face" Porphyrins. *J.

Electroanal. Chem. Interfacial Electrochem.* **1981**, *124* (1), 113–131.

https://doi.org/10.1016/S0022-0728(81)80289-6.

(15) Ceballos, B. M.; Yang, J. Y. Directing the Reactivity of Metal Hydrides for Selective CO2

Reduction. *Proc. Natl. Acad. Sci.* **2018**, *115* (50), 12686–12691.

https://doi.org/10.1073/pnas.1811396115.

(16) Ceballos, B. M.; Yang, J. Y. Highly Selective Electrocatalytic CO2 Reduction by

[Pt(Dmpe)2]2+ through Kinetic and Thermodynamic Control. *Organometallics* **2020**, *39*

(9), 1491–1496. https://doi.org/10.1021/acs.organomet.9b00720.

(17) Kohl, S. W.; Weiner, L.; Schwartsburd, L.; Konstantinovski, L.; Shimon, L. J. W.; Ben-David,

Y.; Iron, M. A.; Milstein, D. Consecutive Thermal H2 and Light-Induced O2 Evolution from

Water Promoted by a Metal Complex. *Science* **2009**, *324* (5923), 74–77. https://doi.org/10.1126/science.1168600.

(18)   Burn, M. J.; Fickes, M. G.; Hartwig, J. F.; Hollander, F. J.; Bergman, R. G. Synthesis of Monomeric Ruthenium Hydroxo Complexes (PMe3)4Ru(R)(OH) (R = H, Me) and a Unique Dimeric Ruthenium Hydroxo-Water Complex [Trans-Ru(H)(OH)(DMPE)2.Cntdot.H2O]2. *J. Am. Chem. Soc.* **1993**, *115* (13), 5875–5876. https://doi.org/10.1021/ja00066a086.

(19)   Nicholson, R. S.; Shain, Irving. Theory of Stationary Electrode Polarography. Single Scan and Cyclic Methods Applied to Reversible, Irreversible, and Kinetic Systems. *Anal. Chem.* **1964**, *36* (4), 706–723. https://doi.org/10.1021/ac60210a007.

(20)   Savéant, J.-M. *Elements of Molecular and Biomolecular Electrochemistry: An Electrochemical Approach to Electron Transfer Chemistry*, 1st ed.; Wiley-Interscience, 2006.

(21)Kunerth, W. Solubility of C O 2 and N 2 O in Certain Solvents. *Phys. Rev.* **1922**, *19* (5), 512–524. https://doi.org/10.1103/PhysRev.19.512.

(22)   Tomita, Y.; Teruya, S.; Koga, O.; Hori, Y. Electrochemical Reduction of Carbon Dioxide at a Platinum Electrode in Acetonitrile-Water Mixtures. *J. Electrochem. Soc.* **2000**, *147* (11), 4164. https://doi.org/10.1149/1.1394035.

(23)   Cunningham, D. W.; Yang, J. Y. Kinetic and Mechanistic Analysis of a Synthetic Reversible CO2/HCO2– Electrocatalyst. *Chem. Commun.* **2020**, *56* (85), 12965–12968. https://doi.org/10.1039/D0CC05556E.

(24)   Yu, H.; Jia, G.; Lin, Z. Theoretical Studies on O-Insertion Reactions of Nitrous Oxide with Ruthenium Hydride Complexes. *Organometallics* **2008**, *27* (15), 3825–3833. https://doi.org/10.1021/om8000845.

(25)   Escayola, S.; Solà, M.; Poater, A. Mechanism of the Facile Nitrous Oxide Fixation by Homogeneous Ruthenium Hydride Pincer Catalysts. *Inorg. Chem.* **2020**, *59* (13), 9374–9383. https://doi.org/10.1021/acs.inorgchem.0c01252.

(26)   Beley, Marc.; Collin, J. Paul.; Ruppert, Romain.; Sauvage, J. Pierre. Electrocatalytic

Reduction of Carbon Dioxide by Nickel Cyclam2+ in Water: Study of the Factors Affecting

the Efficiency and the Selectivity of the Process. *J. Am. Chem. Soc.* **1986**, *108* (24), 7461–

7467. https://doi.org/10.1021/ja00284a003.

(27)   Collin, J. P.; Jouaiti, A.; Sauvage, J. P. Electrocatalytic Properties of

(Tetraazacyclotetradecane)Nickel(2+) and Ni2(Biscyclam)4+ with Respect to Carbon

Dioxide and Water Reduction. *Inorg. Chem.* **1988**, *27* (11), 1986–1990.

https://doi.org/10.1021/ic00284a030.

(28)   Song, J.; Klein, E. L.; Neese, F.; Ye, S. The Mechanism of Homogeneous CO2 Reduction

by Ni(Cyclam): Product Selectivity, Concerted Proton–Electron Transfer and C–O Bond

Cleavage. *Inorg. Chem.* **2014**, *53* (14), 7500–7507. https://doi.org/10.1021/ic500829p.

(29)   Miller, A. J. M.; Labinger, J. A.; Bercaw, J. E. Homogeneous CO Hydrogenation: Ligand

Effects on the Lewis Acid-Assisted Reductive Coupling of Carbon Monoxide.

Organometallics **2010**, *29* (20), 4499–4516. https://doi.org/10.1021/om100638d.

Chapter 3: Reactivity of Late Transition Metal Hydrides with Nitrous Oxide

3.1 Introduction

Nitrous oxide (N_2O) is known to be a thermodynamically strong oxidant, yet kinetically inert as a substrate.[1–3] It is also isoelectronic to CO_2; thus, electrocatalysts for N_2O reduction to N_2 have primarily been developed from previously known CO_2 reduction catalysts.[4–6] However, the two-electron and two-proton reduction of N_2O (Eq 3.1) is more exergonic than the analogous reduction of CO_2 to CO (Eq 3.2) or the other two-electron, one-proton reduction of CO_2 to formate (HCO_2^-) of those of CO_2 (Eq 3.3)[7–9].

$$N_2O \; + \; 2H^+ \; + \; 2e^- \longrightarrow N_2 \; + \; H_2O \qquad \begin{array}{l} \Delta G° = \text{-81.1 kcal/mol} \\ \Delta E° = \text{1.76 V vs. NHE} \end{array} \qquad \text{(Eq 3.1)}$$

$$CO_2 \; + \; H^+ \; + \; 2e^- \longrightarrow HCO_2H \qquad \begin{array}{l} \Delta G° = \text{22.6 kcal/mol} \\ \Delta E° = \text{-0.49 V vs. NHE} \end{array} \qquad \text{(Eq 3.2)}$$

$$CO_2 \; + \; 2H^+ \; + \; 2e^- \longrightarrow CO \; + \; H_2O \qquad \begin{array}{l} \Delta G° = \text{24.4 kcal/mol} \\ \Delta E° = \text{-0.53 V vs. NHE} \end{array} \qquad \text{(Eq 3.3)}$$
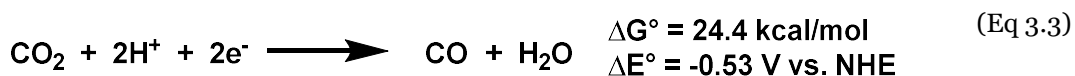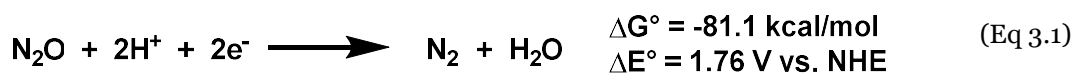
These differences in free energy suggest that electrocatalysis for N_2O reduction could occur at milder potentials compared to CO_2 reduction.

Hydricity, a thermodynamic parameter used for both organic and inorganic hydrides,[10,11] is defined as the free energy for hydride release. For a transition metal hydride (M-H), hydricity is thus the free energy associated with the heterolytic cleavage of the M-H bond:

$$MH \; \rightleftharpoons \; M^+ \; + \; H^- \qquad \Delta G° = \Delta G_{H^-} \qquad \text{(Eq. 3.4)}$$
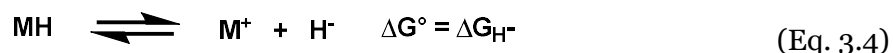
Formate (HCO_2^-) is a two-electron reduction product of CO_2 and its hydricity has been experimentally determined to be 44 kcal/mol in MeCN.[12]

$$HCO_2^- \; \rightleftharpoons \; CO_2 \; + \; H^- \qquad \Delta G_{H^-} = \text{44 kcal/mol (MeCN)} \qquad \text{(Eq 3.5)}$$
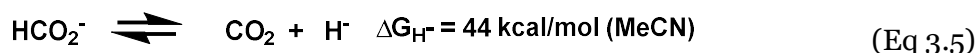
Lower hydricity values correspond to stronger hydride donors. Consequently, hydride transfer from transition metal hydrides with a hydricity below 44 kcal/mol to CO_2 to produce

formate is exergonic. In contrast, the reaction of weaker hydride donors (ΔG_{H^-} > 44 kcal/mol) with CO_2 is endergonic.

While N_2O reactivity with M-H complexes may not involve an explicit hydride transfer, hydricity can still be used as a parameter to identify less reducing metal hydrides (since they will be weaker hydride donors).[13] In the previous chapter, N_2O reactivity and catalysis were demonstrated with $[Pt(dmpe)_2H]^+$ (dmpe = 1,2-*bis*(dimethylphosphino)ethane), a known CO_2 to HCO_2^- reduction catalyst. Nitrous oxide reactivity with transition metal hydrides has also previously been demonstrated with ruthenium,[14,15] niobium,[16] and cobalt hydrides;[17] this reactivity with metal hydrides is also implicated in catalytic cycles for the reduction of N_2O using Ir and Ru pincer complexes[18,19] as well as a bimetallic Rh-Pt system.[20]

Several different transition metal hydrides with experimentally determined hydricity values were investigated to identify a trend or upper bound for N_2O reactivity (**Chart 3.1**). The reactivity of $Ir(POCOP^{tBu})H_2$, another known CO_2 to HCO_2^- reduction catalyst which has a calculated hydricity value of 45.1 kcal/mol in MeCN was also investigated.[21,22] This study focused on transition metal hydrides of the form $[ML_2H]^+$ (L = 1,2-*bis*(dimethylphosphino)ethane (dmpe) or 1,2-*bis*(diethylphosphino)ethane (depe)) in group 10 with hydricities that span a range of almost 15 kcal/mol in MeCN.
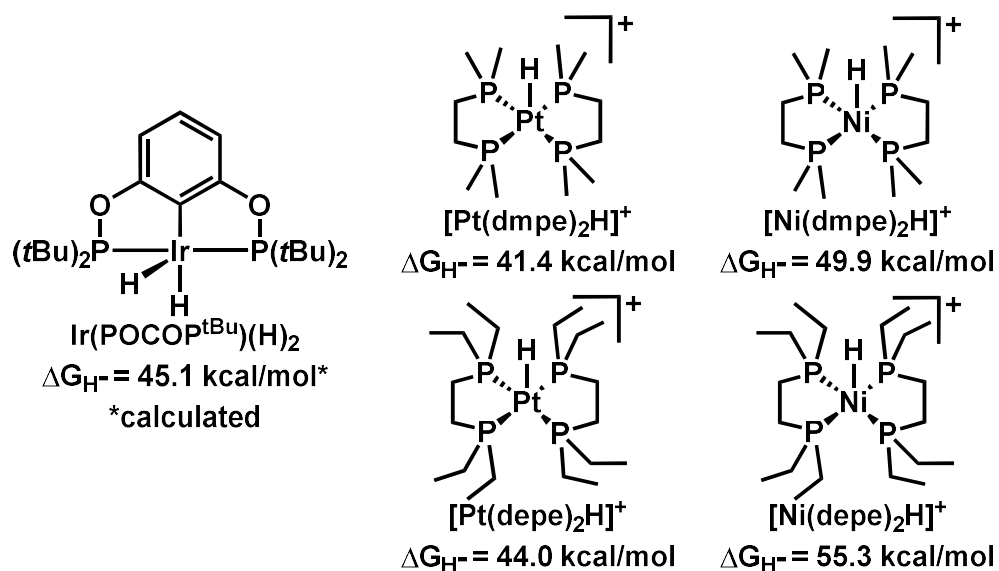
Chart 3.1. Metal hydrides investigated for N_2O reactivity and their corresponding hydricity values in MeCN.

3.2 Results

3.2.1 Reactivity with Ir(POCOP)H$_2$

Ir(POCOP^{tBu})H$_2$ has a calculated hydricity value of 45.1 kcal/mol in neat MeCN.[22] In the absence of water, it is not a sufficiently strong hydride donor to reduce CO_2 to formate; it becomes a competent hydride donor to CO_2 when 5% water is added to the solution due to favorable stabilization of the formate anion in water. Selective electrocatalytic reduction of CO_2 to formate has been demonstrated using 5% water in MeCN.[21]

Ir(POCOP^{tBu})H$_2$ was synthesized according to the published literature procedure.[23] When it is exposed to an atmosphere of N_2O overnight, the solution changes from dark red to dark brown (**Scheme 3.1**).

Scheme 3.1. Reaction between Ir(POCOP^{tBu})H$_2$ and N$_2$O.
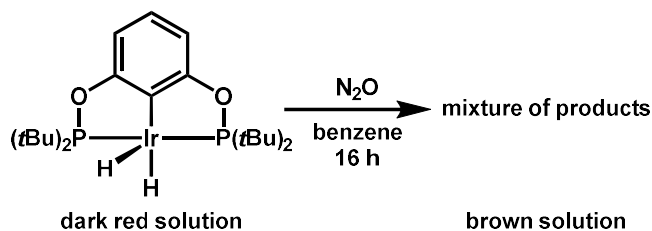
Some remaining dihydride is observed in the ^{1}H NMR spectrum (**Figure 3.1**). ^{31}P{^{1}H} NMR spectra show significant (but not complete) consumption of the starting dihydride with a mixture of species observed (**Figure 3.2**).
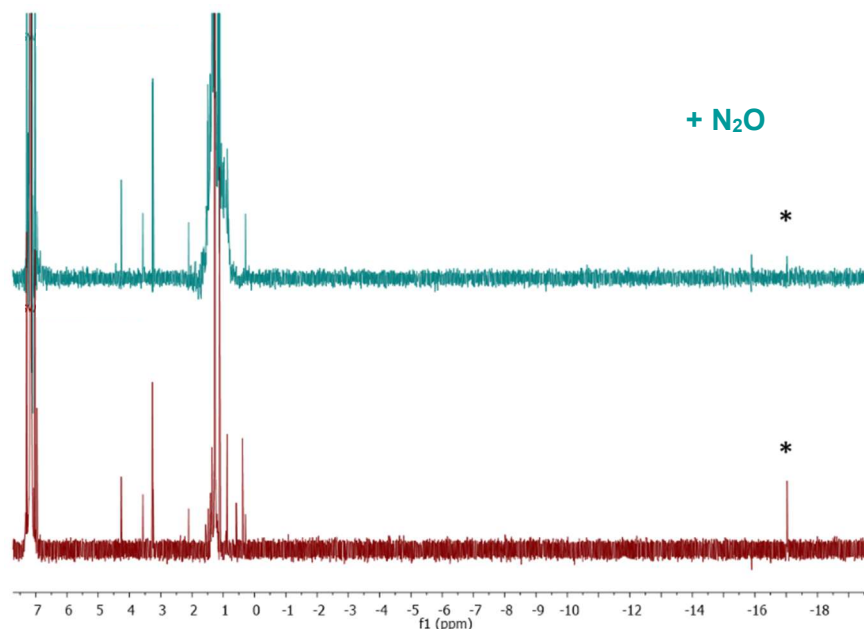
Figure 3.1. ^{1}H NMR spectra acquired in C$_6$D$_6$. *Top*: reaction mixture after 16h exposure to N$_2$O. *Bottom*: starting Ir(POCOP^{tBu})H$_2$. * denotes the dihydride resonance at δ = -17.04 ppm.
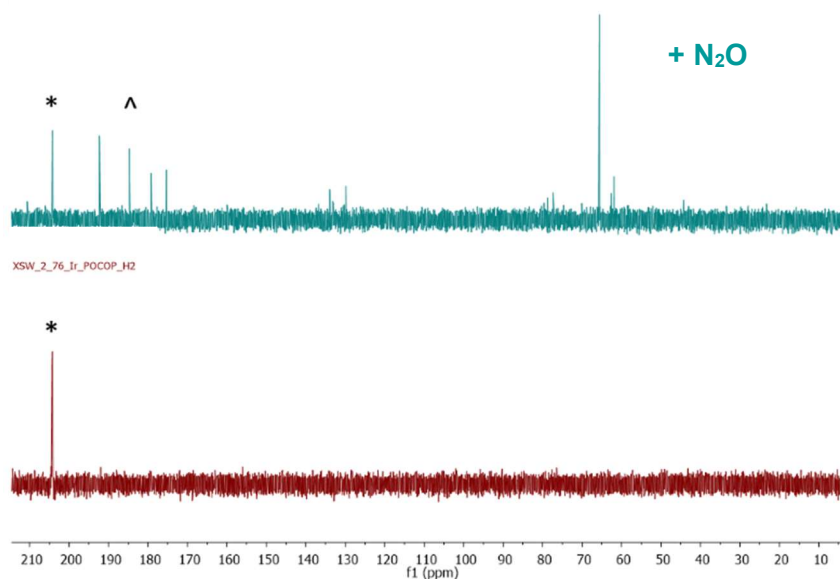
Figure 3.2. $^{31}P\{^1H\}$ NMR spectra acquired in C_6D_6. *Top*: reaction mixture after 16h exposure to N_2O showing a mixture of species. *Bottom*: starting $Ir(POCOP^{tBu})H_2$. * denotes the dihydride resonance at δ = 204.9 ppm. ^ denotes the proposed N_2-bridged dimer at δ = 184.7 ppm.

Notably, the $^{31}P\{^1H\}$ NMR spectrum contains a feature at 184.7 ppm which may correspond to

an Ir dimer species with an end-on bridging N_2 (**Scheme 3.3**). An Ir dimer complex,

$[\{Ir(POCOP^{tBu}\text{-}p\text{-}Ph^{CF3})\}_2\{\mu\text{-}N_2\}]$, with a bridging end-on molecule of N_2 has previously been

identified with a $^{31}P\{^1H\}$ NMR feature at 185.5 ppm.[23]

Scheme 3.3. Proposed end-on N_2 bridging Ir dimer.
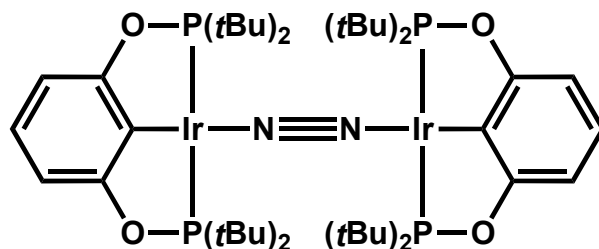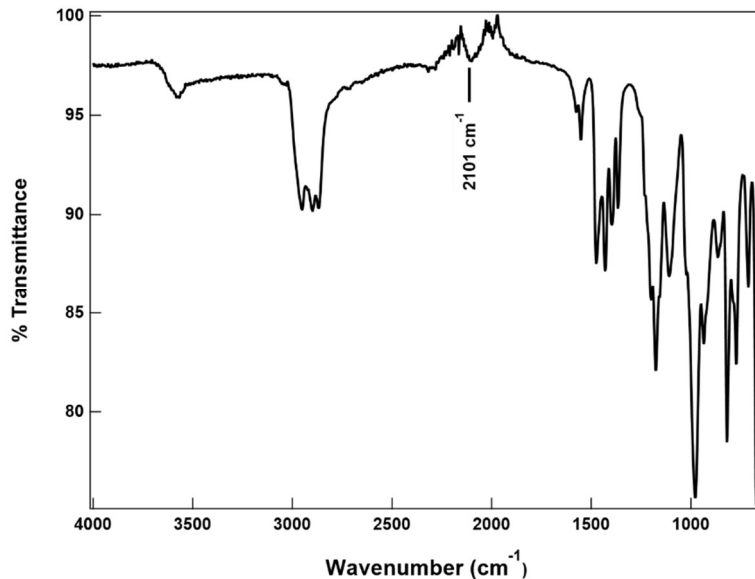
Figure 3.3. Solid-state IR spectrum of reaction mixture between $Ir(POCOP^{tBu})H_2$ and N_2O.

The IR spectrum acquired of the reaction mixture between $Ir(POCOP^{tBu})H_2$ and N_2O (**Figure 3.3**) contains a feature that may be consistent with an end-on bound-N_2 stretch at 2101 cm^{-1}. The spectrometer contains a known aberration in the baseline between 2200-2000 cm^{-1} making it difficult to determine if this feature arises from the sample. Additionally, the parent $Ir(POCOP^{tBu})H_2$ is reported to have a feature in this region, further making any assignment ambiguous.[23]

Ir(POCOP^{tBu}) catalysts used for catalytic dehydrogenation of alkanes are known to react with N_2 to form dimers similar to the $[\{Ir(POCOP^{tBu}\text{-}p\text{-}Ph^{CF3})\}_2\{\mu\text{-}N_2\}]$ dimer mentioned above. These dimers inhibit catalysis. The N_2-bound dimer has been demonstrated to convert back to the catalytically active dihydride when exposed to an atmosphere of H_2.[23] Nonetheless, given the inhibitory role of N_2 (the product of N_2O reduction), and the incomplete reactivity between $Ir(POCOP^{tBu})H_2$ and N_2O, other metal hydrides were investigated for N_2O reactivity.

3.2.2 Reactivity with [Pt(depe)₂H]⁺

[Pt(depe)$_2$H]⁺ has an experimentally determined hydricity of 44 kcal/mol in MeCN,[24] and it is an electrocatalyst for the reversible conversion of CO_2 to formate.[25]

[Pt(depe)$_2$H][PF$_6$] was synthesized according to literature procedure.[26] When a sample of [Pt(depe)$_2$H][PF$_6$] is exposed to 1 atm of N_2O, no immediate change is apparent in the ¹H or ³¹P{¹H} NMR spectra (**Figure 3.4**, **3.5**). After 19 hours, <10% consumption of the platinum hydride is observed and a new species, [Pt(depe)$_2$]²⁺, is observed by ³¹P{¹H} NMR spectrum (Figure 3.5). [Pt(depe)$_2$]²⁺ is the product of hydride transfer from [Pt(depe)$_2$H]⁺. Notably, in contrast to the [Pt(dmpe)$_2$H]⁺ reaction discussed in Ch. 2, the $^1J_{Pt-P}$ coupling constant for this new species is the same that reported for [Pt(depe)$_2$]²⁺,[26] indicating that this reaction is unlikely to be forming the corresponding hydroxide complex after hydride transfer.
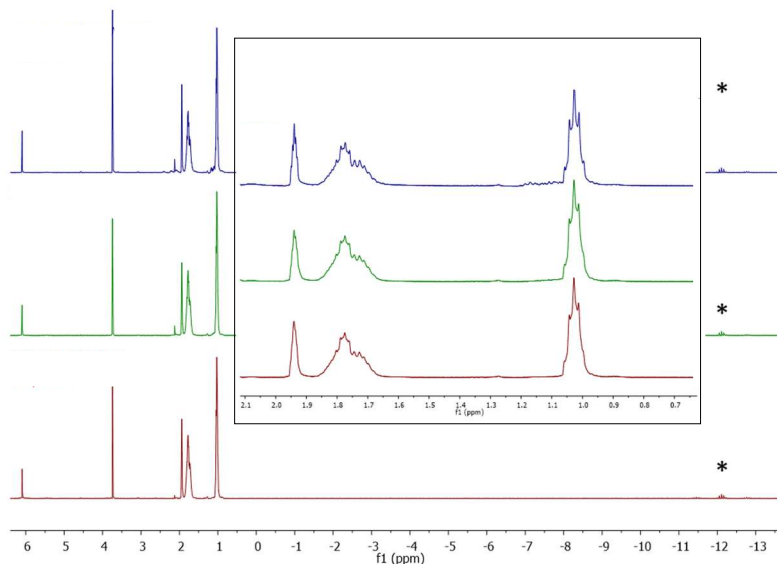
Figure 3.4. ^{1}H NMR spectra of [Pt(depe)$_2$H]$^+$ acquired in CD$_3$CN. *Top*: reaction mixture after 19h exposure to N$_2$O. *Middle*: reaction mixture after 75m exposure to N$_2$O. *Bottom*: starting [Pt(depe)$_2$H][PF$_6$]. *Inset*: alkyl region. * denotes the hydride resonance at δ = -12.12 ppm.
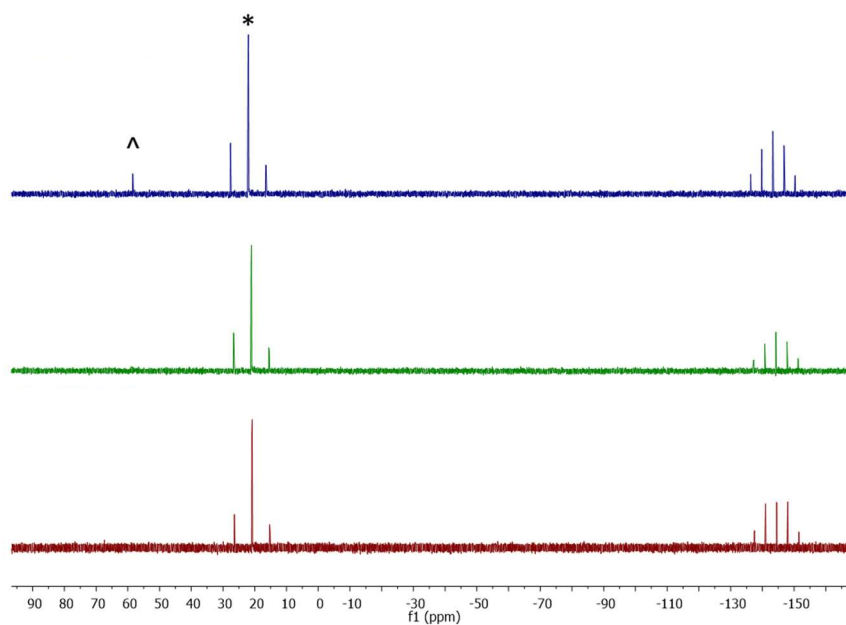
Figure 3.5. ^{31}P{^{1}H} NMR spectra of [Pt(depe)$_2$H]$^+$ acquired in CD$_3$CN. *Top*: reaction mixture after 19h exposure to N$_2$O. *Middle*: reaction mixture after 75m exposure to N$_2$O. *Bottom*: starting [Pt(depe)$_2$H][PF$_6$]. * denotes [Pt(depe)$_2$H]$^+$ at δ = 22.1 ppm. ^ denotes [Pt(depe)$_2$]$^{2+}$ at δ = 58.5 ppm.

3.2.3 Reactivity with [Ni(dmpe)$_2$H]$^+$

The hydricity of [Ni(dmpe)$_2$H]$^+$ has previously been quantified to be 49.9 kcal/mol in MeCN;[11,27,28] since this value is above 44 kcal/mol, this complex is consequently not a competent hydride donor to CO$_2$.

[Ni(dmpe)$_2$H][BF$_4$] was synthesized according to literature procedures.[29] In contrast to the minimal reactivity observed using [Pt(depe)$_2$H]$^+$, more rapid consumption of [Ni(dmpe)$_2$H]$^+$ is observed when the hydride is exposed to N$_2$O. After 16h, all [Ni(dmpe)$_2$H]$^+$ is consumed; the primary product observed by ^{1}H and ^{31}P{^{1}H} NMR spectroscopy is [Ni(dmpe)$_2$]$^{2+}$ (**Figure 3.6**, **3.7**). Although it is known that [Ni(dmpe)$_2$H]$^+$ releases H$_2$ [Ni(dmpe)$_2$]$^{2+}$ and [Ni(dmpe)$_2$]^0 when irradiated,[28] these samples were stored in an opaque cylinder and were only exposed to light briefly when transferred to the NMR spectrometer.
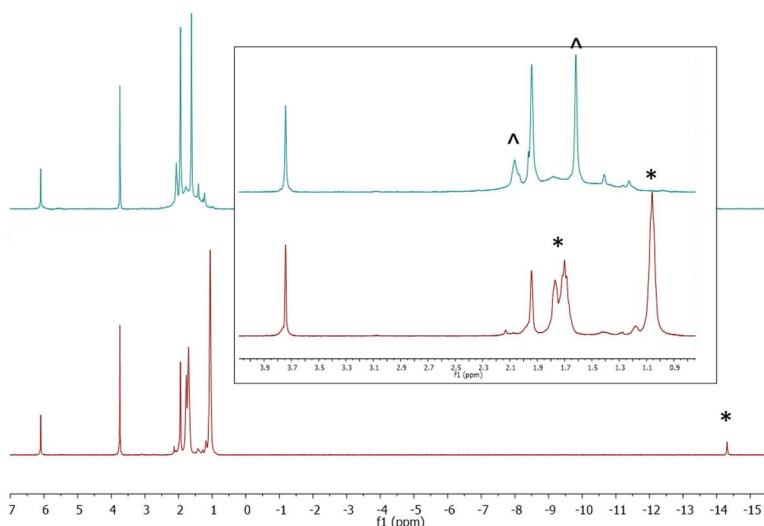
Figure 3.6. ^{1}H NMR spectra of [Ni(dmpe)$_2$H]$^+$ acquired in CD$_3$CN. *Top*: reaction mixture after 16h exposure to N$_2$O. *Bottom*: starting [Ni(dmpe)$_2$H][BF$_4$]. *Inset*: alkyl region. * denotes signals for [Ni(dmpe)$_2$H]$^+$; the hydride resonance is at -14.02 ppm. ^ denotes signals for [Ni(dmpe)$_2$]$^{2+}$.
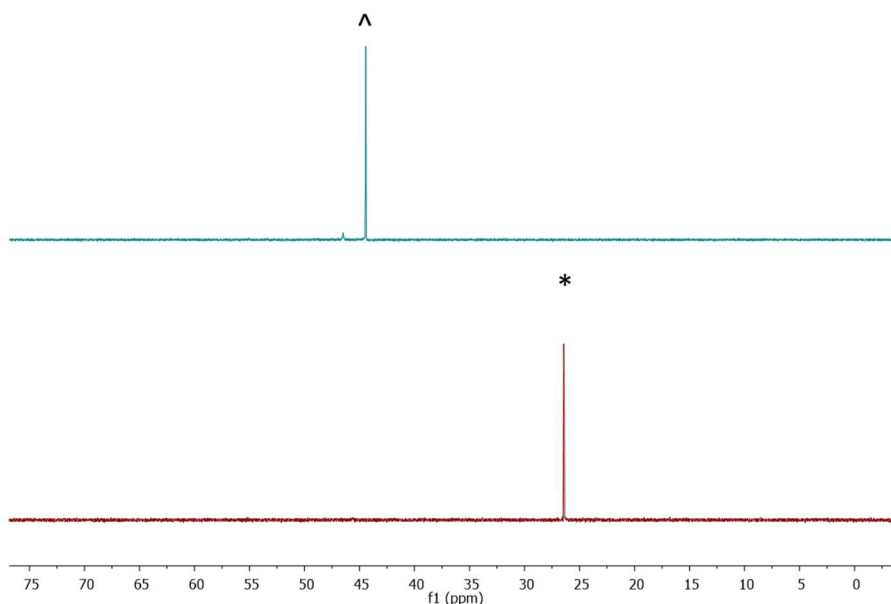
Figure 3.7. $^{31}P\{^1H\}$ NMR spectra of $[Ni(dmpe)_2H]^+$ acquired in CD_3CN. *Top*: reaction mixture after 19h exposure to N_2O. *Bottom*: starting $[Ni(dmpe)_2H][BF_4]$. * denotes $[Ni(dmpe)_2H]^+$ at δ = 24.6 ppm. ^ denotes $[Ni(dmpe)_2]^{2+}$ at δ = 48.6 ppm.

An initial k_{obs} of 1.7 x 10^{-4} s^{-1} can be calculated for $[Ni(dmpe)_2H]^+$ consumption using data from the first 12 minutes after N_2O exposure (**Figure 3.8**). This rate constant is calculated based on a pseudo-first order reaction (eq 3.6, 3.7) since the concentration of N_2O in solution should be much higher than the concentration of $[Ni(dmpe)_2H]^+$. While a precise value for the solubility of N_2O in acetonitrile has not been measured, the solubility is generally comparable to that of CO_2 in many organic solvents. The solubility of CO_2 in MeCN is 280 mM.[30,31] N_2O solubility has been experimentally measured to be as high as 620 mM in THF.[19]

$$-\frac{d[PtH^+]}{dt} = -(\text{slope}) = k_{obs}[PtH^+] \qquad \text{(eq. 3.6)}$$

$$k_{obs} = \frac{-(\text{slope})}{[PtH^+]} \qquad \text{(eq. 3.7)}$$
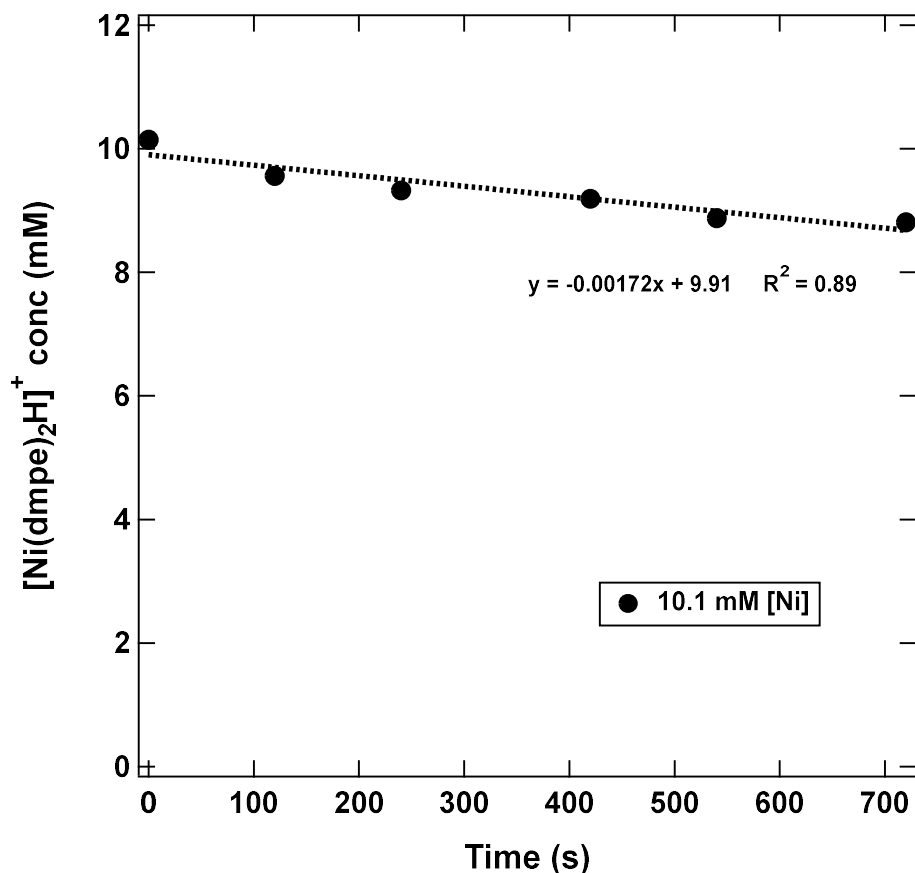
Figure 3.8. Reaction of $[Ni(dmpe)_2H]^+$ with N_2O. The dotted line represents the best linear fit for time points < 12 minutes.

3.2.4 Reactivity with $[Ni(depe)_2H]^+$

The hydricity of $[Ni(depe)_2H]^+$ has previously been quantified to be 55.3 kcal/mol in MeCN which is 13.9 kcal/mol higher than the hydricity for $[Pt(dmpe)_2H]^+$ (41.4 kcal/mol, MeCN).[27,28] $[Ni(depe)_2H]^+$ is not a competent hydride donor to CO_2 since its hydricity is higher than 44 kcal/mol. $[Ni(depe)_2H]^+$ is known to be light sensitive; samples were kept in an opaque tube until just before NMR spectra were acquired.

$[Ni(depe)_2H][BF_4]$ was synthesized in a similar manner to the published synthesis of $[Ni(dmpe)_2H][BF_4]$ using $CsHCO_2$.[29] When the solution containing $[Ni(depe)_2H]^+$ is initially exposed to N_2O, no immediate change is apparent in either the $^{31}P\{^1H\}$ NMR or ^1H NMR spectra (**Figure 3.9, 3.10**). After more than 4 days (54 h), minimal consumption of the $[Ni(depe)_2H]^+$

is observed. After 16 days (384 h), additional but not complete consumption of the hydride is observed. The reaction progress is plotted in **Figure 3.11**. As the hydride is consumed, new features appear at 48.2 ppm and 57.4 ppm in the $^{31}P\{^1H\}$ spectrum. Neither of these features correspond to the $[Ni(depe)_2]^{2+}$ species. The $[Ni(depe)_2]^0$ is known to be insoluble in CD_3CN but no precipitate was observed.[27,28]
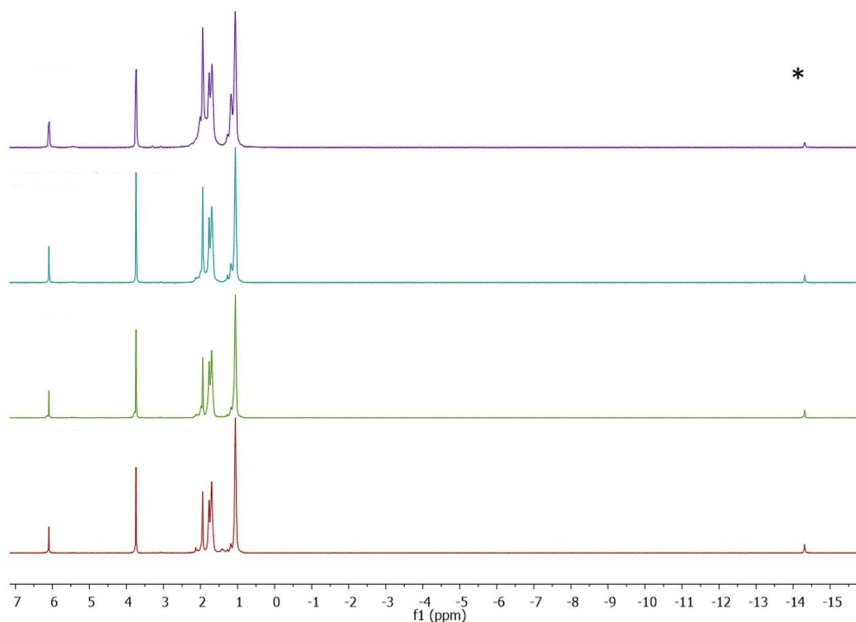
Figure 3.9. ^1H NMR spectra of $[Ni(depe)_2H]^+$ acquired in CD_3CN. *Top*: reaction mixture after 16d exposure to N_2O. *Second*: reaction mixture after 54h exposure to N_2O. *Third*: reaction mixture after 1.5h exposure to N_2O. *Bottom*: starting $[Ni(depe)_2H][BF_4]$. * denotes the hydride resonance at δ = -14.31 ppm.
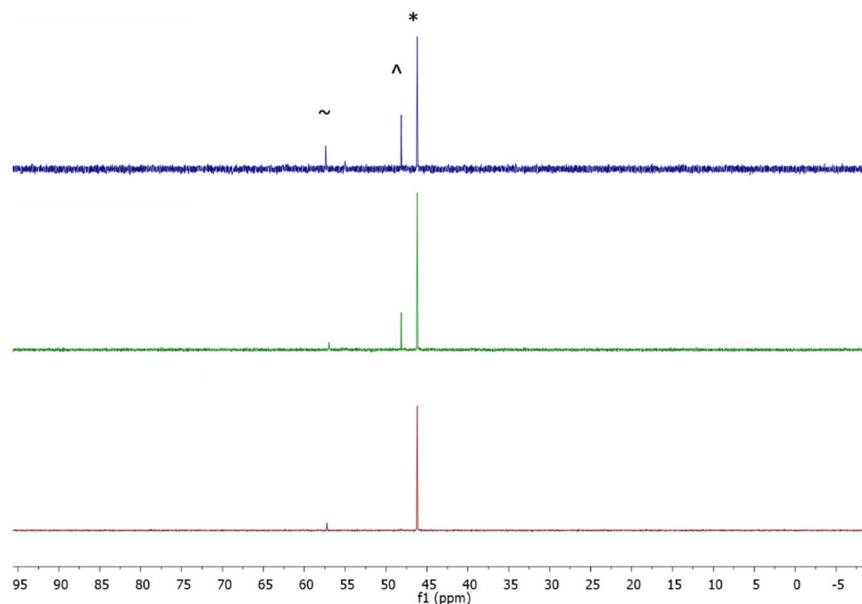
Figure 3.10. $^{31}P\{^{1}H\}$ NMR spectra of $[Ni(depe)_2H]^+$ acquired in CD_3CN. *Top*: reaction mixture after 16d exposure to N_2O. *Middle*: reaction mixture after 54h exposure to N_2O. *Bottom*: starting $[Ni(depe)_2H][BF_4]$. * denotes $[Ni(depe)_2H]^+$ at $\delta = 46.2$ ppm. ^ denotes a new unknown species at $\delta = 48.2$ ppm. ~ denotes a new unknown species at $\delta = 57.4$ ppm.
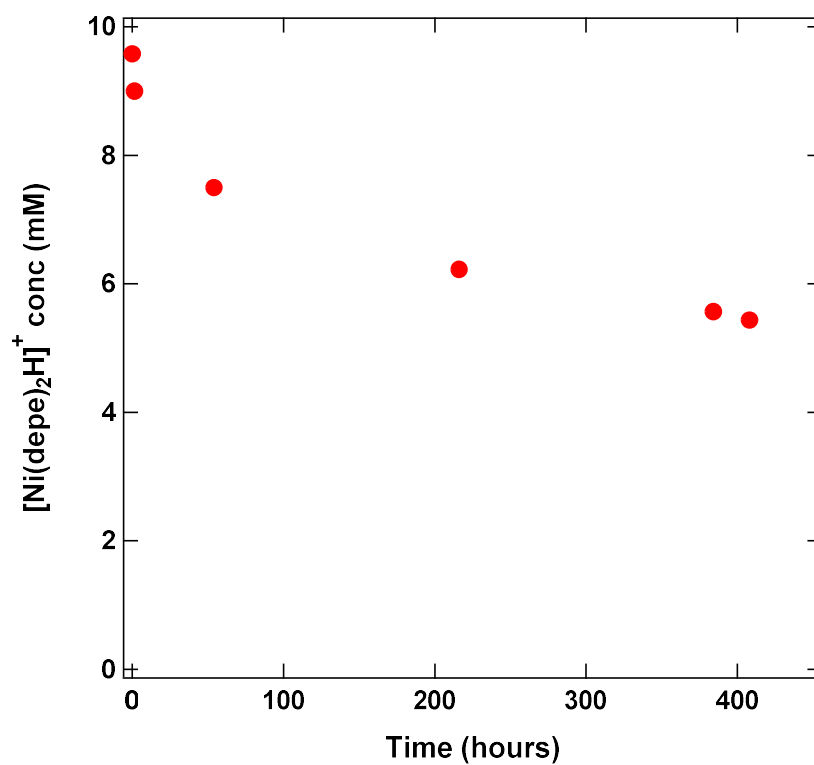
Figure 3.11. Reaction of $[Ni(depe)_2H]^+$ with N_2O.

3.2.5 Electrochemistry with [Ni(depe)₂H]⁺

The electrochemical behavior of $[Ni(depe)_2]^{2+}$ and pK_a of the hydride, $[Ni(depe)_2H]^+$ have previously been characterized by Dubois and coworkers. The pK_a of the nickel hydride was experimentally determined to be 23.8 in benzonitrile; its pK_a should be similar in MeCN.[27] Consequently, $HNEt_3^+$ (pK_a = 18.8 in MeCN) was selected as an acid that would be sufficiently acidic to generate the desired $[Ni(depe)_2H]^+$ electrochemically without further protonating the hydride to make H_2.[32]

Cyclic voltammograms of $[Ni(depe)_2]^{2+}$ show two reversible one electron features at $E_{1/2}$ (Ni²⁺/⁺) = - 1.16 and $E_{1/2}$ (Ni⁺/⁰) = - 1.29 V vs. $Fe(C_5H_5)_2^{+/0}$ in MeCN. When 3 eq of HNE_3^+ are added, the Ni⁺/⁰ couple becomes irreversible at 100 mV/s and the E_{pc} shifts cathodically by 10 mV. The oxidation feature of the Ni²⁺/⁺ couple is attenuated and the E_{pa} and E_{pc} of the Ni²⁺/⁺ also shift cathodically by 10 mV. When N_2O is sparged into the solution with 3 eq of acid present, the potentials shift anodically by about 20 mV, but no current enhancement is observed, suggesting that no catalysis is occurring.
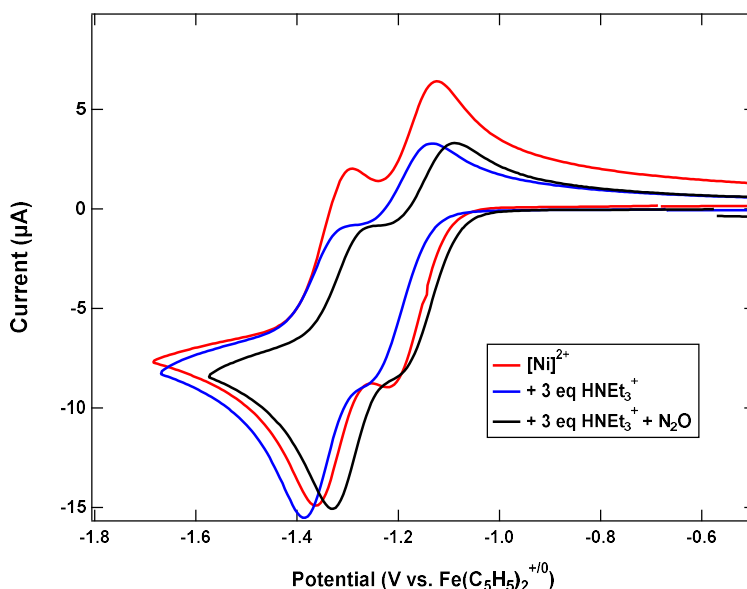
Figure 3.12. Cyclic voltammograms of 1 mM $[Ni(depe)_2][BF_4]_2$ in 0.2 M TBAPF₆ MeCN (**red**), after addition of 3 eq of $HNEt_3^+$ (**blue**), and after addition of acid and 1 atm of N_2O (**black**). Scan rate = 100 mV/s.

A controlled potential electrolysis experiment was conducted using 2 mM [Ni(depe)$_2$]$^{2+}$ and 20 eq of HNEt$_3$$^+$. The solution was electrolyzed at −1.50 V vs. Fe(C$_5$H$_5$)$_2$$^{+/0}$ in the dark. Approximately 3.7 C of charge, corresponding to 2.2 eq of electrons per [Ni(depe)$_2$]$^{2+}$ is passed in the first 12 minutes; the current significantly decreases after this time (**Figure 3.13**). The slight increase in current after 2000 seconds is attributed to solution drift between the working and counter-electrode compartments and some light exposure.
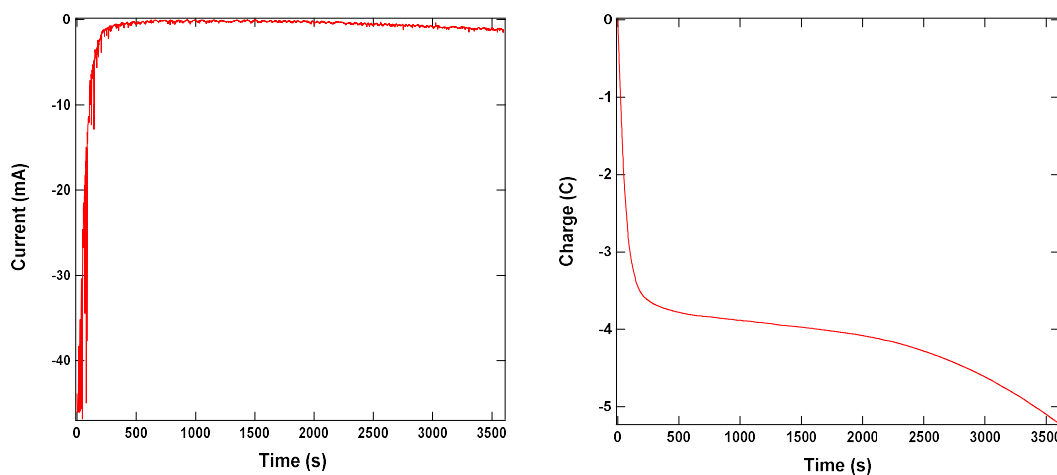
Figure 3.13. Controlled potential electrolysis at −1.50 V vs. Fe(C$_5$H$_5$)$_2$$^{+/0}$ in the dark using 2 mM [Ni(depe)$_2$]$^{2+}$ and 20 eq of HNEt$_3$$^+$. *Left*: Current passed over 1h. *Right*: Accumulated charge over 1 h.

No N$_2$ is detected after 1 h of electrolysis. The ^{31}P{^{1}H} NMR spectrum of the post-electrolysis solution contains primarily [Ni(depe)$_2$H]$^+$ and some [Ni(depe)$_2$]$^{2+}$ (**Figure 3.14**). The other species observed during stoichiometric activity (at 57.4 and 48.2 ppm) are not observed in the post-electrolysis solution.
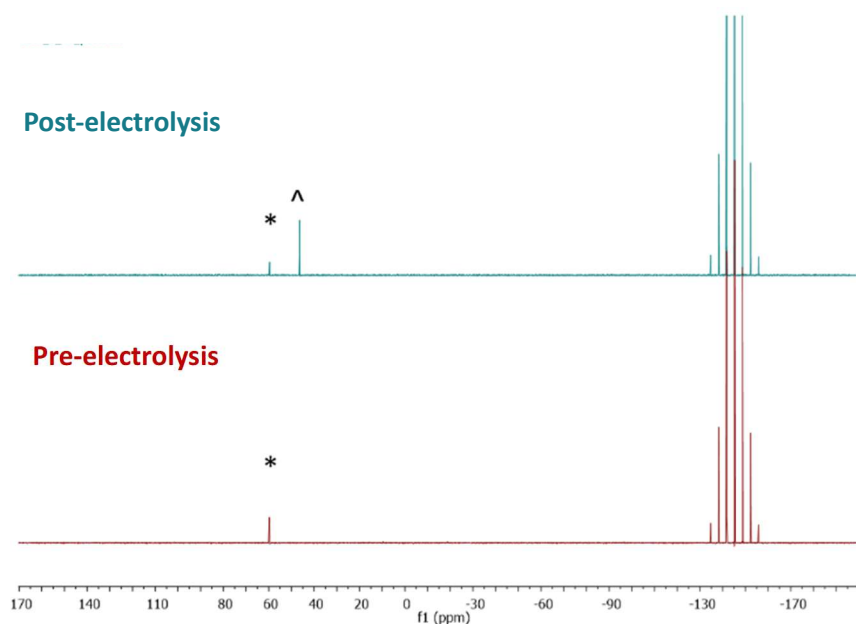
Figure 3.14. $^{31}P\{^1H\}$ NMR spectra of pre-electrolysis (*bottom*) and post-electrolysis solutions (*top*) showing [Ni(depe)$_2$H]$^+$ and [Ni(depe)$_2$]$^{2+}$ and PF$_6^-$ with no other species formed. Spectra were acquired in MeCN. * denotes [Ni(depe)$_2$]$^{2+}$ at δ = 59.4 ppm. ^ denotes [Ni(depe)$_2$H]$^+$ at δ = 46.2 ppm.

3.3 Discussion

Table 3.1. Summary of N$_2$O reactivity with metal hydrides investigated.

Complex	ΔG_{H^-} (kcal/mol, MeCN)	pK_a	Consumption of M-H with 1 atm of N$_2$O in 20h	Products observed
[Pt(dmpe)$_2$H]$^+$	41.4	31.1	Complete	Mixture, contains [Pt(dmpe)$_2$OH]$^+$
[Pt(depe)$_2$H]$^+$	44.0	29.7	Incomplete (< 10%)	[Pt(depe)$_2$]$^{2+}$, [Pt(depe)$_2$H]$^+$
Ir(POCOP^{tBu})H$_2$	45.1*	36.6**	Incomplete	Mixture, starting material
[Ni(dmpe)$_2$H]$^+$	49.9	24.3	Complete	[Ni(dmpe)$_2$]$^{2+}$
[Ni(depe)$_2$H]$^+$	55.3	23.8	Incomplete	Mixture, starting material

*Hydricity determined computationally. See ref. 22. **pK_a calculated based on computed hydricity and known 2 e$^-$ reduction potential (p$K_a = \Delta G_{H^-} + 46.12 * E_{1/2} - 79.8\frac{\text{kcal}}{\text{mol}}$) where ΔG_{H^-} is 45.1 kcal/mol, $E_{1/2}$ is $-$ 1.83 V vs. Fe(C$_5$H$_5$)$_2^{+/0}$, and 79.8 kcal/mol corresponds to the free energy of H$^+$ + 2 e$^-$ $\rightleftharpoons$ H$^-$ in MeCN.

Table 3.1 summarizes the reactivity of the metal hydrides investigated. Due to varying time points measured, consumption is noted after 20h of exposure to N_2O. The two M-H species shown to completely react with N_2O within 20h are $[Pt(dmpe)_2H]^+$ and $[Ni(dmpe)_2H]^+$. In contrast, $[Ni(depe)_2H]^+$ is not fully consumed even when exposed to 1 atm of N_2O for 16 days. Controlled potential electrolysis using $[Ni(depe)_2]^{2+}$ and 20 eq of an appropriate acid, $HNEt_3^+$, in an N_2O atmosphere produced no detectable N_2 and demonstrates the persistence of $[Ni(depe)_2H]^+$ in the presence of nitrous oxide.

The initial rate of reactivity of these complexes does not appear to correlate with their measured hydricities. $[Ni(dmpe)_2H]^+$ is a weaker hydride donor than both $Ir(POCOP^{tBu})$ and $[Pt(depe)_2H]^+$ yet shows complete consumption of the hydride within 20h. Less than 10% of $[Pt(depe)_2H]^+$ is consumed in the same time. No internal standard was used with the $Ir(POCOP^{tBu})H_2$ reaction, so accurate concentrations cannot be determined but some remaining dihydride is observed by ^1H and $^{31}P\{^1H\}$ NMR spectroscopy. Reactivity with N_2O also does not appear to significantly correlate with pK_a values of the metal hydride. $[Pt(dmpe)_2H]^+$ is a much weaker acid than $[Ni(depe)_2H]^+$ (pK_a = 31.1 vs. 24.3) and the platinum hydride reacts much more rapidly than nickel. However, $[Ni(dmpe)_2H]^+$ and $[Ni(depe)_2H]^+$ have more similar pK_a values (23.8 vs. 24.3) yet the former is completely consumed upon N_2O exposure while the latter persists for weeks.

The products detected after the M-H reacts with N_2O are also not consistent. In the previous chapter, it is demonstrated that the primary species observed in the $^{31}P\{^1H\}$ NMR spectrum after $[Pt(dmpe)_2H]^+$ reacts with N_2O is likely $[Pt(dmpe)_2OH]^+$. In contrast, $[Pt(depe)_2]^{2+}$ is detected after $[Pt(depe)_2H]^+$ is exposed to N_2O after 19h and no other species are observed in the $^{31}P\{^1H\}$ NMR spectrum. When $[Ni(dmpe)_2H]^+$ reacts with N_2O, only $[Ni(dmpe)_2]^{2+}$ is detected. While two new species are observed from the reaction with $[Ni(depe)_2H]^+$, neither species corresponds to $[Ni(depe)_2]^{2+}$.

3.4 Conclusion

A series of transition metal hydride complexes were reacted with N_2O to identify candidates for electrocatalytic N_2O reduction at milder potentials than those used for CO_2 reduction. Consumption of the hydrides under 1 atm of N_2O does not appear to correlate with known hydricity or pK_a values. While the $[ML_2]^{2+}$ (L = dmpe or depe) species is observed from the reaction with $[Ni(dmpe)_2H]^+$ and $[Pt(depe)_2H]^+$, this species is not observed in other cases. The lack of N_2 production from controlled potential electrolysis using $[Ni(depe)_2]^{2+}$ and $HNEt_3^+$ may indicate an upper hydricity bound for proposed N_2O electrocatalysts but more electrolysis experiments using other metal hydrides are necessary to verify this.

3.5 Experimental details

General methods: All syntheses were carried out under an inert atmosphere of dinitrogen in a Vacuum Atmospheres OMNI-Lab glovebox or using standard Schlenk techniques. All electrochemical studies were carried out in an inert atmosphere of argon in a Vacuum Atmospheres OMNI-Lab glovebox. Organic solvents used during synthesis and/or manipulations were degassed by sparging with argon and dried by passing through columns of neutral alumina or molecular sieves and stored over activated 3 Å molecular sieves. Water was obtained from a Barnstead Nanopure filtration system and was degassed under active vacuum. All deuterated solvents were purchased from Cambridge Isotope Laboratories, Inc. Deuterated solvents used for NMR (nuclear magnetic resonance) spectroscopic characterization were degassed via three freeze-pump-thaw (FPT) cycles and stored over activated 3 Å molecular sieves prior to use. All solvents and reagents were purchased from commercial vendors and used without further purification unless otherwise noted. Tetrabuylammonium hexafluorophosphate ($TBAPF_6$) used for electrochemical studies was recrystallized three times from hot ethanol. Electrochemical studies under pure N_2O atmospheres were performed using N_2O (> 99%) from Airgas.

Synthesis

Ir(POCOP^{tBu})H$_2$,[23] [Pt(depe)$_2$H][PF$_6$],[26] [Ni(dmpe)$_2$H][BF$_4$],[29] and [Ni(depe)$_2$][BF$_4$]$_2$[27] were synthesized per literature precedent. [Ni(depe)$_2$H][BF$_4$] was synthesized in a similar manner as [Ni(dmpe)$_2$H][BF$_4$] using CsHCO$_2$.[29] [HNEt$_3$H][BF$_4$] was synthesized per literature precedent using HBF4 etherate.[33]

Physical methods: ^{1}H and ^{31}P{^{1}H} nuclear magnetic resonance (NMR) spectra were collected at 298 K on a Bruker AVANCE 600 MHz spectrometer equipped with a BBFO cryoprobe or a Bruker DRX 500 MHz spectrometer equipped with a BBO probe. ^{2}H NMR spectra were collected on a Bruker AVANCE 600 MHz spectrometer equipped with a TCI probe. Chemical shifts are reported in δ units notation in parts per million (ppm). ^{1}H spectra are referenced to the residual solvent resonances of the deuterated solvent. ^{31}P{^{1}H} spectra were referenced to H$_3$PO$_4$ at 0 ppm within XwinNMR or Bruker's Topspin software, using the known frequency ratios (Ξ) of the ^{31}P standard to the lock signal of the deuterated solvent or referenced to the PF$_6$ anion. Manual shimming, Fourier transformation, and automatic spectrum phasing were performed using Xwin-NMR software when using the 500 MHz spectrometer. Spectra were analyzed and figures were generated using MestReNova 6.0.2 software. Peak integrations were calculated within MestReNova. Infrared (IR) spectra were recorded as compressed solids on an Agilent Cary 630 ATR-FTIR.

Electrochemistry: All measurements were performed on a Pine Wavedriver 10 bipotentiostat. Cyclic voltammetry was performed with a 1 mm diameter glassy carbon disc working electrode, a glassy carbon rod counter electrode, and a Ag$^{+/o}$ pseudo-reference electrode with Fe(C$_5$H$_5$)$_2$ added to the solution. Internal resistance was measured for each solution, and resistance manually compensated for between 80-90% of the measured value for each voltammogram performed. Samples for electrochemical studies performed under N$_2$O atmosphere were prepared by sparging the analyte solution with solvent-saturated N$_2$O gas prior to measurement

and the headspace above the solution was blanketed with N_2O during each measurement. Controlled potential electrolysis experiments were performed in a custom H-cell with the working and counter compartments separated by a fine glass frit. The working and counter compartments were sealed with GL25 and GL18 open top caps with silicone/PTFE septa from Ace Glass. The working compartment contained: 2.0 mM catalyst, 36 mM $HNEt_3BF_4$, 0.2 M $TBAPF_6$ in acetonitrile, a carbon fabric working electrode measuring 2.25"x 0.75", a $Ag^{+/0}$ pseudo-reference electrode separated from the bulk solution with a Vycor tip filled with 0.2 M $TBAPF_6$, and a mercury pool at the bottom of the compartment. The counter compartment contained 0.2 M $TBAPF_6$ in acetonitrile, 0.1 M $Fe(C_5H_5)_2$ as a sacrificial reductant, and a 0.75" x 2.25" piece of carbon fabric as the counter electrode. After the electrolysis period, the volume in the working compartment was measured. The headspace of the working compartment was sampled with a Restek A-2 Luer lock gas-tight syringe. Headspace nitrogen was quantified by gas chromatography using argon as the carrier gas on an Agilent 7890B instrument with a instrument with a HP-PLOT Molesieve column (19095P-MS6, 30m x 0.530 mm, 25 mm) and thermal conductivity detector (TCD).

$Ir(POCOP^{tBu})H_2$ reaction with N_2O

$Ir(POCOP^{tBu})H_2$ (130 mg, 0.141 mmol) was dissolved in benzene (30 mL) and the reddish-brown solution was transferred to a 100 mL Schlenk flask. N_2O was bubbled into the solution for 4 h, turning the solution brown. The solution was allowed to stir with N_2O flowing into the headspace overnight (12 h). The solvent was removed *in vacuo*, leaving a dark brown powder. The solid was dissolved in C_6D_6 for NMR spectroscopy experiments.

N_2O reactivity studies by ^1H NMR

The [M-H]$^+$ sample was dissolved in 0.4 mL of CD_3CN and filtered through a glass microfiber pipette into a J. Young tube. An 0.1 mL aliquot of trimethoxybenzene (25 mM in CD_3CN) was added as an internal standard. The J. Young was freeze-pump-thawed three times using liquid

N_2 to remove gaseous N_2 from the headspace and solution. A starting ^{1}H and ^{31}P{^{1}H} NMR spectrum was acquired. N_2O was then charged into the J. Young using a balloon, starting the timer at 0s. The J. Young sample was exposed to N_2O for 60s and then brought immediately to the spectrometer. [1]H spectra were acquired with 8 scans and a d1 = 1s. Concentrations of [M-H][+] were calculated using the methyl protons of the ligand (24H) and the methoxy protons of the trimethoxybenzene standard (9H, 3.74 ppm). [31]P{[1]H} spectra were acquired periodically to confirm the consumption of [M-H][+].

References

(1)   Severin, K. Synthetic Chemistry with Nitrous Oxide. *Chem. Soc. Rev.* **2015**, *44* (17), 6375–6386. https://doi.org/10.1039/C5CS00339C.

(2)   Severin, K. Homogeneous Catalysis with Nitrous Oxide. *Trends Chem.* **2023**, *0* (0). https://doi.org/10.1016/j.trechm.2022.12.008.

(3)   Tolman, W. B. Binding and Activation of N2O at Transition-Metal Centers: Recent Mechanistic Insights. *Angew. Chem. Int. Ed.* **2010**, *49* (6), 1018–1024. https://doi.org/10.1002/anie.200905364.

(4)   Collman, J. P.; Marrocco, M.; Elliott, C. M.; L'Her, M. Electrocatalysis of Nitrous Oxide Reduction: Comparison of Several Porphyrins and Binary "Face-to-Face" Porphyrins. *J. Electroanal. Chem. Interfacial Electrochem.* **1981**, *124* (1), 113–131. https://doi.org/10.1016/S0022-0728(81)80289-6.

(5)   Taniguchi, I.; Shimpuku, T.; Yamashita, K.; Ohtaki, H. Electrocatalytic Reduction of Nitrous Oxide to Dinitrogen at a Mercury Electrode Using Niii Complexes of Macrocyclic Polyamines. *J. Chem. Soc. Chem. Commun.* **1990**, No. 13, 915–917. https://doi.org/10.1039/C39900000915.

(6) Deeba, R.; Molton, F.; Chardon-Noblat, S.; Costentin, C. Effective Homogeneous Catalysis of Electrochemical Reduction of Nitrous Oxide to Dinitrogen at Rhenium Carbonyl Catalysts. *ACS Catal.* **2021**, *11* (10), 6099–6103. https://doi.org/10.1021/acscatal.1c01197.

(7) Rathnayaka, S. C.; Mankad, N. P. Coordination Chemistry of the CuZ Site in Nitrous Oxide Reductase and Its Synthetic Mimics. *Coord. Chem. Rev.* **2021**, *429*, 213718. https://doi.org/10.1016/j.ccr.2020.213718.

(8) Benson, E. E.; Kubiak, C. P.; Sathrum, A. J.; Smieja, J. M. Electrocatalytic and Homogeneous Approaches to Conversion of CO $_2$ to Liquid Fuels. *Chem Soc Rev* **2009**, *38* (1), 89–99. https://doi.org/10.1039/B804323J.

(9) Kumar, B.; Llorente, M.; Froehlich, J.; Dang, T.; Sathrum, A.; Kubiak, C. P. Photochemical and Photoelectrochemical Reduction of CO2. *Annu. Rev. Phys. Chem.* **2012**, *63* (1), 541–569. https://doi.org/10.1146/annurev-physchem-032511-143759.

(10) Brereton, K. R.; Smith, N. E.; Hazari, N.; Miller, A. J. M. Thermodynamic and Kinetic Hydricity of Transition Metal Hydrides. *Chem. Soc. Rev.* **2020**, *49* (22), 7929–7948. https://doi.org/10.1039/D0CS00405G.

(11) Wiedner, E. S.; Chambers, M. B.; Pitman, C. L.; Bullock, R. M.; Miller, A. J. M.; Appel, A. M. Thermodynamic Hydricity of Transition Metal Hydrides. *Chem. Rev.* **2016**, *116* (15), 8655–8692. https://doi.org/10.1021/acs.chemrev.6b00168.

(12) Miller, A. J. M.; Labinger, J. A.; Bercaw, J. E. Trialkylborane-Assisted CO2 Reduction by Late Transition Metal Hydrides. *Organometallics* **2011**, *30* (16), 4308–4314. https://doi.org/10.1021/om200364w.

(13) Yang, J. Y.; Kerr, T. A.; Wang, X. S.; Barlow, J. M. Reducing CO2 to HCO2− at Mild Potentials: Lessons from Formate Dehydrogenase. *J. Am. Chem. Soc.* **2020**, *142* (46), 19438–19445. https://doi.org/10.1021/jacs.0c07965.

(14) Kaplan, A. W.; Bergman, R. G. Nitrous Oxide Mediated Oxygen Atom Insertion into a Ruthenium–Hydride Bond. Synthesis and Reactivity of the Monomeric Hydroxoruthenium

Complex (DMPE) $_2$ Ru(H)(OH). *Organometallics* **1997**, *16* (6), 1106–1108. https://doi.org/10.1021/om960991i.

(15) Kaplan, A. W.; Bergman, R. G. Nitrous Oxide Mediated Synthesis of Monomeric Hydroxoruthenium Complexes. Reactivity of (DMPE) $_2$ Ru(H)(OH) and the Synthesis of a Silica-Bound Ruthenium Complex. *Organometallics* **1998**, *17* (23), 5072–5085. https://doi.org/10.1021/om980295d.

(16) Figueroa, J. S.; Cummins, C. C. The Niobaziridine–Hydride Functional Group: Synthesis and Divergent Reactivity. *J. Am. Chem. Soc.* **2003**, *125* (14), 4020–4021. https://doi.org/10.1021/ja028446y.

(17) Yamamoto, A.; Kitazume, S.; Pu, L. S.; Ikeda, S. Synthesis and Properties of Hydridodinitrogentris(Triphenylphosphine)Cobalt(I) and the Related Phosphine-Cobalt Complexes. *J. Am. Chem. Soc.* **1971**, *93* (2), 371–380. https://doi.org/10.1021/ja00731a012.

(18) Ortega-Lepe, I.; Sánchez, P.; Santos, L. L.; Lara, P.; Rendón, N.; López-Serrano, J.; Salazar-Pereda, V.; Álvarez, E.; Paneque, M.; Suárez, A. Catalytic Nitrous Oxide Reduction with H2 Mediated by Pincer Ir Complexes. *Inorg. Chem.* **2022**, *61* (46), 18590–18600. https://doi.org/10.1021/acs.inorgchem.2c02963.

(19) Zeng, R.; Feller, M.; Ben-David, Y.; Milstein, D. Hydrogenation and Hydrosilylation of Nitrous Oxide Homogeneously Catalyzed by a Metal Complex. *J. Am. Chem. Soc.* **2017**, *139* (16), 5720–5723. https://doi.org/10.1021/jacs.7b02124.

(20) Jurt, P.; Abels, A. S.; Gamboa-Carballo, J. J.; Fernández, I.; Le Corre, G.; Aebli, M.; Baker, M. G.; Eiler, F.; Müller, F.; Wörle, M.; Verel, R.; Gauthier, S.; Trincado, M.; Gianetti, T. L.; Grützmacher, H. Reduction of Nitrogen Oxides by Hydrogen with Rhodium(I)–Platinum(II) Olefin Complexes as Catalysts. *Angew. Chem. Int. Ed.* **2021**, *60* (48), 25372–25380. https://doi.org/10.1002/anie.202109642.

(21) Kang, P.; Cheng, C.; Chen, Z.; Schauer, C. K.; Meyer, T. J.; Brookhart, M. Selective Electrocatalytic Reduction of CO2 to Formate by Water-Stable Iridium Dihydride Pincer Complexes. *J. Am. Chem. Soc.* **2012**, *134* (12), 5500–5503. https://doi.org/10.1021/ja300543s.

(22) Johnson, S. I.; Nielsen, R. J.; Goddard, W. A. I. Selectivity for HCO2– over H2 in the Electrochemical Catalytic Reduction of CO2 by (POCOP)IrH2. *ACS Catal.* **2016**, *6* (10), 6362–6371. https://doi.org/10.1021/acscatal.6b01755.

(23) Göttker-Schnetmann, I.; White, P. S.; Brookhart, M. Synthesis and Properties of Iridium Bis(Phosphinite) Pincer Complexes (p-XPCP)IrH2, (p-XPCP)Ir(CO), (p-XPCP)Ir(H)(Aryl), and {(p-XPCP)Ir}2{μ-N2} and Their Relevance in Alkane Transfer Dehydrogenation. *Organometallics* **2004**, *23* (8), 1766–1776. https://doi.org/10.1021/om0306700.

(24) Curtis, C. J.; Miedaner, A.; Ellis, W. W.; DuBois, D. L. Measurement of the Hydride Donor Abilities of [HM(Diphosphine)2]+ Complexes (M = Ni, Pt) by Heterolytic Activation of Hydrogen. *J. Am. Chem. Soc.* **2002**, *124* (9), 1918–1925. https://doi.org/10.1021/ja0116829.

(25) Cunningham, D. W.; Barlow, J. M.; Velazquez, R. S.; Yang, J. Y. Reversible and Selective CO2 to HCO2– Electrocatalysis near the Thermodynamic Potential. *Angew. Chem. Int. Ed.* **2020**, *59* (11), 4443–4447. https://doi.org/10.1002/anie.201913198.

(26) Miedaner, A.; DuBois, D. L.; Curtis, C. J.; Haltiwanger, R. C. Generation of Metal Formyl Complexes Using Nickel and Platinum Hydrides as Reducing Agents. *Organometallics* **1993**, *12* (2), 299–303. https://doi.org/10.1021/om00026a014.

(27) Berning, D. E.; Noll, B. C.; DuBois, D. L. Relative Hydride, Proton, and Hydrogen Atom Transfer Abilities of [HM(Diphosphine)2]PF6 Complexes (M = Pt, Ni). *J. Am. Chem. Soc.* **1999**, *121* (49), 11432–11447. https://doi.org/10.1021/ja991888y.

(28) Stratakes, B. M.; Wells, K. A.; Kurtz, D. A.; Castellano, F. N.; Miller, A. J. M. Photochemical H$_2$ Evolution from Bis(Diphosphine)Nickel Hydrides Enables Low-Overpotential

Electrocatalysis. *J. Am. Chem. Soc.* **2021**, *143* (50), 21388–21401.

https://doi.org/10.1021/jacs.1c10628.

(29) Robinson, S. J. C.; Zall, C. M.; Miller, D. L.; Linehan, J. C.; Appel, A. M. Solvent Influence

on the Thermodynamics for Hydride Transfer from Bis(Diphosphine) Complexes of Nickel.

Dalton Trans. **2016**, *45* (24), 10017–10023. https://doi.org/10.1039/C6DT00309E.

(30) Kunerth, W. Solubility of C O 2 and N 2 O in Certain Solvents. *Phys. Rev.* **1922**, *19* (5),

512–524. https://doi.org/10.1103/PhysRev.19.512.

(31) Tomita, Y.; Teruya, S.; Koga, O.; Hori, Y. Electrochemical Reduction of Carbon Dioxide at a

Platinum Electrode in Acetonitrile-Water Mixtures. *J. Electrochem. Soc.* **2000**, *147* (11),

4164. https://doi.org/10.1149/1.1394035.

(32) Ceballos, B. M.; Yang, J. Y. Directing the Reactivity of Metal Hydrides for Selective CO2

Reduction. *Proc. Natl. Acad. Sci.* **2018**, *115* (50), 12686–12691.

https://doi.org/10.1073/pnas.1811396115.

(33) McCarthy, B. D.; Martin, D. J.; Rountree, E. S.; Ullman, A. C.; Dempsey, J. L.

Electrochemical Reduction of Brønsted Acids by Glassy Carbon in Acetonitrile—

Implications for Electrocatalytic Hydrogen Evolution. *Inorg. Chem.* **2014**, *53* (16), 8350–

8361. https://doi.org/10.1021/ic500770k.

(34) Miller, A. J. M.; Labinger, J. A.; Bercaw, J. E. Homogeneous CO Hydrogenation: Ligand

Effects on the Lewis Acid-Assisted Reductive Coupling of Carbon Monoxide.

Organometallics **2010**, *29* (20), 4499–4516. https://doi.org/10.1021/om100638d.